Regenerative and Adaptive Shock Absorber: A Hybrid Design

by

Roberto Ribeiro

A thesis
presented to the University of Waterloo
in fulfillment of the
thesis requirement for the degree of
Master of Applied Science
in
Mechanical and Mechatronics Engineering

Waterloo, Ontario, Canada, 2014

I hereby declare that I am the sole author of this thesis. This is a true copy of the thesis, including any required final revisions, as accepted by my examiners.

I understand that my thesis may be made electronically available to the public.

Abstract

Damping in a multitude of engineering applications has a variable threshold requirement based on the input excitation given to the system. In most applications the desired system response is known but the input to the system is a time dependent function with fluctuating amplitudes and frequencies. Therefore for optimal performance the damping characteristics of a given system must be able to adapt to increase or decrease the amount of energy being absorbed by the system.

In most mechanical systems (including vehicles) damping is achieved through a viscous medium; such as hydraulic oil. Although the oil is capable of absorbing the unwanted energy in the system, its passive nature limits its ability to achieve an optimal amount of damping given the excitation. To achieve the requisite functionality of variable damping; a multitude of solutions have been implemented, proposed, and evaluated at both commercial and academic research levels. These solutions have met the variable damping requirements but have significant drawbacks associated with them.

To address the shortcomings associated with the aforementioned variable damping solutions, a hybrid design consisting of a conventional hydraulic damper and a linear motor topology was fused together to produce a hybrid variable damper. In this hybrid design, the oil in the system acts as bias and the linear motor topology allows for variability in the amount of damping being provided to the system. This hybrid design allows for the requisite variable damping requirement to be achieved. In addition to the hybrid design being able to achieve variable damping, it has the capacity to act as a generator and also provide fail-safe operation due to the viscous bias.

Through analytical, FEM analysis and experimental modeling the hybrid damper has been characterized and with a high level of agreement between the various results. This work has also shown that the design is capable of achieving variable damping with the capacity to recover energy from the system.

Acknowledgements

I would like to first thank my two supervisors; Dr. Mir Behrad Khamesee and Dr. Amir Khajepour, for giving me the opportunity to work on this project. This opportunity did not only increase my level of knowledge with respect to my research topic but I truly believe that my overall engineering aptitude increased significantly as a result. Throughout my research both supervisors were always available to address my concerns and help guide my research in the right direction. In addition to the academic support provided throughout, the financial support during my degree is something that I am extremely thankful for. In additional I would also like to thank Auto21 for providing funding to facilitate this research.I am also truly grateful for the experiences and knowledge I have gained during my studies at the University of Waterloo as a direct result of these supervisors taking a chance on me.

I would also like to thank my office mates and friends at the University of Waterloo for their support throughout my studies. They were always available to help me understand a topic that wasn't of strength to me and offer different perspectives regarding my work. In particular I would like to thank Ehsan Asadi for all of the help, insight and knowledge he shared with me during my research. I truly believe I have developed life lasting relationships with these individuals.

Finally I would like to thank my parents for all of their support. I would not be where I am today without them and the core values they instilled in me during childhood which I continued to embrace through adulthood. My parents could never offer me much help academically due to language barriers and their very limited formal education, but I believe what they did give me is far more valuable.

Dedication

This is dedicated to my parents, Lurdes and Manuel Ribeiro.

Table of Contents

List of Tables

List of Figures

Chapter 1

Introduction

1.1 Damping in Mechanical Systems

Damping in a mechanical system is often the difference between a system's response being stable or unstable. The instability can stem from no damping being present, or an insufficient amount of damping. On the other hand, having an excess of damping is not a desirable attribute either because it would result in a slower overall system response. In a mechanical system damping can be achieved through a damper (or dashpot) and based on the mechanical electrical analogous; resistance in an electrical circuit is equivalent.

System modeling in a multitude of engineering applications typically results in a simplified representation consisting of a series of masses, springs and dampers (refer to Figure 1.1; example of a vehicle suspension system (1/4 car model)). The damper in the referenced figure causes the system to eventually settle to a point of zero motion given a discontinuous input. Damping in a system can be obtained by the structure itself, the addition of a viscous medium, through contact friction or by many other means; all yielding a time dependent decay in response. In all systems there is an optimal damping factor based on the input and the desired response. In most applications, the desired system response is known but the input varies with time. In other instances the desired system response is something that also requires change. In a vehicle for instance; a driver would prefer a very soft suspension system on a rough road (better isolation of the input disturbances) and a very stiff suspension on a very smooth road (sharper handling for high speed maneuvering). In conventional suspension systems, all of the parameters that effect comfort and performance (mass, damping and spring stiffness) are fixed and have suboptimal values for most conditions. Due to the dynamic nature of these systems (both in terms of road conditions

and driver preferences) design engineers are given the difficult task of choosing a damping factor and spring stiffness that will perform adequately at a wide range of inputs; given the passive nature of the mechanisms used in conventional suspension systems.

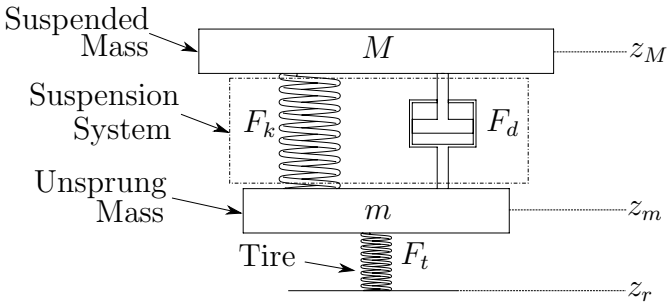

Figure 1.1: Simplified Representation of Vehicle Suspension System.

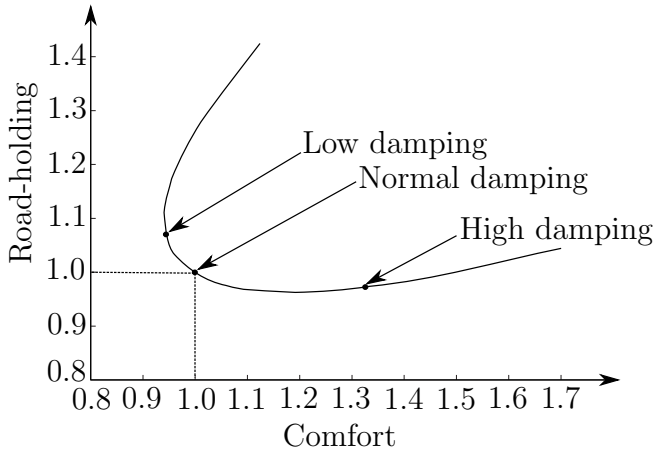

Figure 1.2: Damping Ratio Trade off between comfort and road-holding. Image reproduced from [33].

Figure 1.2 illustrates the trade-off between performance and comfort in a suspension system. This figure clearly shows that with a passive mechanism for damping, the designer can never optimize a suspension system design with respect to these two parameters (Road-holding and Comfort). To achieve an optimal amount of damping given a variable input (assuming the spring stiffness is constant) the damping itself must dynamically fluctuate. In order to achieve this requisite functionality, an active or semi-active suspension system can be implemented.

1.2 Scope of Research and Outline

As previously discussed, there is always a conflict of interest present in the typical suspension systems found in vehicles. This conflict stems from the variability appearing in road profiles (which act as the input to the suspension system) and also the varying requirement to provide optimal driving dynamics or comfort for passengers and drivers. The purpose of this thesis is to evaluate existing variable damping solutions for the automotive industry at both commercial and academic levels of implementation for mid-size passenger vehicles. Based on this evaluation, a new variable damper design will be established and assessed both analytically and experimentally. The scope of this research will be limited to the mechanical design of the damper, and any supporting electronic circuits. Hydraulic modeling(both analytically and though finite element methods), controls theory, controller design and evaluation are outside the scope of this research. This research is being actively worked on as well by a PhD candidate Ehsan Asadi within the same research group. His contribution to this work comes in the form of the optimization, design of the buck booster circuit and the extended finite element model. The determination criteria for this research will be the completion of a functional design and its experimental characterization.

This thesis will be structured in the following manner: Chapter 2 covers a literature review and background. This chapter will review commercial and academic variable damping solutions. In addition common control strategies used for the control of variable dampers will be discussed, and finally a comparison between all of the variable damping solutions will be presented and assessed. Chapter 3 will outline the completed modeling for the proposed variable damping solution. This chapter will include the well known quarter car model that is used for assessing vehicle suspension systems, road profile modeling using the approach outlined in ISO 8608 to model the input disturbance to the quarter car model and the determination of optimal damping will modeled. In addition, this chapter will also show an analytical electromagnetic modeling approach as well as a finite element modeling of electromagnetics. Chapter 4 will outline the design of the proposed damper. This chapter will be broken down in mechanical, electromagnetic, and electronic design and will discuss how all of the parameters of the final prototype were selected. Chapter 5 will cover the experimental validation of the proposed design. This chapter will outline the experimental protocol carried out for testing and fully characterizing the prototype. Finally drawn conclusions and future work will be presented in Chapter 6.

Chapter 2

Literature and Background

Due to the variable nature of input experienced by vehicle suspension systems and the conflicting objectives of comfort and road-holding; it is clear that having the ability to adapt the spring stiffness or damping constant is a beneficial attribute. For the remainder of this thesis the spring stiffness will be considered a constant parameter in the suspension system and the damping coefficient (c) of the damper will become the variable of interest.

The adaptability of damping in a suspension system can be classified into two core categories: **Active** and **Semi-Active**. **Active** damping can be further classified into the following three categories:

1. Load-leveling: This category is typically characterized by the damper actuating at a bandwidth (reaction time of the system) below the main suspension's dynamics [33].
2. Slow-active: This category is typically characterized by the damper working in a bandwidth between the body and wheel dynamics [33].
3. Fully-active: This category is typically characterized by the damper actuating at the full bandwidth of the suspension system [33].

In the same manner **Semi-Active** suspension systems can be further classified into two additional sub-categories:

1. Adaptive suspension: This category is typically characterized by the damper slowly changing its damping ratio in an open-loop configuration [33].

2. Semi-active: This category is typically characterized by the damper changing its damping ratio in a closed-loop configuration [33].

Both the **Active** and **Semi-active** modes of operation have positive and negative attributes associated with them dictated by application. For instance one of the fundamental shortcomings of a fully-active suspension system implementation is the significant amount of power consumption; but arguably the best performance can be achieved in this mode. Alternatively the semi-active implementation can be configured to have no (or marginal) power consumption but its inability to provide an active force input can inherently reduce its performance. Ultimately the mode of operation will be determined predominately by the application oppose to the damping hardware itself, due to the various topologies (commercial and non-commercial) being able to operate in both modes. The following sections of this chapter will present the various topologies commercially available among others that are being developed in academic institutions globally.

2.1 Commercial Products

The first commercial implementation of an adaptable suspension system in the automotive industry was developed by Citroën in the 1960s with its hydro-pneumatic suspension [33]. In the 1980s this technology was capable of further progression due to advancements in analogue electronics as well as micro controllers. During this era Lotus became the leader in this segment with their hydraulic adaptable suspension which they implemented in Formula 1 racing as well as in production vehicles [33]. In the 1990s the development of this system became less relevant to Lotus after the Fédération Internationale de l'Automobile (FIA) banned the use of electronic suspensions in Formula 1 competitions. Later on in the 1990s, adaptable dampers became relevant once again and led to the development of three core products that are commercially available today and in use in a multitude of applications.

Delphi, Fludicon and Sachs are the three main players currently in the adaptable suspension system market. Each of these companies has developed a complete solution (hardware, controllers and software) to attain variable damping based on their own proprietary technology (refer to Figure 2.1).

The system developed by Delphi (Figure 2.1a) is called the magnetorheological damper (MR) based on the magnetorheological fluid it uses to operate. Within this damper there is an electromagnet that produces a magnetic field when energized. When a magnetic field is present, the magnetorheological fluid changes its viscosity. The viscosity in this

(a) Delphi Magnetorheological Damper (MR).

(b) Fludicon Electrorheological Damper(ER).

(c) Sachs Solenoid Valve Damper(SVD).

Figure 2.1: Commercial variable damping solutions. Image reproduced from [33].

medium changes with a magnetic field because of the presence of ferrous particulate in the fluid. When a field is not present the particulate is randomly dispersed, and once a field is applied the particulate aligns in a uniform manner causing the viscosity of the medium to change. The system developed by Fludicon (Figure 2.1b) is called the electrorheological damper (ER) based on the electrorheological fluid it uses to operate. Similar to the Delphi MR damper, the Fludicon ER damper is capable of changing the viscosity of its working medium dynamically. The major difference between the ER and MR damper is that the ER damper excites the particulate in the fluid with an electric field and the MR damper uses a magnetic field as previously outlined. Finally, the system developed by Sachs (Figure 2.1c) is called the Solenoid Valve Damper (SVD). This damper, unlike the others does not use a special fluid as its working medium. It achieves variable damping by adding or removing flow restrictions within the system to change the amount of force it produces. This system uses a series of solenoid valves to achieve this functionality.

Although still in the research/pre-production stages of commercialization Bose has also been developing an active suspension system since approximately 1980 [19]. Within this system each wheel has its own linear electromagnetic motor which takes the place of a conventional damper and a torsion bar spring which supports the static weight of the vehicle [10]. Although this system is active, it also has regenerative capabilities by using the linear electromagnetic motors as generators when not being actively driven. The projected power consumption of this system is approximately one third of what an automotive air-conditioner consumes [19]. Another company still in the research/pre-production stages of commercialization is Levãnt power. Levãnt power has developed a system that is capable of changing damping characteristics in a manner similar to how the Sachs damper operates

(through a flow restriction). The novel aspect of this design is that the system is capable of generating power through the use of a hydraulic motor and that the design is retrofitable for existing OEM dampers [30] (refer to Figure 2.2). Another variable damping solution in the commercial space at a research and development level is the Dynamic Suspension Energy Recovery Damper(DSRED) developed by Multimatic. The DSRED system harvests power from the vehicle's suspension system using an innovative mechanism that spins a generator to produce power. The produced power is then stored in a capacitor for later discharge back into the system, by the proprietary electronic management system developed by Multimatic [26].

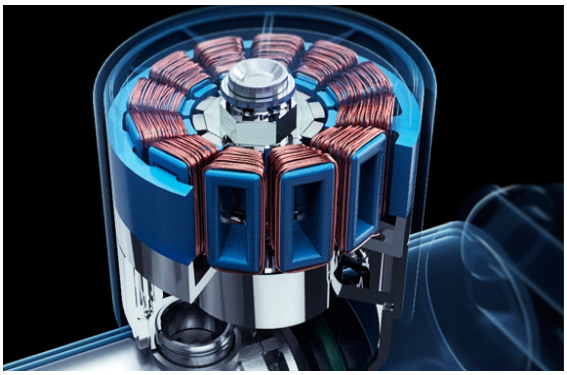

(a) Levãnt power hydraulic motor.

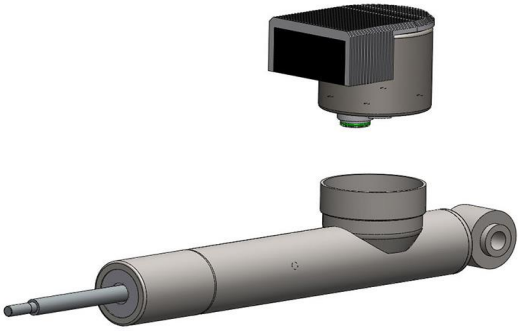

(b) Levãnt power OEM system integration capability.

Figure 2.2: Levãnt power Variable Damping Solution. Images reproduced from [30].

Once again at a slightly different level of commercialization (commercialized but significant amount of proprietary intellectual property); Audi AG, Mercedes-Benz, and BMW have all developed systems to improve driving dynamics and passenger comfort. Audi AG has developed/implemented three variable damping solutions in their vehicles: *Magnetic Ride*, *Adaptive Air Suspension*, and *Dynamic Ride Control*. The *Magnetic Ride* system in its simplest form is a set of four MR dampers (similar technology to the Delphi damper) and a network of sensors. The sensor network monitors road conditions and driving style, and adjusts each damper accordingly to ensure a balanced ride is achieved [3]. This system can also be put into sport mode, which attempts to optimize the damping in the vehicle to achieve optimal road holding conditions. The *Adaptive Air Suspension* uses struts and air springs enclosed in the shock absorbers at the front of the vehicle; and in the rear the shock absorbers and air springs are separated [2]. The air springs change the ride

height as a function of speed and driver preference to increase fuel economy, comfort and ground clearance. The dampers are able to provide variable damping characteristics based on an integrated electromagnetic valve which internally changes flow characteristics. Finally, the *Dynamic Ride Control* system emphasis is vehicle dynamics; it achieves this by augmenting the body roll and pitch characteristics around the transverse and longitudinal axes [4]. This system operates by having a set of diagonally opposing shock absorbers that are linked via a hydraulic connection. During an event such as high speed cornering, a valve regulates oil flow in the shock absorber of the deflected outside wheel which reduces the lateral tilt of the vehicle [4].

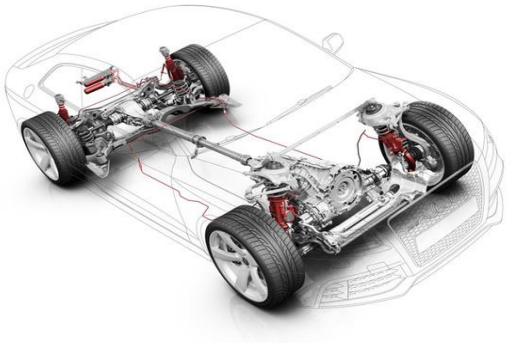

(a) Audi AG Dynamic Ride Control. Image reproduced from [4]

(b) BMW Dynamic Drive. Image reproduced from [7]

Figure 2.3: Automotive Manufactures' Viable Damping Solutions.

The active chassis system developed by BMW is called *Dynamic Drive* [7]. The objective of this system is to provide better road holding characteristics, stability and comfort. The system uses two active stabilizer bars on the front and rear axles and a sensor network. During an event such as driving in a straight line, the *Dynamic Drive* system will reduce the pressure on the active stabilizers to increase passenger comfort. During a cornering event, the system can independently change the rigidity of the stabilizers to optimize the roll distribution of the vehicle, achieving better road holding and stability characteristics [7]. Finally, the system developed by Mercedes-Benz is called *Active Body Control(ABC)* and its main objective is comfort. The system implements four active hydraulic dampers and a sensor network that is capable of eliminating pitch, roll and vertical movement of the chassis [25]. As part of this system, a high pressure hydraulic pump is used to quickly

change the length of each damper independently based on the road and driving conditions.

Judging from the systems outlined above, it is clear that variable damping is a topic of interest within the commercial space. As with any technology there are advantages and disadvantages associated with the products or systems developed. The major disadvantage of most of the systems presented above is their power consumption. Based on this fundamental short-coming, a significant amount work has been done at a variety of academic institutions in an attempt to address this issue. The following section will further detail the non-commercial development efforts.

2.2 Non-Commercial Variable Damping Solutions

As previously mentioned, the core deficiency with most of the commercially available variable damping systems is their power consumption. Although these systems are capable of providing better comfort or driving dynamics in vehicles; their consumption negates the performance benefits in most automotive market segments. In the last decade the fuel efficiency of vehicles has been a topic of interest and much work has gone into improving this efficiency. Work done by Bandivadekar et al. [5] has shown that only 10-16% of the fuel burned in an average car goes toward actually driving the car and the remaining energy is consumed by losses in the system (air drag, friction, thermal losses, etc.). Based on the work done by Bell [6]; the greatest opportunity for energy recovery from a vehicle comes from the waste heat produced by the engine, braking systems, and finally, the suspension system. In addition Zuo et al. [42] found that an average power of 100, 400 and 1600 W is available for harvesting at 60 mph on ISO road classes B (good), C (average) and D (poor)respectively.

Based on the potential for significant energy recovery from a vehicle's suspension system; many of the variable damping solutions being developed in academic institutions have the capacity to produce variable damping and also recover energy. The dampers being developed in the academic world can be classified into two main categories: rotatory and linear. The subsequent sub-sections of this chapter will further define each category.

2.2.1 Rotary Topology

The rotary topology consists of an electric motor (DC or AC permanent magnet motor) and some mechanism for converting the linear translation from the suspension system to rotary motion. Many systems have been developed based on the rotary topology with the

major variation resulting from the design and choice of mechanism for motion conversion. Gupta et al. [15] developed a damper which uses a system of gears, an input lever and DC motor. This design allowed for motion magnification due to the chosen gearing (motion magnification of interest to maximize the output). Kawamoto et al. [21], Nakano et al. [27], Cassidy et al. [8] and Zhang et al. [39], [40] all developed systems which used motors and ball screws to convert the linear motion of the damper to rotary motion for the motor. Another interesting design was one proposed by Fujimoto et al. [13]. In this work they detailed the design of their spiral motor which uses a ball screw as the main shaft of the motor with permanent magnets attached to it; and the main body (the stator) has slots and coils. Notwithstanding the novel/innovative nature of this design; it is severely hindered by its complexity. Refer to Figure 2.4 for a schematic representation of the design proposed by Fujimoto et al. [13]. In general, the ball screw design is very robust and reliable but typically is better suited for low frequency applications due to the nature of the mechanism.

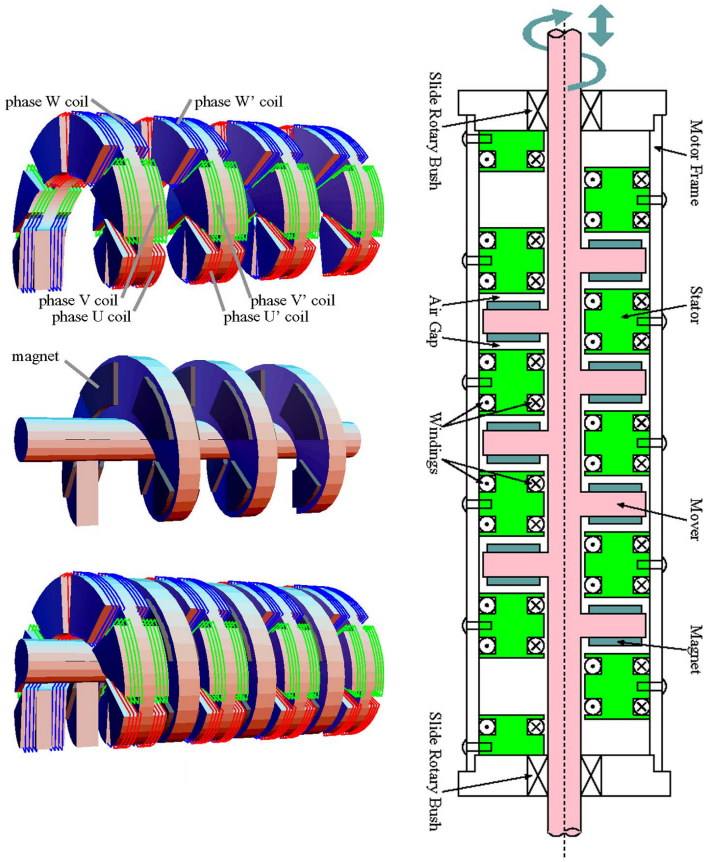

Figure 2.4: Spiral Motor Design Developed by Fujimoto et al.. Image reproduced from [13].

Rome et al. [32] and Li et al. [23], [22] both developed systems that use motors and a rack and pinion mechanism for the motion conversion. The design developed by Li et al. [23], [22] also included a motion magnification by using a set of planetary gears. In general, the rack and pinion mechanism used in both of these designs is more suitable for higher frequency applications because the mechanism itself is capable of handling quick changes in direction a bi-directional manner. Refer to Figure 2.5 for a schematic representation of one of the ball screw designs and one of the rack and pinon designs.

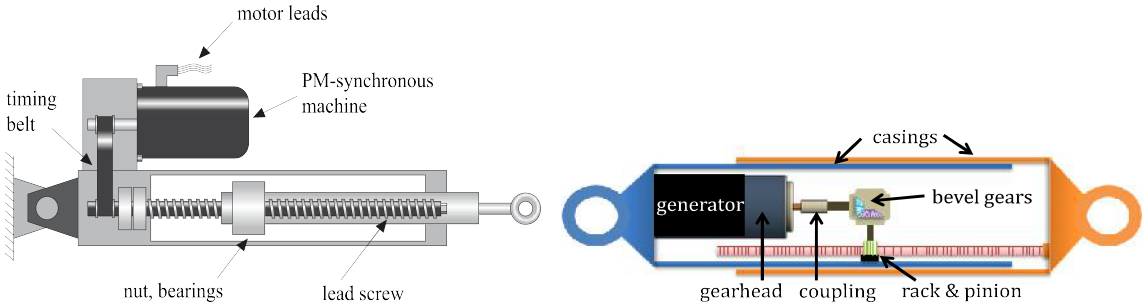

(a) Rotary Topology Ballscrew Design. Image reproduced from [8].

(b) Rotary Topology Rack and Pinon Design. Image reproduced from [22].

Figure 2.5: Rotatory Topology Designs.

2.2.2 Linear Topology

The linear damper topology consists of a series of coils and magnets configured in manner where either the coils or magnets move concentric to one another. This relative motion between the coils and magnets induces a voltage in the coils as per the Faraday-Lenz law. Zuo et al. [41] based on their analysis and design found that maximizing the output power of a system configured in the linear topology can be achieved by either increasing the magnetic flux intensity or by amplifying the magnitude of the input motion. Gysen et al. [16] developed a similar design to the one developed by Zuo et al. [41] with the major difference being the inclusion of an inline spring element and the use of a slotted stator. The Gysen et al. [16] design was also intended to be used in a fully active configuration, opposed to semi-active (which also differentiates it from [41]). Another design based on the linear topology was developed by Ebrahimi et al. [12] with the basis of the damping mechanism being eddy current. Although eddy current damping has been demonstrated in this work; if regeneration is of interest the eddy current effect eliminates the potential

for energy. Refer to Figure 2.6 for a schematic representation of the systems developed by Gysen et al. [16] and Zuo et al. [41].

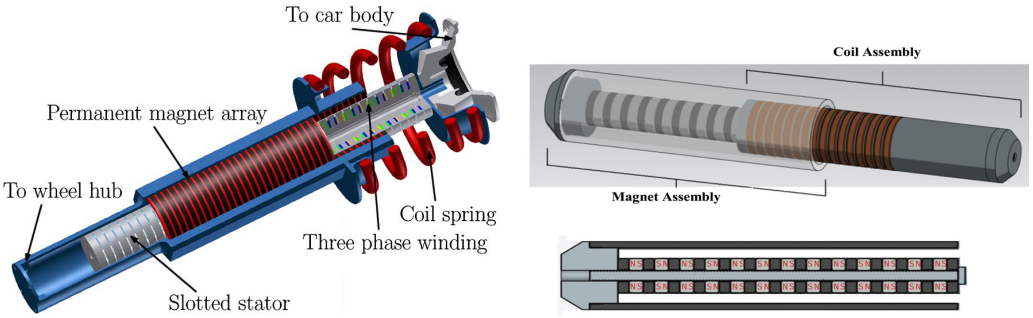

(a) Linear Topology Design Developed by Gysen et al.. Image reproduced from [16].

(b) Linear Topology Design Developed by Zuo et al.. Image reproduced from [41].

Figure 2.6: Linear Topology Designs.

The most attractive aspect of the linear topology for automotive applications is that no change in motion direction is required (linear motion of the suspension system directly capable of producing an output). Hence this topology is a bit simpler to implement mechanically in comparison to the rotary configuration.

2.3 Tuning Mechanism and Energy Recovery

2.3.1 Damping Tuning Mechanism

For both the linear and rotary topologies discussed, variable damping is typically achieved by shunting the output of the system with a load. Figure 2.7 illustrates a schematic of an electrical circuit which could be used for a linear topology variable damper. As previously discussed, when the permanent magnet (PM in Figure 2.7) moves inside a coil it induces a voltage in that coil. If the output from the coil is not connected to anything no damping force would be produced (open loop configuration). If the two ends of the coil were tied together maximum damping force would be achieved (short circuited configuration). Finally, if a variable load is applied between the two ends of the coil a variable amount of damping force could be achieved (variable configuration). The shunting of the output produces variable force due to the load (R in this case) drawing a variable amount of current; which in turn produces an electromagnetic field. This newly produced field will

now oppose the field produced by the permanent magnet, resulting in a force. Following the shunting load (in Figure 2.7) is a diode bridge(or full bridge rectifier) which is used to rectify the AC output of the coil into DC, a filtering capacitor (C) after the full bridge rectifier to filter the output of the rectifier, and finally the load for the system (B). A very similar electrical circuit could be used for the rotary topology as well.

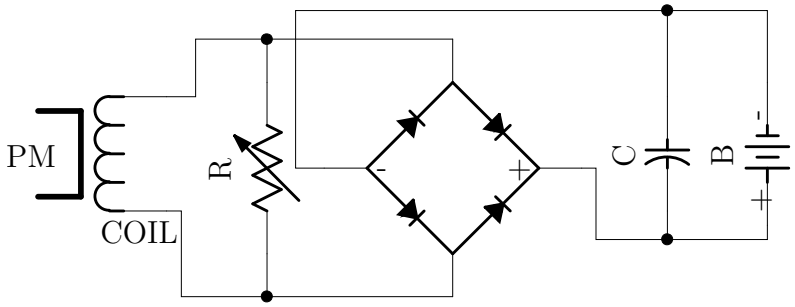

Figure 2.7: Linear Topology Variable Damping Control Circuit Schematic.

2.3.2 Energy Recovery

When the non-commercial topologies are not being subjected to the previously described short circuited condition (maximum force-generation condition), the capacity for energy recovery is present. To maximize the energy harvesting capacity for both of these topologies, three approaches can used. If no complex impedance is present in the system (produced by inductance or capacitance) or is negligible; the maximum power transfer theorem can be used to maximize the output. This theorem states that maximum power transfer between a source and load will occur when the electrical resistance of the source is equal to that of the load ($R_{source} = R_{load}$). When complex impedance is present additional power loss will occur due to the phase lead or lag between current and voltage. If complex impedance is present in the system, impedance matching in the electrical domain should be used to maximize the output. An alternative approach of impedance matching for a complex condition is impedance matching across the mechanical and electrical domains [14]. In this approach the electrical impedance is the summation of the impedance of the source and the load circuit and the mechanical impedance is based on the mechanical system solely. It is important to note that this approach is only possible when a mechanical system has a free response.

2.4 Control Strategies

As discussed in subsection 2.3.1, the damping tuning mechanism in its simplest form for the non-commercial damping solutions is shunting the output of the damper with a load. The shunting will allow for variation in the amount of force being produced by the damper to counter any unwanted disturbances. In a similar manner, damping in the previously described commercial products is attenuated by varying the magnetic field, electric field or valve opening in each of the previously described technologies (MR, ER, and SV dampers). By knowing the amount of force ($F_d = c\dot{z}$) the damper is capable of producing and measuring key attributes of the suspension system (typically the velocities of the suspended mass and unsprung mass) an optimal amount of damping force can be produced to meet the objective of the system (road-holding, comfort or a combination of both). In order to achieve this functionality a control algorithm or strategy must be implemented. A variety of the control algorithms have been developed over the years and an extensive amount of literature is available for semi-active and fully-active systems. In both semi-active and fully-active configurations, the most commonly used control strategies are Skyhook and Groundhook.

2.4.1 Skyhook

The Skyhook control strategy was first developed by D. Karnopp et al. [20]. This control strategy is typically associated with comfort rather than road-holding. In order to achieve the comfort objective, the algorithm attempts to minimize the amount of displacement experienced by the sprung mass in a typical quart car model(refer to Figure 1.1). The physical model for this control strategy consists of a damping element connected between a sky reference frame (above suspended mass) and the suspended mass, a spring element between the suspended mass and the unsprung mass and a secondary spring element between the unsprung mass and the road reference frame(z_r).The equation below ((2.1)) reflects how the damping coefficient would vary in an on/off or two state (other strategies such as linear, Acceleration Driven Damper (ADD), Power Driven Damper (PDD) could also be used [33]) configuration as a function of the velocity of the suspended and unsprung masses respectively:

$$c = \begin{cases} -c_{max} & \text{if } \dot{z}_M(\dot{z}_M - \dot{z}_m) \geq 0 \\ +c_{max} & \text{if } \dot{z}_M(\dot{z}_M - \dot{z}_m) < 0 \end{cases} \tag{2.1}$$

In equation (2.1) c represents the damping coefficient returned by the algorithm, $\pm c_{max}$ represents the maximum damping coefficient the damper is capable of producing in the positive and negative direction, and $\dot{z}_M$ & $\dot{z}_m$ represent the velocities of the suspended and unsprung mass respectively. The logic shown in equation (2.1) is only valid for a fully-active system due to a semi-active dampers' inability to produce an active force. If equation (2.1) was re-written for a semi-active configuration, the $+c_{max}$ would be zero or the steady state value of the damper.

2.4.2 Groundhook

The objective of the Groundhook control strategy is road-holding, as oppose to comfort seen in the Skyhook model. The Groundhook control strategy was first developed by Valek et al. [35] and the basis of the model is to reduce tire forces and deflection of the unsprung mass. The physical model used for this control strategy consists of a spring element between the suspended and unsprung masses, a secondary spring element between the unsprung mass and the road reference frame(z_r), and a damping element between upsprung mass and a ground reference frame below the road reference. Equation (2.2) reflects the logic used in the Groundhook control strategy based on a two state configuration.

$$c = \begin{cases} +c_{max} & \text{if } \dot{z}_m(\dot{z}_M - \dot{z}_m) \geq 0 \\ -c_{max} & \text{if } \dot{z}_m(\dot{z}_M - \dot{z}_m) < 0 \end{cases} \tag{2.2}$$

All of the variables shown in (2.2) are the same as what was previously defined in the Skyhook model((2.1)). The major difference between equations (2.1) & (2.2) is that signs change on the c_{max} terms. As previously mentioned if this model was implemented in a semi-active configuration, the $-c_{max}$ term would be zero or its steady state value.

2.5 Technology Comparison

To further quantify each of the variable damping solutions previously presented, it is beneficial to tabulate the major advantages and disadvantages associated with each system. Since only the systems developed by Delphi, Fludicon and Sachs in the commercial space have reached a mature stage in their product life cycle and are also currently available for third party integration into vehicles; they will be the focus of the comparison. For comparison of the non-commercial topologies, the two categories(rotary and linear) will be all-encompassing of the various designs previously discussed. Tables 2.1 and 2.2 reflect the advantages and disadvantages that were identified through literature review and knowledge of each product in its applicable market segment (automotive; mid-size passenger vehicles).

Advantages			
SV Damper	MR Damper & ER Damper	Linear Design	Rotary Design
Simple control mechanism	Control of system	High level of control due to number of coils	Use of off-the-shelf components
Standard oil for operation	Suitable form factors for retrofitting of existing equipment	Based on existing topology (Linear actuator)	Amount of force system is able to produce
Robust mechanism	Capacity to increase comfort and driving dynamics	Regenerative	Clean three phase output (low noise)
Fail safe in event of electronics failure	Fail safe in event of electronics failure	No power consumption	Regenerative
		No change in motion direction	
		Fast Response	No power consumption

Table 2.1: Advantages of Presented Damper Topologies

Disadvantages			
SV Damper	MR Damper & ER Damper	Linear Design	Rotary Design
Power consumption	Power consumption	Not fail-safe	Backlash in design
Slow response time	Degradation of fluid	Additional complexity due to regeneration (power electronics)	Weight of System
Temperature sensitivity	Weight of System	Use of rare earth permanent magnets	Axial loading on generator motors and motor life
Sealing	Cost of Fluid	Amount of force proportional size	Higher mechanical loses
Bulky		Significant number of custom components	Size of system
			Not fail-safe

Table 2.2: Disadvantages of Presented Damper Topologies

Starting with the Solenoid Valve Damper (SVD); its core competency relates to the simplicity of operation. Solenoid valve technology is used in many industries (solenoid valves are found in many industrial machines) and can be considered a mature technology. The major disadvantages associated with this technology relate to its relatively slow response time and power consumption. Since the Delphi Magnetorheological Damper (MR) and Fludicon Electrorheological Damper (ER) are fundamentally the same device, they have identical advantages and disadvantages. The major advantages of these systems is their fail-safe nature, and proven performance in automotive applications. The core disadvantages associated with these systems is their power consumption, cost of the working medium (MR and ER fluid respectively) and the degradation of the working medium. Now by considering the linear topology; the major advantages associated with topology is its fast response time, capacity to act in a regenerative mode; and no change in the input motion direction is required. The major disadvantages related to this technology is that it is not fail-safe, the amount of force it can produce is proportional to size (larger size more force), and the topology requires rare earth magnets for operation. Finally, the major advantages associated with the rotary topology is the amount of force the system is able to produce, its

capacity to work in a regenerative mode, and the use of standard off-the-shelf components. The major disadvantages associated with this topology would be the mechanical losses due to the change in motion direction, and that it is not fail-safe.

Overall, the commercial products are attractive due to their proven performance and fail-safe operation. The major disadvantage results from the amount of power they consume. The linear and rotary topologies are attractive due to high performance characteristics and regenerative capacity. The major disadvantage is that these systems are not fail-safe. In order to address the key concern associated with the commercial products, the power consumption must be reduced or eliminated. To address the key concern with the non-commercial damping solutions, the designs need to be fail-safe. Therefore to address these various concerns it is proposed that the linear topology is chosen as the basis of a new design with the integration of a viscous medium for additional damping. This proposed design will address the power consumption issue due to this designs capabilities to be run in a semi-active with configuration with trivial power consumption and also act as a generator. Making the damper fail safe is addressed by the integration of a viscous medium. In addition the proposed design also benefits from the high performance characteristics of the linear topology and the others stated in Table 2.1.

The following section of this thesis will detail the modeling approach taken for this newly-proposed hybrid damper.

Chapter 3

Modeling

In this chapter the modeling techniques employed to analyze the proposed hybrid damper will be developed and discussed. For a suspension system it is important to understand and model the motion of the suspended and usprung masses in a vehicle in order to evaluate the performance of individual components or the overall system response. Given that the proposed design achieves its variability in damping based on electromagnetic theory, the modeling approach and analysis of this subsystem is of interest. The following sections will outline the process, considerations and results obtained based on the completed modeling.

3.1 Quarter Car Model

As previously mentiond, a typical manner of modeling a vehicle's suspension system response is by means of the quarter car model. This model consists of a suspended mass representing one quarter of the chassis mass, a damping element which represents a shock absorber in a vehicle suspension system,a spring element which represents a spring typically found in a vehicle suspension system (spring element can be parallel or in series with the damper), an unsprung mass which represents the mass of the vehicle's wheel, and another spring element representing the stiffness of the vehicle's tire. Figure 3.1 illustrates a schematic representation of the quarter car model and the adopted nomenclature.

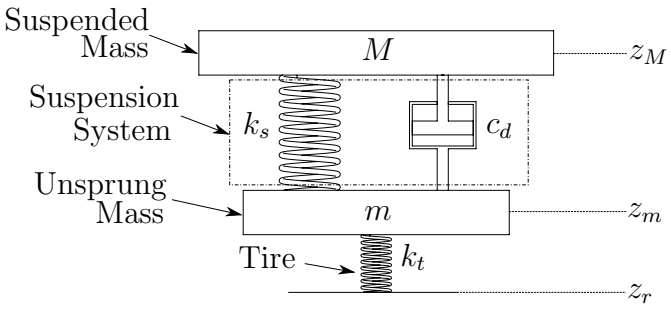

Figure 3.1: Schematic of Quarter Car Model for development of equations of motion.

In Figure 1.1, k_s represents the stiffness of the spring in the suspension system, c_d represents the damping coefficient of the damper, z_M, z_m, z_r represent the vertical positions of the suspended mass, unsprung mass, and road surface, respectively. The development of the quarter car model is based on the following list of assumptions [29]:

1. The tire and road always maintain contact
2. Friction between the tire and road is negligible
3. The vehicle tire does not have any damping characteristics
4. No rotational motion of the wheel and chassis (m, M respectively)
5. All spring and damping elements in the system have linear behaviors

Now with the nomenclature and assumptions defined, the free body diagrams for the suspended and unsprung masses can be created (refer to Figure 3.2). Based on Figure 3.2 the following equations of motion can be written for the unsprung and suspended masses respectively:

$$m\ddot{z}_m - c_d(\dot{z}_M - \dot{z}_m) + k_t(z_m - z_r) - k_s(z_M - z_m) = 0 \tag{3.1}$$

$$M\ddot{z}_M + c_d(\dot{z}_M - \dot{z}_m) + k_s(z_M - z_m) = 0 \tag{3.2}$$

To further simplify the nomenclature found in equations (3.1) and (3.2) going forward $z_m = x_1, z_M = x_2$, & $z_r = x_3$. By rewriting equations (3.1) and (3.2) with the updated nomenclature, the following equations can be written:

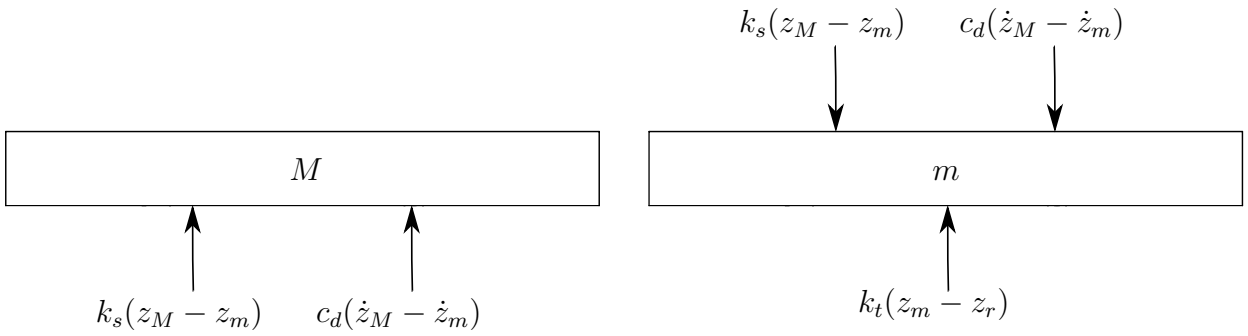

(a) Free body diagram of suspended mass.

(b) Free body diagram of unsprung mass.

Figure 3.2: Free body diagrams for quarter car model.

$$m\ddot{x}_1 - c_d(\dot{x}_2 - \dot{x}_1) + k_t(x_1 - x_3) - k_s(x_2 - x_1) = 0 \tag{3.3}$$

$$M\ddot{x}_2 + c_d(\dot{x}_2 - \dot{x}_1) + k_s(x_2 - x_1) = 0 \tag{3.4}$$

By applying a Laplace transformation assuming zero initial conditions to equations (3.3) and (3.4) using $X_1, X_2, \& X_3$ as the Laplace transformation variables, the following can be written:

$$ms^2X_1(s) - c_dsX_2(s) + c_dsX_1(s) + k_tX_1(s) - k_tX_3(s) - k_sX_2(s) + k_sX_1(s) = 0 \tag{3.5}$$

$$Ms^2X_2(s) + cdsX_2(s) - cdsX_1(s) + k_sX_2(s) - k_sX_1(s) = 0 \tag{3.6}$$

By simplifying and rearranging equations (3.5) and (3.6) the following matrix representation of the system of equations can be written:

$$\begin{bmatrix} ms^2 + c_ds + k_t + k_s & -c_ds - k_s \\ -c_ds - k_s & Ms^2 + c_ds + k_s \end{bmatrix} \begin{bmatrix} X_1(s) \\ X_2(s) \end{bmatrix} + \begin{bmatrix} -k_t \\ 0 \end{bmatrix} X_3(s) = \begin{bmatrix} 0 \\ 0 \end{bmatrix} \tag{3.7}$$

Now by solving the system of equations shown above, the following expressions can be

written:

$$X_1(s) = \frac{k_t X_3(s)(Ms^2 + c_d s + k_s)}{ms^4M + ms^3c_d + ms^2k_s + c_d s^3M + k_t Ms^2 + k_t c_d s + k_t k_s + k_s Ms^2} \tag{3.8}$$

$$X_2(s) = \frac{X_3(s)k_t(c_d s + k_s)}{ms^4M + ms^3c_d + ms^2k_s + c_d s^3M + k_t Ms^2 + k_t c_d s + k_t k_s + k_s Ms^2} \tag{3.9}$$

In addition to equations (3.8) and (3.9) it is useful to define transfer functions to evaluate the effectiveness of the suspension system. In general the transmissibilty, acceleration, rattle space(suspension travel), and tire deflection transfer functions are useful [31].

Starting with the transmissibility transfer function; this function relates the displacement of the suspended mass to the excitation of the road input($X_2(s)/X_3(s)$). The transmissibility ratio can be used as a means of evaluating a system's vibration isolation capacity. To maximize the isolation characteristics of a system (minimize ratio to meet comfort objective) its natural frequency should be kept from the frequency band the displacement disturbance operates within. Based on equation (3.8), this ratio is equal to:

$$H_T(s) = \frac{k_t(c_d s + k_s)}{ms^4M + ms^3c_d + ms^2k_s + c_d s^3M + k_t Ms^2 + k_t c_d s + k_t k_s + k_s Ms^2} \tag{3.10}$$

Based on the transmissibility transfer function (3.10), the acceleration transfer function can be defined ($s^2H_T(s)$). In order to achieve optimal ride comfort the acceleration of the sprung mass should be minimized. This transfer function relates the acceleration of the suspended mass to the road excitation in the following manner:

$$H_A(s) = \frac{s^2(k_t(c_d s + k_s))}{ms^4M + ms^3c_d + ms^2k_s + c_d s^3M + k_t Ms^2 + k_t c_d s + k_t k_s + k_s Ms^2} \tag{3.11}$$

The rattle space transfer function is the ratio of the relative displacements between the suspended and unsprung masses relative to the road reference frame($X_2(s) - X_1(s)/X_3(s)$) . Similar to the tramissibility and acceleration transfer functions; in order to achieve the

best ride comfort the rattle space or suspension travel should be minimized [17]. The following represents the rattle space transfer function:

$$H_{RS}(s) = \frac{k_t M s^2}{ms^4 M + ms^3 c_d + ms^2 k_s + c_d s^3 M + k_t M s^2 + k_t c_d s + k_t k_s + k_s M s^2} \tag{3.12}$$

The last transfer function of interest is the tire deflection ratio. Unlike the previously defined transfer functions, the tire deflection transfer function is of interest for evaluating the road-holding performance of a suspension system [31]. This ratio relates the tire deflection to the road reference frame$(X_1(s) - X_3(s)/X_3(s))$. The following represents the tire deflection transfer function:

$$H_{TD}(s) = \frac{s^2(ms^2 M + msc_d + mk_s + c_d s M + k_s M)}{ms^4 M + ms^3 c_d + ms^2 k_s + c_d s^3 M + k_t M s^2 + k_t c_d s + k_t k_s + k_s M s^2} \tag{3.13}$$

By knowing the physical characteristics of a given quarter car model $(M, k_s, c_d, m, \,\&\, k_t)$, equations (3.10), (3.11), (3.12), and (3.13) can be used to evaluate a system in the frequency domain.

As an alternative to the frequency domain solution shown above, equations (3.3) and (3.4) can be solved using the state space representation (known as time-domain approach). The general form of the state space solution is as follows:

$$\dot{x} = Ax + Bu \tag{3.14}$$

$$y = Cx + Du \tag{3.15}$$

In equation (3.14); A is the state matrix, x is the state vector, B is the input matrix, and u is the input vector. In equation (3.15); C is the output matrix, and D is the feed-through matrix(x, & u in equations (3.14) and (3.15) are equivalent). In order to solve equations (3.3) and (3.4) with the state space approach, the state vector (x) must be substituted into these equations. The state vector can be assumed to have the following form:

$$z_m = x_1 \tag{3.16a}$$

$$\dot{z}_m = x_2 \tag{3.16b}$$

$$z_M = x_3 \tag{3.16c}$$

$$\dot{z}_M = x_4 \tag{3.16d}$$

From the state vector shown above (3.16), the following two additional relationships can be derived:

$$\dot{x}_1 = x_2 \tag{3.17}$$

$$\dot{x}_3 = x_4 \tag{3.18}$$

Now if the relationships shown in the state vector (3.16) are substituted into equations (3.3) and (3.4), the following can be written:

$$\dot{x}_2 = -\frac{k_t + k_s}{m}x_1 - \frac{c_d}{m}x_2 + \frac{k_s}{m}x_3 + \frac{c_d}{m}x_4 + \frac{k_t}{m}z_r \tag{3.19}$$

$$\dot{x}_4 = \frac{k_s}{M}x_1 + \frac{c_d}{M}x_2 - \frac{k_s}{M}x_3 - \frac{c_d}{M}x_4 \tag{3.20}$$

Now by substituting equations (3.17), (3.18), (3.19), and (3.20) into equation(3.14), the following can be written:

$$\begin{bmatrix} \dot{x}_1 \\ \dot{x}_2 \\ \dot{x}_3 \\ \dot{x}_4 \end{bmatrix} = \begin{bmatrix} 0 & 1 & 0 & 0 \\ -\frac{k_t+k_s}{m} & -\frac{c_d}{m} & \frac{k_s}{m} & \frac{c_d}{m} \\ 0 & 0 & 0 & 1 \\ \frac{k_s}{M} & \frac{c_d}{M} & -\frac{k_s}{M} & -\frac{c_d}{M} \end{bmatrix} \begin{bmatrix} x_1 \\ x_2 \\ x_3 \\ x_4 \end{bmatrix} + \begin{bmatrix} 0 \\ \frac{k_t}{m} \\ 0 \\ 0 \end{bmatrix} z_r \tag{3.21}$$

In order to obtain the displacement and velocity of the suspended and unsprung masses, the output matrix (C) in equation (3.15) needs to be set to the identity matrix(I_4); and if the feed-forward matrix is assumed to be zero the following can be written:

$$y(t) = \begin{bmatrix} z_m(t) \\ \dot{z}_m(t) \\ z_M(t) \\ \dot{z}_M(t) \end{bmatrix} = \begin{bmatrix} 1 & 0 & 0 & 0 \\ 0 & 1 & 0 & 0 \\ 0 & 0 & 1 & 0 \\ 0 & 0 & 0 & 1 \end{bmatrix} \begin{bmatrix} x_1 \\ x_2 \\ x_3 \\ x_4 \end{bmatrix} \tag{3.22}$$

Now with the frequency domain and the time domain solutions defined for the quarter car model, the input excitation (z_r) can be further defined with the power spectral density modeling approach used to model road profiles.

3.2 Power Spectral Density (PSD) Road Modeling

Based on the quarter model detailed in section 3.1, the input disturbance z_r can take on a variety of amplitudes and trends (step, ramped, sinusoidal, periodic, etc...). As a basis for comparison, z_r taking on any of the mentioned trends with a given amplitude is sufficient for evaluating the performance of a given suspension system. If the objective of an analysis is to evaluate a suspension system under realistic excitation conditions, this approach is inadequate. In order to accurately model realistic excitation conditions for the evaluation of the quarter car model, road profiles should be used.

One of the most widely used approaches for road profile modeling is the method outlined in ISO 8608:1995 *Mechanical vibration-Road surface profiles–Reporting of measured data*. This standard details an approach for the compilation and comparison of measured vertical road profile data [1]. From this standard the sections of interest are*Annexes B & C*. Annex B details an approach for characterizing road profile data into the developed road profile classifications; and also a curve-fitting model is presented for the characterization of spectral data [1]. Annex C provides general information with respect to the use of the road profile data for studies related to comfort, suspension systems, and spectral data [1]. The following subsections will detail the modeling approach used for road modeling and reconstruction.

3.2.1 Road Modeling

Roads in general have a variety of irregularities associated with them resulting from a multitude of factors. These factors can range from grading, weather events (extended periods of hot and cold weather), physical damage from heavy vehicles, accumulated damage from passenger vehicles, and oxidation [34]. In general, road profiles can be modeled under the assumption that they consist of random fields which are real-valued, have a zero mean, remain stationary, and have a Gaussian distribution [36]. To mathematically model these assumptions, power spectral density (PSD) functions can be used in the spatial domain. The following empirical model is widely accepted in literature as a means of adequately modeling the relationship between power spectral density function and spatial frequency:

$$G_d(n) = C_{sf} n^{-w} \tag{3.23}$$

In equation (3.23), $G_d(n)$ is the power spectral density function representing the road surface elevation, n is the spatial frequency (inverse of wavelength, $1/\lambda$), C_{sf} is determined experimentally, and w is an assumed value(typically $w = 2$ when velocity is constant [1]). From equation (3.23) it can be seen that as the value of w increases the dominance of the longer wavelengths becomes more apparent while suppressing the shorter wavelengths [36]. Therefore it is common to use a more elaborate version of equation (3.23) to address this issue. The extended version of equation (3.23) is as follows:

$$G_d(n) = \begin{cases} G_d(n_0)(n/n_0)^{-w_1} & \text{, if } n \geq n_0 \\ G_d(n_0)(n/n_0)^{-w_2} & \text{, if } n \leq n_0 \end{cases} \tag{3.24}$$

In equation (3.24) n_0 represents the reference spatial frequency (typically, $n_0 = 1/2\pi$), $G_d(n_0)$ is the degree of of road roughness at the reference spatial frequency, and all other presented variables maintain the nomenclature defined in equation (3.23). Typically for modeling equation (3.24) w_1 and w_2 take on the values of 2 and 1.5 respectively [38]. In order to evaluate equation (3.24) the value for the degree of road roughness ($G_d(n_0)$) must be determined. From the ISO 8608 standard the following table was recreated. This table tabulates the values for the degree of road roughness based on the road classification outlined in this document.

	Degree of Roughness $G_d(n_0), 10^{-6}\text{m}^2/\text{cycles/m}$	
Road Class	Range	Geometric Mean
A (Very Good)	< 8	4
B (Good)	8-32	16
C (Average)	32-128	64
D (Poor)	128-512	256
E (Very Poor)	512-2048	1024
F	2048-8192	4096
G	8192-32768	16384
H	> 32768	65536

Table 3.1: Road roughness classification outlined in ISO:8608 [1].

Now by using equation (3.24) and the geometric mean values shown in Table 3.1; the ISO classification of road surfaces can be recreated.

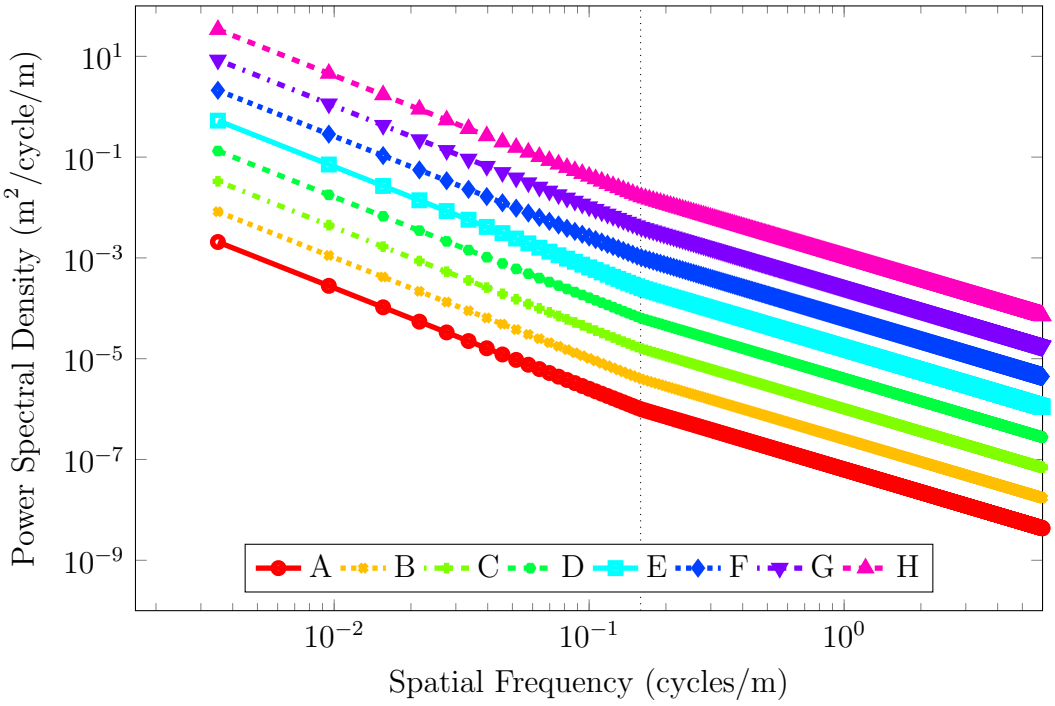

Figure 3.3: ISO 8650 Road Roughness Classification at Geometric Mean.

In Figure 3.3 the dotted vertical line denotes the reference spatial frequency point of ($n_0 = 1/2\pi$). This figure illustrates the wide distribution between the various ISO 8608 road classifications tabulated in Table 3.1 ranging from *Very Good* to beyond *Very Bad*. With the road roughness now defined the road reconstruction modeling can take place.

3.2.2 Road Reconstruction

After defining and obtaining the road roughness characteristics of the various roads outlined in ISO 8608, it is of interest to further transform the data into a form that could be used as an input in the quarter car model. In order for this data to be directly input into the previously defined quarter car model, it should be in the form of a height versus distance or a height versus time relationship. In order to simulate the height versus distance

relationship the following sum of sines series can be used:

$$z_r(x) = \sum_{m=1}^{M} s_m \sin(2\pi m \Delta n x + \phi_m) \tag{3.25a}$$

$$s_m = \sqrt{2G_d(m\Delta n)\Delta n} \tag{3.25b}$$

In equations (3.25a) and (3.25b) s_m is the amplitude of the disturbance harmonics from the power spectral density modeling, Δn is the spatial frequency width (typically $\Delta n = 2\pi/L$ where L is the length road segment being considered), and ϕ_m is a random phase angle (between $0 - 2\pi$). By evaluating equations (3.25a) and (3.25b) the distance versus height relationship can used for road profile reconstruction. The following figure reflects a sample of reconstructed roads (A through D) using these relationships.

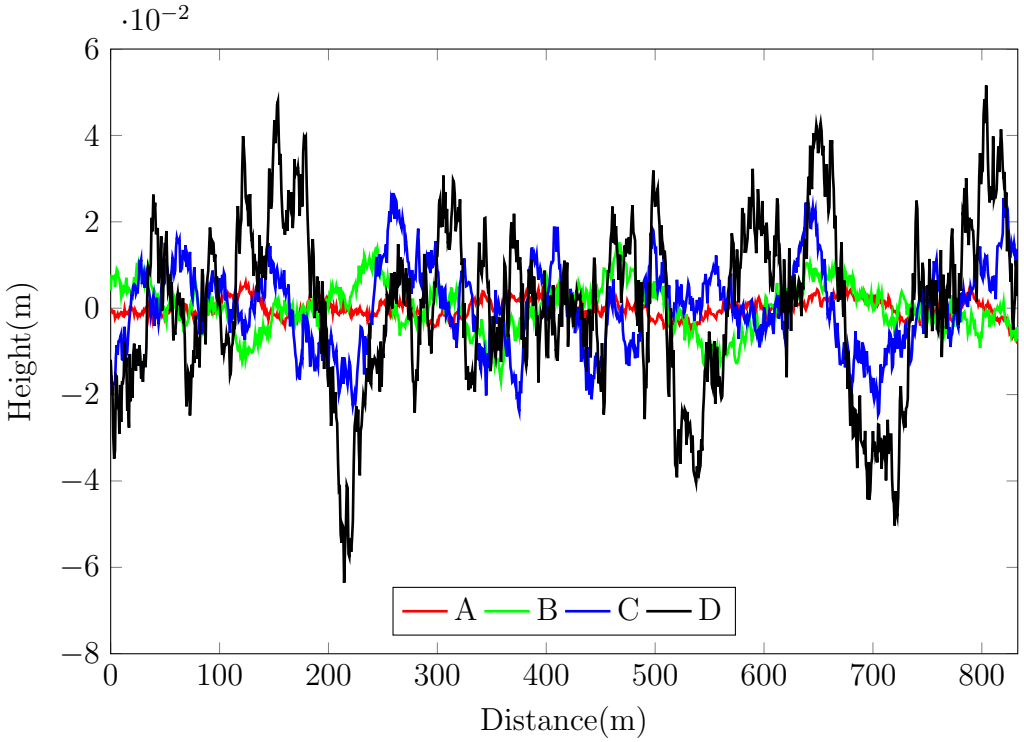

Figure 3.4: ISO 8608: 1995 Reconstructed Road Profile Height vs. Distance Relationship(at Geometric Mean).

As an alternative to the height versus distance relationship shown above, equation (3.25a) can be further modified to output a height versus time relationship directly. By assuming that a vehicle is traveling at constant velocity the following relationship can be used:

$$z_r(t) = \sum_{m=1}^{M} s_m \sin(m(\frac{2\pi}{L}v)t + \phi_m) \tag{3.26}$$

In equation (3.26), v is the velocity of the vehicle (m/s) and the remaining variables maintain the previously defined nomenclature. By assuming a constant velocity of $40 kph$ or approximately $11.11\, m/s$ and evaluating equations (3.26) and (3.25b), the following figure can be created illustrating the height versus time relationship for a sample of reconstructed roads (A through D).

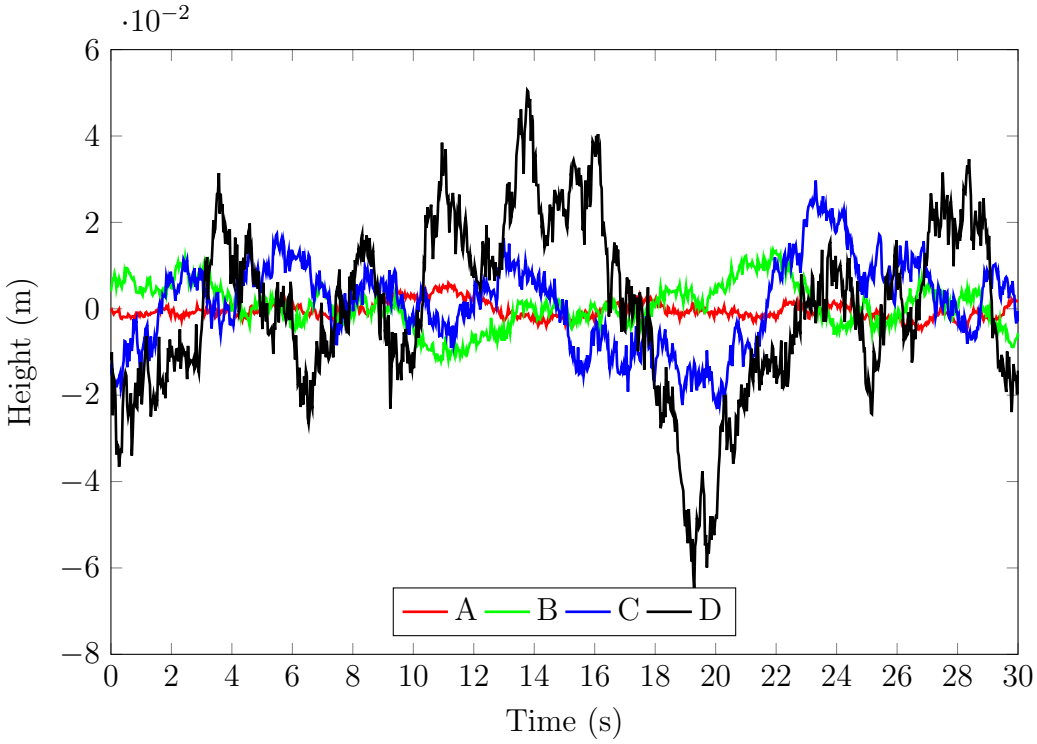

Figure 3.5: ISO 8608: 1995 Reconstructed Road Profile Height vs. Time Relationship(at Geometric Mean $v = 40$ kph).

Now with the road modeling defined this can act as a direct input into the previously defined quarter car model to evaluate the damping characteristics of a given system.

3.3 Vehicle Damping Evaluation

Based on the previously defined models for the quarter car and road, a numerical evaluation of a typical passive suspension system can be completed. In order to complete this numerical evaluation values for the mass of the suspended and unsrung (M, and m respectively) masses must be known; as well as the stiffness for the main spring, tire, and the damper in the suspension system (k_s, k_t, and c_d respectively). The following table reflects typical values for these parameters [33]:

Variable	Value	Units	Description
M	400	kg	Suspended Mass
m	50	kg	Unsprung Mass
k_s	20,000	N/m	Spring Stiffness
k_t	200,000	N/m	Tire Stiffness
c_d	3,000	$N \cdot s/m$	Damper Coefficient

Table 3.2: Typical Vehicle Quarter Car Model Parameters [33].

Now by substituting the values shown in Table 3.2 into equations (3.10), (3.12), and (3.13), these transfer functions can be evaluated over a frequency band of 0-30 Hz (which a suspension system could be exposed to during normal operation). The following figures reflect the results of this evaluation:

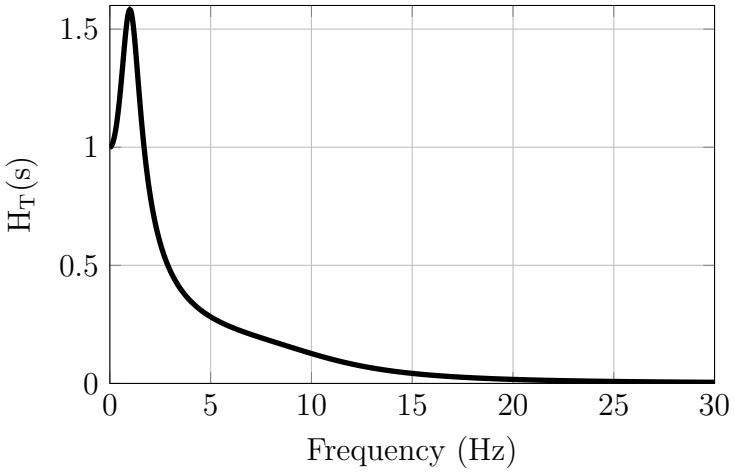

Figure 3.6: Transmissibility Transfer Function.

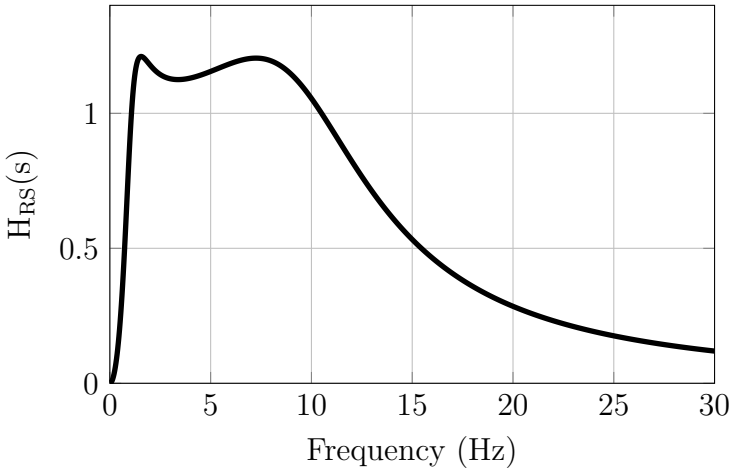

Figure 3.7: Rattle Space Transfer Function.

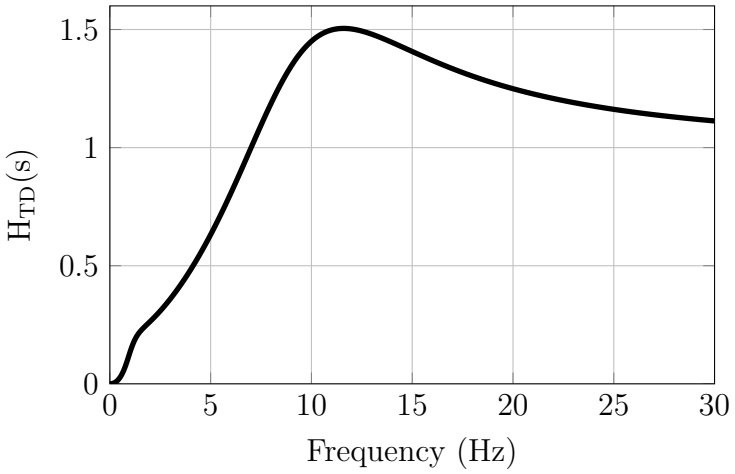

Figure 3.8: Tire Deflection Transfer Function.

Figures 3.6, 3.7, and 3.8 reflect the transfer functions for the transmissibility ratio, rattle space and tire deflection respectively. In Figures 3.6 and 3.7 it can be observed that the peak amplitudes occur between the $0 - 5\,Hz$ interval, and in Figure 3.8 the peak occurs between the $10 - 15\,Hz$ range. The peaks on these plots can be further defined by calculating the respective natural frequencies of the suspended and unsprung masses.

The following equations represent the two natural frequencies of the system.

$$f_M = \frac{1}{2\pi}\sqrt{\frac{k_s k_t}{(k_s + k_t)M}} \tag{3.27a}$$

$$f_m = \frac{1}{2\pi}\sqrt{\frac{k_s + k_t}{m}} \tag{3.27b}$$

By evaluating equations (3.27a) and (3.27b) based on the given values in Table 3.2, $f_M = 1.07\ Hz$ and $f_m = 11.8\ Hz$ illustrating that both values fall within the region where the peaks occur for all plotted transfer functions. Based on the shown transfer functions and the previously defined equations, it is of interest to know how the system response would vary due to changes in the spring stiffness, damping coefficient, and tire stiffness in general (k_s, c_d, k_t respectively).

Decreasing the spring stiffness (k_s), would decrease the value of the natural frequency of the suspended mass. This would result in a lower acceleration of the suspended mass at higher frequencies; on the other hand it would increase the overall travel of the suspension at lower frequencies. By increasing the value of the damping coefficient (c_d), the amplitude of the peak shown on the tramissibility transfer function would decrease; which in turn increases the ride quality at or near the first natural frequency. At frequencies beyond this point, the change would result in a larger average magnitude of excitation due to the less aggressive transition from the point of resonance of the suspended mass. Finally by increasing the tire stiffness (k_t), the natural frequency of the unsprung mass would increase and a decrease in the rate at which the tire deflection transfer function approaches its peak would be realized. This change would result in better overall road-holding characteristics.

Now by using the previously defined state space model (3.22) and road model (3.26) as an input, the quarter car model can be numerically evaluated. The following figure reflects the various responses of the suspended and unsprung masses respectively.

From Figure 3.9 it can be seen that the magnitude of excitation experienced by the suspended mass is always less than that experienced by the unsprung mass (which illustrates the suspension systems isolation characteristics). From the Figure 3.9a) the suspended mass displacement is representative of the average of the usprung mass displacement (equivalent to the effect of applying a *moving average* filter to a data set). Figures 3.9b) and c) illustrate a similar trend although their equivalents in terms of filtering could be considered *rms* and *mean* filters respectively. Now with the mechanical aspect of the system defined, the following sections will outline the electromagnetic modeling approach analytically and numerically through a finite element approach.

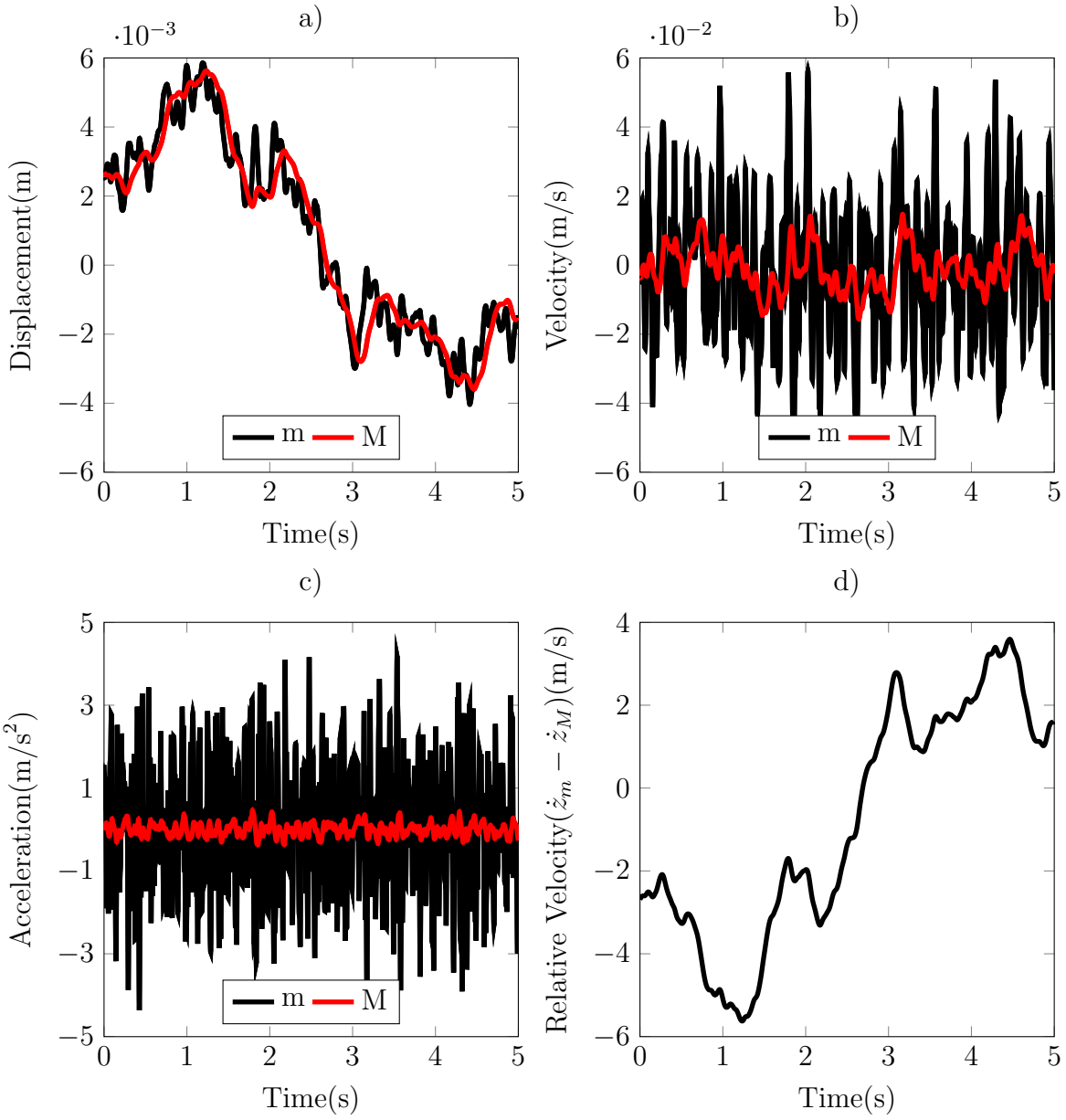

Figure 3.9: a) Quarter Car Model Suspended(M) and Unsprung(m) Mass Displacement. b) Quarter Car Model Suspended(M) and Unsprung(m) Mass Velocity. c) Quarter Car Model Suspended(M) and Unsprung(m) Mass Acceleration. d) Quarter Car Model Suspended(M) and Unsprung(m) Mass Relative Velocity.

3.4 Analytical Electromagnetic Modeling

As previously discussed, the variable damping component in the proposed design will be provided based on an electromagnetic system. As defined in the linear topology subsection, the basic linear topology consists of a series of permanent magnets (typically configured in *Halbach Array*), and coils. The relative motion between the magnets and coils induces a voltage which can be used to produce force, or alternatively the induced voltage can be harvested. Therefore the parameters of interest in the modeling of the electromagnetic system become the induced voltage, force, and current (V, F, and i respectively).

The linear topology can be configured in a variety of manners ranging from stationary coils and a moving radially magnetized magnetic stack, to a system using axially magnetized magnets and iron poles (with all other permutations in between). For the purposes of this modeling it is assumed that the configuration will consist of stationary coils, axially magnetized magnets, and iron poles. The following figure is a schematic representation of the proposed electromagnetic system:

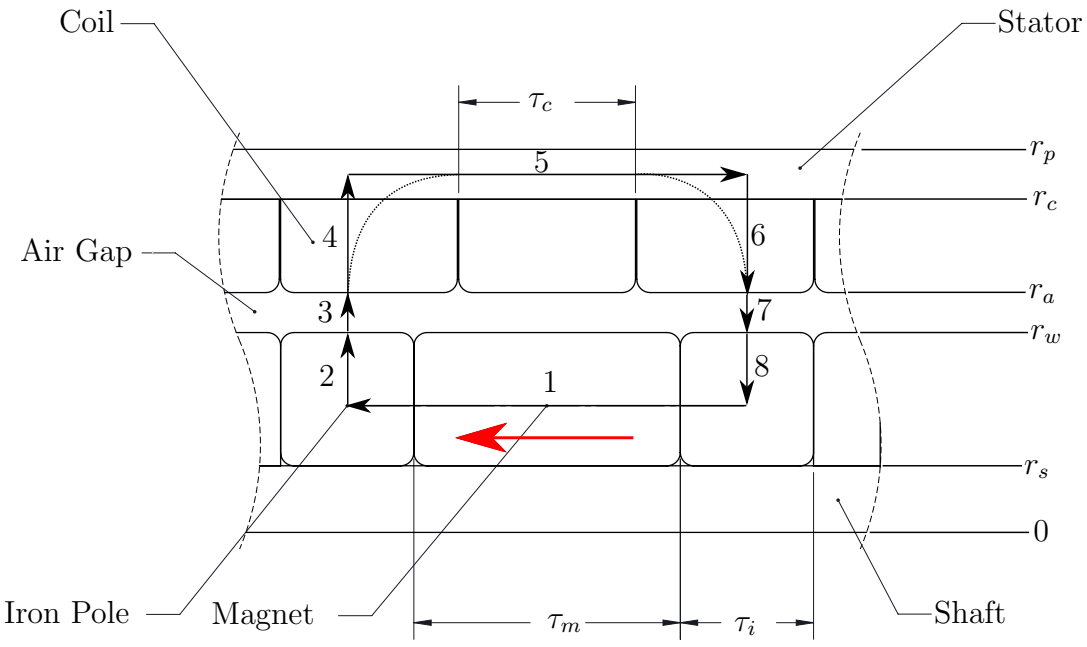

Figure 3.10: Proposed Design Electromagnetic System and Flux Circuit.

Figure 3.10 reflects a partial section of the electromagnetic system for the proposed design with the adopted nomenclature. Since the system is symmetric about the central

axis(denoted by 0 in Figure 3.10) only a quarter of the system requires analysis. The following table reflects the definitions and units for the provided nomenclature:

Variable	Units	Description
r_s	mm[in]	Radius of Piston Shaft
r_w	:	Outside Radius of Magents/Iron Poles
r_a	:	Outside Radius of Air Gap
r_c	:	Outside Radius of Coil
r_p	:	Outside Radius of Conductor Tube
τ_m	:	Magnet Thickness
τ_i	:	Iron Pole Thickness
τ_c	:	Coil Thickness

Table 3.3: Proposed Design Electromagnetic System Nomenclature.

The premise of the design is that the shaft has a series of iron poles and axially magnetized magnets attached to it, and a series of the coils that are concentric to the shaft. The purpose of the iron poles is to redirect the axial magnetic flux being passed by the magnets in the radial direction to induce a voltage in the coils.The coils are connected to the stator which is stationary. The purpose of the stator is to complete an electric circuit. The purpose of the air gap is to ensure relative non-contact motion between the coils and magnetic/ iron pole stack. Minimizing the air gap $(r_a - r_w)$ leads to better overall performance of the system due to less divergence of the redirected flux field.

From classical electromagnetic theory, Faraday's law states: the change of total flux in a closed circuit results in an induced electromotive force proportional to the rate of change of flux through the integral path [43]. Lenz's law states that the induced magnetic field produced by the induced current will oppose the direction of the original magnetic field. The Faraday-Lenz law can be expressed mathematically by the following equation:

$$V_{emf} = -\frac{d\lambda}{dt} = -N\frac{d\psi}{dt} \tag{3.28}$$

Where V_{emf} represents the electromotive force in volts, λ and ψ represent the flux through a loop, and N is the number of turns in a multi-turn coil. In order to quantify the force produced by an electromagnetic system, Lorrentz's law can be used. Lorrentz's law is defined by the following relationship:

$$\boldsymbol{F_E} = \oint Nid\boldsymbol{l} \times \boldsymbol{B} \tag{3.29}$$

Where F_E represents the force experienced by a multi-turn conductor, i is the induced current in a conductor,N is the number of turns in the multi-turn conductor, $\boldsymbol{l}$ is the current path, and $\boldsymbol{B}$ is the magnetic flux density. Although equations (3.28) and (3.29) define two of the three previously defined parameters of interest, the flux and magnetic flux density in both equations are unknown. In order to solve for the flux and magnetic flux respectively, the lumped magnetic circuit model can be used [28] [24]. Referring back to Figure 3.10, the magnetic circuit for the electromagnetic system is represented by the black arrows, the red arrow defines the poling direction of the magnet, and each labeled segment represents a section of interest based on the lumped magnetic circuit model. Using the lumped magnetic circuit model and Ampere's law the following equation can written:

$$\oint_c \boldsymbol{H} \cdot d\boldsymbol{l} = 0 = \int_1 \boldsymbol{H} \cdot d\boldsymbol{l} + \int_{2,8} \boldsymbol{H} \cdot d\boldsymbol{l} + \int_{3,7} \boldsymbol{H} \cdot d\boldsymbol{l} + \int_{4,6} \boldsymbol{H} \cdot d\boldsymbol{l} + \int_5 \boldsymbol{H} \cdot d\boldsymbol{l} \tag{3.30}$$

In equation (3.30), $\boldsymbol{H}$ is the magnetic field intensity, $d\boldsymbol{l}$ is an infinitesimal element of the closed integral path c, and subscripts one through eight are the various flux paths defined in Figure 3.10. By substituting in relationships for the various magnetic field intensities shown in equation (3.30) the following equation can be written:

$$\oint \boldsymbol{H} \cdot d\boldsymbol{l} = H_M(\tau_m + \tau_i) + 2\int_{r_s}^{r_w} \frac{B_{IP}}{\mu_0 \mu_{IP}} dr + 2\int_{r_w}^{r_a} \frac{B_{AG}}{\mu_0} dr + 2\int_{r_a}^{r_c} \frac{B_C}{\mu_0 \mu_c} dr - \frac{B_S \tau_c}{\mu_0 \mu_s} \tag{3.31}$$

In equation (3.31) H_M is the magnetic field intensity of the permanent magnet, B_{IP}, B_{AG}, B_C, and B_S represent the various magnetic flux densities for the iron pole, air gap, coil, and stator respectively, μ_0 is the permeability of free of space, and μ_{IP}, μ_c and μ_s represent the relative permeabilities of the iron pole, coil, and stator. Now with the lumped magnetic circuit defined in terms of the various magnetic flux densities (3.31), if it is assumed that there is no leakage flux in the system the following relationship can be used to represent the conservation of flux (this relationship is also known as Gauss's law for magnetic fields; which one of Maxwell's equations):

$$\oint \boldsymbol{B} \cdot dA = 0 \tag{3.32}$$

By applying equation (3.32) to the defined flux circuit the following equations can be written:

$$B_M A_M - B_{IP} A_{IP} = 0 \tag{3.33a}$$

$$B_M A_M - B_{AG} A_{AG} = 0 \tag{3.33b}$$

$$B_M A_M - B_C A_C = 0 \tag{3.33c}$$

$$B_M A_M - B_S A_S = 0 \tag{3.33d}$$

In equations (3.33a), (3.33b), (3.33c), (3.33d); A_{IP}, A_{AG}, A_C, and A_S represent the areas through which the flux projection occurs for the iron pole, air gap, coil and stator respectively. Now by substituting in relationships for the projection areas shown in the equations above, the following relationships can be derived:

$$B_{IP} = \frac{B_M \pi (r^2 - r_s^2)}{\pi r \tau_i} \text{ ,where } r_s < r < r_w \tag{3.34a}$$

$$B_{AG} = \frac{B_M \pi (r_w^2 - r_s^2)}{\pi r \tau_i} \text{ ,where } r_w < r < r_a \tag{3.34b}$$

$$B_S = \frac{B_M \pi (r_w^2 - r_s^2)}{\pi (r_p^2 - r_c^2)} \tag{3.34c}$$

From equations (3.34a), (3.34b),and (3.34c) it is clear that the relationships substituted in for the various areas correspond to the cross-sectional areas and surface areas respectively. In order to model the flux projection area into the coil it is assumed that the flux field in the air gap diverges in a linear manner between the limits of the inside and outside radii of the coil (r_a and r_c respectively) [9]. This assumption is derived based on the air gap ($r_a - r_w$) being significantly smaller than the coil limits ($r_c - r_a$) in order to achieve optimal operation of the electromagnetic system. By making this flux divergence assumption it allows for the magnetic circuit to be analyzed solely in the radial direction while accounting for the change in the flux through the coil with a linear approach. An alternative to this approach would be to attempt to model the highly non-linear flux distribution through the

coil by accounting for the radial and axial components of the flux with the norm of these to vectors(following dotted line between sections 3 and 5 of flux circuit). The following schematic illustrates how the assumed flux area is defined.

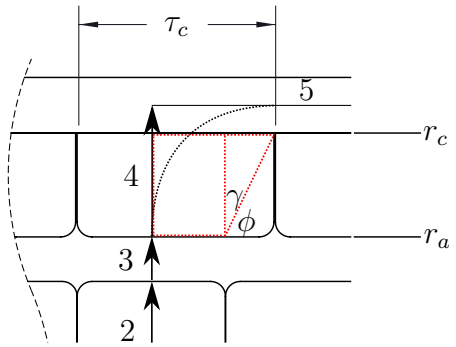

Figure 3.11: Flux Projection Area in Coil.

From Figure 3.11 the area of flux projection is defined by the red dotted lines. When $r = r_a$ the area is equal to the area projected in the air gap (A_{AG}). As r increases the area also increases at a gradient of ϕ as defined in the figure. The following relationships can be written to define ϕ, γ, and the flux projection area in the coil as a function of r:

$$\phi = \arctan\left(\frac{r_c - r_a}{\tau_c - \tau_i}\right) \tag{3.35a}$$

$$\gamma = \frac{\pi}{2} - \phi = \frac{\pi}{2} - \arctan\left(\frac{r_c - r_a}{\tau_c - \tau_i}\right) \tag{3.35b}$$

$$A_C = 2\pi r_a \frac{\tau_i}{2} + 2\pi r(\tan(\gamma)(r)) \tag{3.35c}$$

Now by substituting equations (3.35b), and (3.35c) into equation (3.33c), the following relationship can be written:

$$B_C = \frac{B_M \pi (r_w^2 - r_s^2)}{2\pi r_a \frac{\tau_i}{2} + 2\pi r(\tan\left(\frac{\pi}{2} - \arctan\left(\frac{r_c - r_a}{\tau_c - \tau_i}\right)\right)(r))} \text{ ,where } r_a < r < r_c \tag{3.36}$$

As seen in equations (3.34a), (3.34b), (3.34c), and (3.36) all equations are solved for in terms of B_M. In order a to solve equation (3.31) a relationship must also be defined to solve for H_M. H_M can also be solved for in terms of B_M based on the remanent flux density constitutive relationship. The following relationship reflects this constitutive equation:

$$H_M = \frac{B_M - B_r}{\mu_0 \mu_r} \tag{3.37}$$

In equation (3.37) B_r is the remanent flux density of the magnet, and μ_r is the relative permeability of the magnet material. Now by substituting equations (3.34a), (3.34b), (3.34c), (3.36), and (3.37) into (3.31) and evaluating each term, the following equation can be written:

$$\int_1 \boldsymbol{H} = H_M(\tau_m + \tau_i) = \frac{B_M - B_r}{\mu_0 \mu_r}(\tau_m + \tau_i) \tag{3.38a}$$

$$\int_{2,8} \boldsymbol{H} \cdot d\boldsymbol{l} = 2\int_{r_s}^{r_w} \frac{B_{IP}}{\mu_0 \mu_{IP}} dr = \frac{-B_M(-r_w^2 + 2r_s^2 \ln(r_w) + r_s^2 - 2r_s^2 \ln(r_s))}{\tau_i \mu_0 \mu_{IP}} = c_{IP} B_M \tag{3.38b}$$

$$\int_{3,7} \boldsymbol{H} \cdot d\boldsymbol{l} = 2\int_{r_w}^{r_a} \frac{B_{AG}}{\mu_0} dr = \frac{-2B_M(r_s - r_w)(r_s + r_w)(\ln(r_a) - \ln(r_w))}{\mu_0 \tau_i} = c_{AG} B_M \tag{3.38c}$$

$$\int_{4,6} \boldsymbol{H} \cdot d\boldsymbol{l} = 2\int_{r_a}^{r_c} \frac{B_C}{\mu_0 \mu_c} dr = \frac{2B_M \pi (r_w^2 - r_s^2)}{\mu_0 \mu_c} \left(\frac{A_1(\ln(r_c - r_1) - \ln(r_a - r_1)) + A_2(\ln(r_c - r_2) - \ln(r_a - r_2))}{k_2} \right) = c_c B_M \tag{3.38d}$$

$$\int_5 \boldsymbol{H} \cdot d\boldsymbol{l} = -\frac{B_s \tau_c}{\mu_0 \mu_s} = \frac{\tau_c B_M (r_w^2 - r_s^2)}{\mu_0 \mu_s (r_p^2 - r_c^2)} = c_s B_M \tag{3.38e}$$

In equation (3.38d) the various coefficients can be further defined with the following rela-

tionships:

$$k_1 = \pi r_a \tau_i, \,\&\, k_2 = -2\pi tan\left(\frac{\pi}{2} - \arctan\left(\frac{r_c - r_a}{\tau_c - \tau_i}\right)\right) \tag{3.39a}$$

$$r_1, r_2 = \frac{k_2 r_a \pm \sqrt{(k_2 r_a)^2 - 4k_2 k_1}}{2k_2} \tag{3.39b}$$

$$A_1 = \frac{1}{r_1 - r_2}, \,\&\, A_2 = \frac{1}{r_2 - r_1} \tag{3.39c}$$

Now by substituting equations (3.38a), (3.38b), (3.38c), (3.38d), and (3.38e) into equation (3.31) and rearranging the equation to put it in terms of B_M, the following relationship can be written:

$$B_M = \frac{B_r(\tau_m + \tau_i)}{\tau_m + \tau_i + \mu_0 \mu_r (c_{IP} + c_{AG} + c_c - c_s)} \tag{3.40}$$

Now with all of the magnetic fields defined within the various components in the previously defined magnetic flux circuit, the field in the coil(B_C, equation (3.36)) can be substituted into equation (3.28) to yield a relationship defining the induced voltage in the following manner:

$$V_{emf} = -N 2\pi r B_C \frac{dx}{dt} \tag{3.41}$$

As previously mentioned and calculated in equation (3.36) the field in the coil (B_C) is not constant. Therefore in order to solve for the V_{emf} the equation must be integrated with respect to r and N in equation (3.41) needs to be changed to the number of turns in the axial direction (z) oppose to the total number of turns. Figure 3.12 reflects a schematic of a typical multi-turn coil.

In Figure 3.12 a represents the number of coil turns in the axial direction and b represents the number of turns in the radial direction. By substituting a in for N in equation (3.41) and integrating with respect to r between the radial limits of the coil (r_c, r_a)the following can be written:

$$V_{emf} = -a 2\pi \int_{r_a}^{r_c} r B_C dr \frac{dx}{dt} = \frac{-a 2\pi B_M \pi (r_w^2 - r_s^2)}{r_c - r_a}(A_3 - A_4)\frac{dx}{dt} \tag{3.42}$$

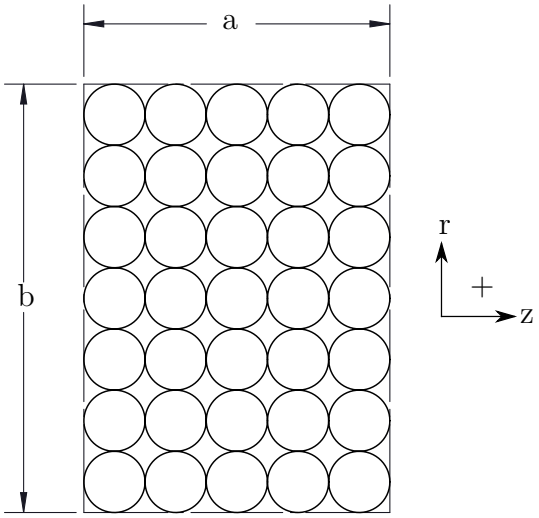

Figure 3.12: Cross-Section of Typical Multi-Turn Coil.

In equation (3.42) coefficients A_3 and A_4 can be further defined with the following relationships:

$$A_3 = \frac{\log(-k_2 r_a r_c + k_2 r_c^2 + k_1)}{2k_2} - \frac{r_a \arctan\left(\frac{\sqrt{k_2}(r_a - 2r_c)}{\sqrt{4k_1 - k_2 r_a^2}}\right)}{\sqrt{k_2}\sqrt{4k_1 - k_2 r_a^2}} \tag{3.43a}$$

$$A_4 = \frac{\log(k_1)}{2k_2} - \frac{r_a \arctan\left(\frac{\sqrt{k_2}(-r_a)}{\sqrt{4k_1 - k_2 r_a^2}}\right)}{\sqrt{k_2}\sqrt{4k_1 - k_2 r_a^2}} \tag{3.43b}$$

In equations (3.43a) and (3.43a) k_1 and k_2 are defined by equation (3.39a). By proceeding in similar manner if the equation previously defined for the field in the coil(B_C, equation (3.36)) is substituted into (3.29) the following relationship for the force can be written:

$$F = N 2\pi r B_C i \tag{3.44}$$

As was the case in equation in (3.41), B_C in equation (3.44) is not constant. By proceeding a similar manner as previously descried to develop equation (3.42) the following expression

can be written to define the force F:

$$F = -a2\pi i \int_{r_a}^{r_c} rB_C dr = \frac{-a2\pi i B_M \pi (r_w^2 - r_s^2)}{r_c - r_a}(A_3 - A_4) \tag{3.45}$$

Based on the relationship defined for the induced voltage in the coil, this equation can be used to derive the current(i) in the coil as well. By assuming the electrical circuit for the electromagnetic system consists of a resistive element representing the external load on the system, and an inductor representing the coil itself; the following electrical circuit is representative for the system. Figure represents a schematic of the equivalent electrical circuit for the electromagnetic system.

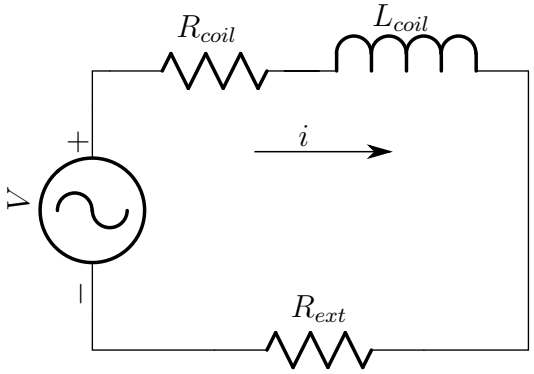

Figure 3.13: RL Circuit.

In Figure 3.13, the shown AC power source (V) represents the coil, R_{coil} and L_{coil} represent the resistance of the coil and inductance respectively, and R_{ext} represents the resistance of an external load being applied to the system. From Figure 3.13 it can be seen that the proposed circuit is representative of a RL series circuit; and based on Kirchhoff's voltage law the following expression can be written to model the circuit:

$$V(t) = V_R(t) + V_L(t) \tag{3.46}$$

In equation (3.46), $V(t)$, $V_R(t)$, and $V_L(t)$ can be further defined with the following relationships:

$$V(t) = V_{emf} \cos \omega t \tag{3.47a}$$

$$V_R(t) = (R_{coil} + R_{ext})i(t) \tag{3.47b}$$

$$V_L(t) = L_{coil}\frac{di}{dt} \tag{3.47c}$$

Equation (3.47a) is based on the general form of an alternating current signal assuming its amplitude is equal to the induced voltage in the coil (V_{emf}), and equations (3.47b) and (3.47c) are general electrical equations for modeling the voltage drop across a resistor and inductor respectively. Now if equations (3.47a), (3.47b), and (3.47c) are substituted into equation (3.46) the following can be written:

$$V(t) = (R_{coil} + R_{ext})i(t) + L_{coil}\frac{di}{dt} \tag{3.48}$$

A possible solution to equation (3.48) is as follows:

$$i(t) = i_0 \cos(\omega t - \phi) \tag{3.49}$$

In equation (3.49) i_0 and ϕ can be further defined by the following relationships:

$$i_0 = \frac{V_{emf}}{\sqrt{(R_{coil} + R_{ext})^2 + (\omega L_{coil})^2}} \tag{3.50a}$$

$$\phi = \arctan\left(\frac{\omega L_{coil}}{R_{coil} + R_{ext}}\right) \tag{3.50b}$$

Now if equations (3.50a) and (3.50b) are substituted into equation (3.49) the following expression can be written defining current as a function of time:

$$i(t) = \frac{V_{emf}}{\sqrt{(R_{coil} + R_{ext})^2 + (\omega L_{coil})^2}} sin\left(\omega t - \arctan\left(\frac{\omega L_{coil}}{R_{coil} + R_{ext}}\right)\right) \tag{3.51}$$

Now with all of the previously identified variables of interest (V, F, and i) defined, two additional derived expressions can be defined for the total force (F_t) produced by the system, and the total power (P_t). The following two equations represent these relationships:

$$F_t = Fn \tag{3.52}$$

$$P_t = ni^2R \tag{3.53}$$

In equations (3.52) and (3.53), n represents the number of iron pole/magnet stacks, F is defined by equation (3.44), i is defined by equation (3.51), and R is the total resistance in the system($\sqrt{(R_{coil} + R_{ext})^2 + (\omega L_{coil})^2}$).

As an alternative approach to modeling the electromagnetic system analytically, a finite element method (FEM) can be used. The following section of this thesis will outline the FEM approach.

3.5 Finite Element Electromagnetic Modeling

As an alternative to the analytical model shown in the previous section, a finite element method can be used. In order to model the previously defined electromagnetic system, COMSOL MultiPhyics was used. COMSOL MultiPhysics was chosen as the modeling package due to its ability to combine multiple physics domains into a single model. Being able to model multiple physical domains simultaneously allows for the analysis to account for the coupling effects of the various domains. In order to model the electromagnetic system in COMSOL a two dimensional axis symmetric model was created with the inclusion of the *Magnetic Fields*, *Moving Mesh*, and *Electrical Circuit* modules.

In order to model the system, the geometry was modeled within the COMSOL interface using parameters to define all of the dimensions and positions. Using the parameter approach for modeling allowed COMSOL to dynamically sweep through various permutations of the model during optimization and analysis at a variety of test points in an automated manner. After modeling the geometry all materials were assigned to the model based on the built-in material library. The *Magnetic Fields* module allowed for the definition of the permanent magnets using Ampere's law, the definition of the multi-turn coil domains, and the calculation of Lorrentz force. The *Moving Mesh* model was used to evaluate the model during a time-dependent study. Using this module allowed for the input of an excitation into the system to simulate the output forces and voltages. Finally the *Electrical Circuit* module was used to add external circuits to the previously defined coil domains. The following figure reflects a sample of the magnetic flux density plot produced by COMSOL for the electromagnetic system.

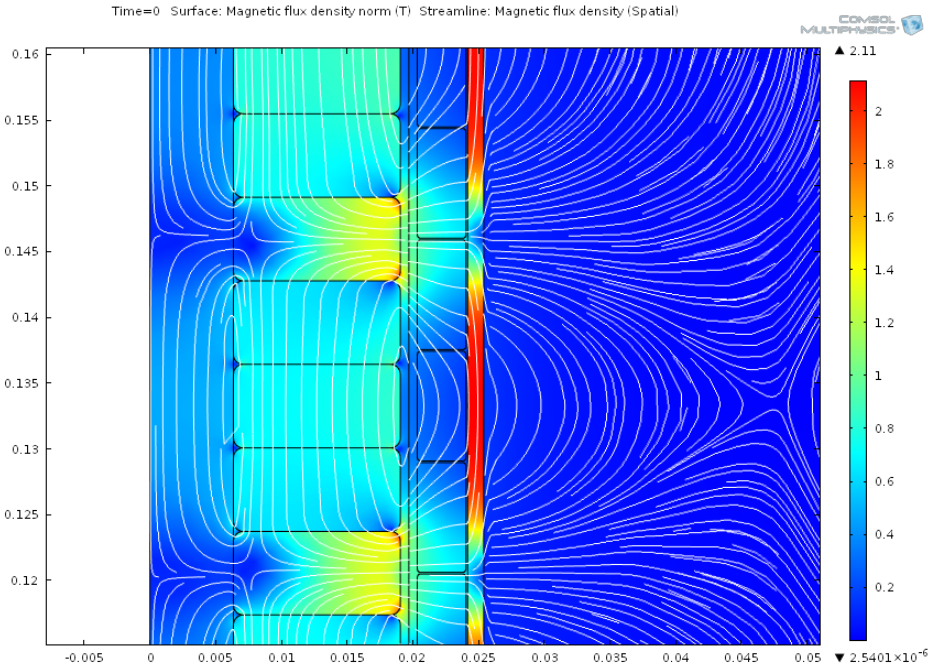

Figure 3.14: Sample Output from Comsol MultiPhysics.

The subsequent sections of this thesis will outline the geometry and parameters used as inputs into this model based on the mechanical and electromagnetic system designs. In addition the results from this model once evaluated with the final geometry and parameters, will be compared to the experimental results to further validation.

Chapter 4

Hybrid Damper Design

The design of the hybrid damper is a critical aspect of this thesis because it defines how the proposed concept of integrating a passive hydraulic damper and the linear motor topology can be physically achieved. This must be achieved in order to develop a prototype for further experimental characterization and model validation. The following subsections of this chapter will outline the mechanical design, electromagnetic design and optimization, and finally the design of the electronics for data acquisition and management of the damper output.

4.1 Mechanical Design

The purpose of this section is detail the mechanical design of the proposed hybrid damper. The following subsections will cover general passive damper construction, a proposed conceptual design, and finally the actual prototype design.

4.1.1 Damper Construction

Mechanically, the objective of the design is to develop a damper that is suitable for mid-size passenger vehicles. Therefore a logical starting point in the design process is to investigate existing passive damper designs. In general there are two types of passive dampers used in automotive applications: mono-tube and twin-tube. Beginning with the mono tube damper, the following figure reflects the typical construction.

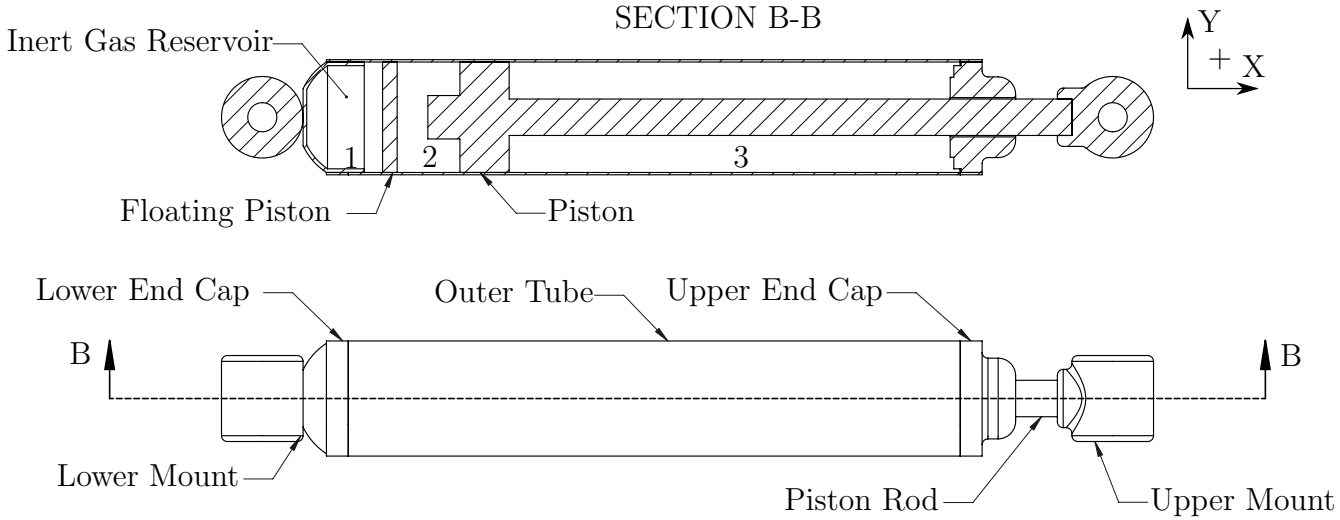

Figure 4.1: Mono Tube Design.

From Figure 4.1 it can be seen that the major components of the mono tube damper are the two pistons (floating and stationary piston attached to piston rod), the piston rod, and the main working chamber enclosed within the outer tube and capped by the lower and upper end caps (reservoirs 1,2,3). In this design, as the piston rod moves up and down during operation oil transitions through the piston (bi-direction flow) with a predefined flow restriction into reservoirs 2 and 3. The purpose of the floating piston is to dynamically regulate the volume of reservoirs 1 and 2. As the piston rod assembly moves in the $+X$ direction, reservoir 1 decreases in volume to increase the working volume of reservoir 2. Alternatively when the piston rod assembly moves in the $-X$ direction, reservoir 1 increases in volume and reservoir 2 decreases in volume. In addition, since reservoir 1 is pressurized with an inert gas (typically nitrogen or air) it also acts as a recoil mechanism when no force is applied to either end of the damper. Now with the basic operation of the mono tube damper defined, the twin tube damper operating principle can be described. Figure 4.2 reflects the typical construction of a twin tube damper.

From Figure 4.2 it can be seen that the twin tube design includes some of the mono tube components, as well as additional ones. In this design, as the piston rod assembly moves in the $+X$ direction oil is drawn from reservoir 2 (aided by the pressure of the inert gas in reservoir 1) into reservoir 3 through the pressure tube valve. In addition, oil can flow from reservoir 4 into reservoir 3 to equalize the pressures across the various reservoirs. When the piston rod assembly moves in the opposite direction ($-X$), oil in reservoir 3 flows through the pressure tube valve into reservoir 2 and any excess oil can flow into reservoir

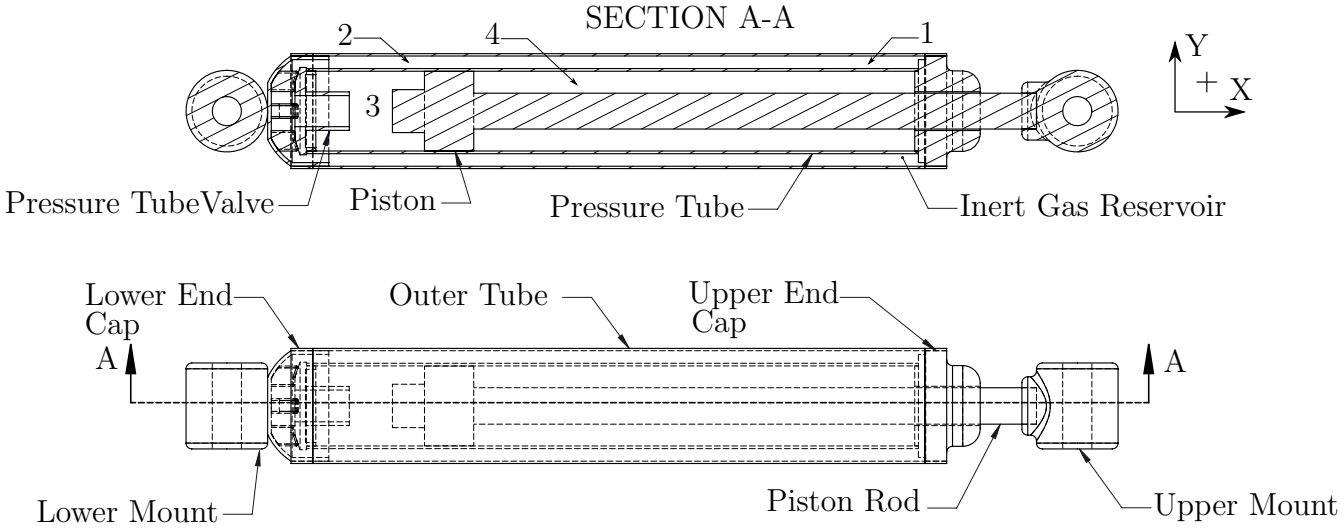

Figure 4.2: Twin Tube Design.

4. The major differences observed with the twin tube design in contrast to the mono tube design stem from the use of two main working reservoirs (2 and 3), the use of the pressure tube valve, and the nondistinct segregation between the inert gas and fluid reservoirs (1 and 2) as seen with the mono tube design (floating piston separates reservoirs).

In general mono tube dampers are more suitable for high performance applications when road holding is the objective of interest. Mono tube dampers also benefit from having less fade in damping at elevated temperatures due to the better heat transfer capacity of the construction [11]. In addition, this (construction) eliminates the cavitation of oil within the damper due to the (discrete) separation of the inert gas and working fluid. The major shortcomings of this design are its cost and comfort. The twin tube design benefits from providing better comfort for passengers, being more robust due to the pressure tube being concealed within the outer tube, and by being less expensive to manufacture overall. The disadvantages of the twin tube damper in essence are the advantages of the mono tube damper; cavitation of working medium occurs due to the non-segregation of the inert gas, and poor heat transfer characteristics as a result of the pressure tube being contained within the outer tube.

Based on the described damper constructions, the requisite background has been developed to introduce the conceptual design. The following subsection will detail the conceptual design.

4.1.2 Conceptual Damper Design

Based on the two types of dampers previously defined, the twin tube construction was chosen as the basis of the hybrid design. Intuitively it makes more sense to use the mono tube design because of its simpler construction and operation. Although the mono tube is simpler, the twin tube design was chosen because the construction was more suitable for the addition of the electromagnetic sub-system. Figure 4.3 is a schematic representation of the concept design of the hybrid damper.

From Figure 4.3 it can be seen that the core construction of the twin tube damper was maintained while adding the required components for the electromagnetic system. The electromagnetic system in the design consists of coils, permanent magnets, and iron poles (as previously defined in the modeling section). In addition, cable glands were added to the damper in order to access the coils externally and maintain a sealed environment for the hydraulic aspect of the system. From a mechanical prescriptive, support bushings were added to ensure that the pressure tube maintained concentricity with respect to the outer tube to mitigate the risk of coil damage. The bushings have been designed to include four scalloped slots to allow for oil flow. Also, as another conceptual prevision the support shaft was added to maintain the concentricity constraint. The cable glad mounting plate was added to allow for mounting of the cable glands on the cylindrical surface of the damper. From a hydraulic prescriptive, the up and down stroke adjustment valves were added to allow for the adjustment of the hydraulic system if required (unidirectional flow in each valve). In addition the inert gas inlet was included to add and remove pressure to and from the system.

Conceptually, the hybrid design is now defined and various components added to the core twin tube design have been discussed. Although the design is conceptually representative (in its current state), it would difficult to manufacture with conventional machining techniques. The following section will detail the prototype design which was built and tested.

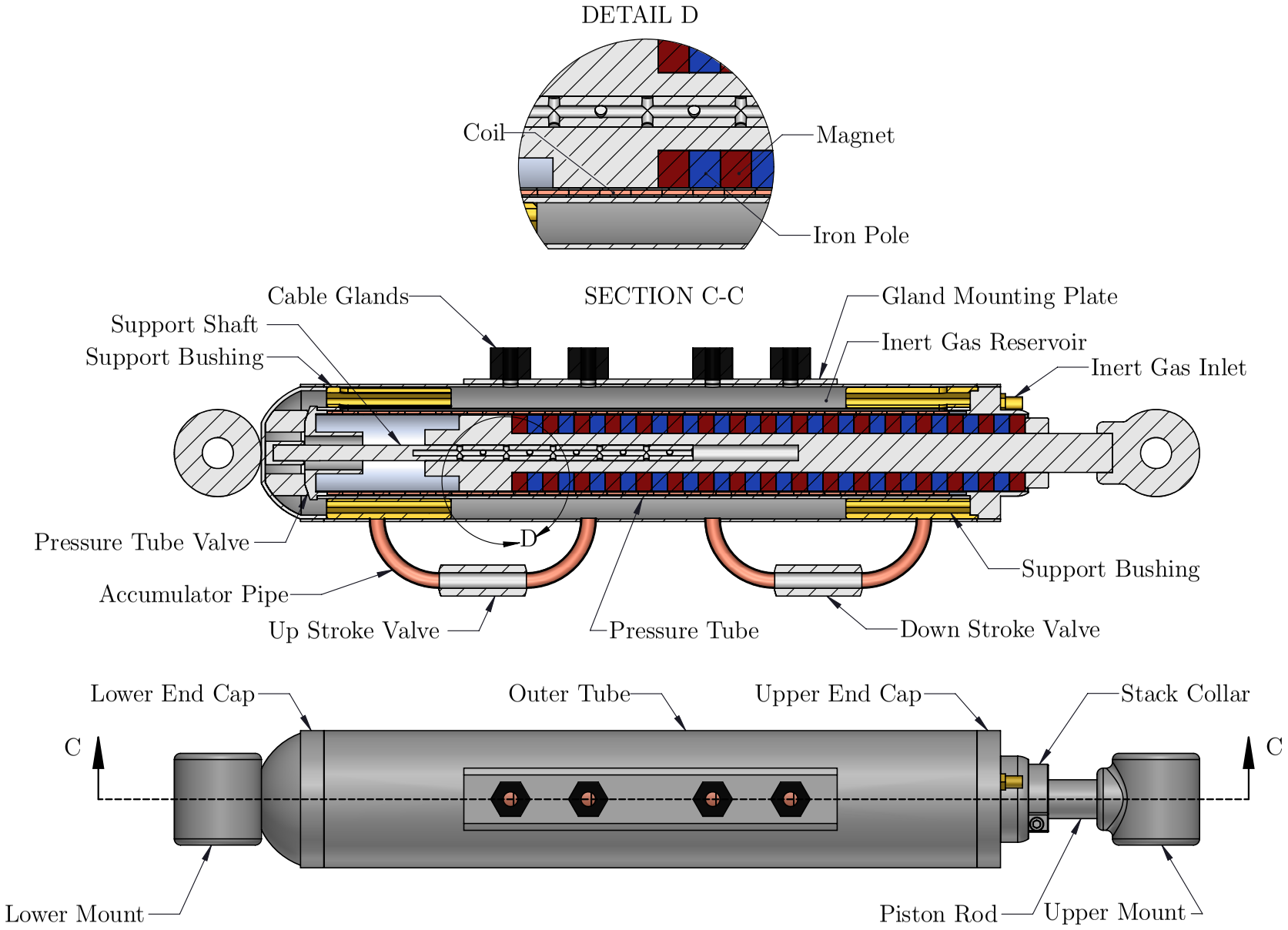

Figure 4.3: Hybrid Damper Twin Tube Conceptual Design.

4.1.3 Hybrid Prototype Design

In order to manufacture a prototype of the previously defined conceptual design, a variety of features need to be addressed. In addition, since this damper is being designed for research purposes, the prototype should be configured in a manner which allows for changes in the electromagnetic system with minimal effort. Based on these requirements the final prototype was designed and Figure 4.5 is a schematic of the final design.

From Figure 4.5 it can be seen that a variety of changes were implemented to ensure the manufacturability, adjustability, and functional requirements were met. Starting with the outer tube; its shape was changed from cylindrical to square with a cylindrical internal bore. This change was made to facilitate the mounting of external components (cable glands, temperature sensor, and hydraulic couplers) on the exterior surface of the outer tube. In addition this change allowed for the upper and lower end caps to be fastened to the outer tube. In a conventional twin tube design these end caps would be welded to the outer tube which would conflict with the adjustability requirement. Although the fastening of the upper and lower end caps addressed the adjustabilty requirement, it also introduced sealing concerns. To address the sealing issues lower and upper gaskets where added between the outer tube and end cap interfaces. In addition, three seals were added to the interior of the upper end cap (buffer, rod, wiper seals; refer to Figure 4.4a).

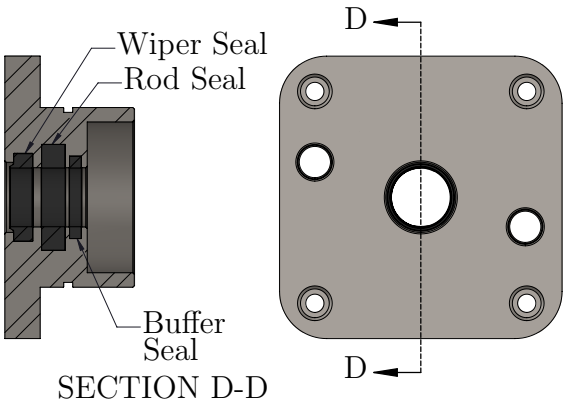

(a) Schematic of Upper End Cap with Seals.

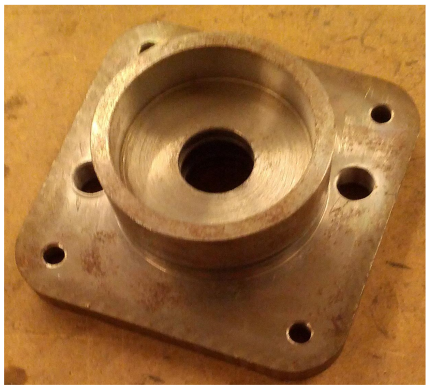

(b) Photograph of Actual Upper End Cap.

Figure 4.4: Prototype Hybrid Damper Upper End Cap.

Another key concern with the conceptual design was that the piston rod was not fully constrained within the assembly. Referring back to Figure 4.3 it can be seen that the

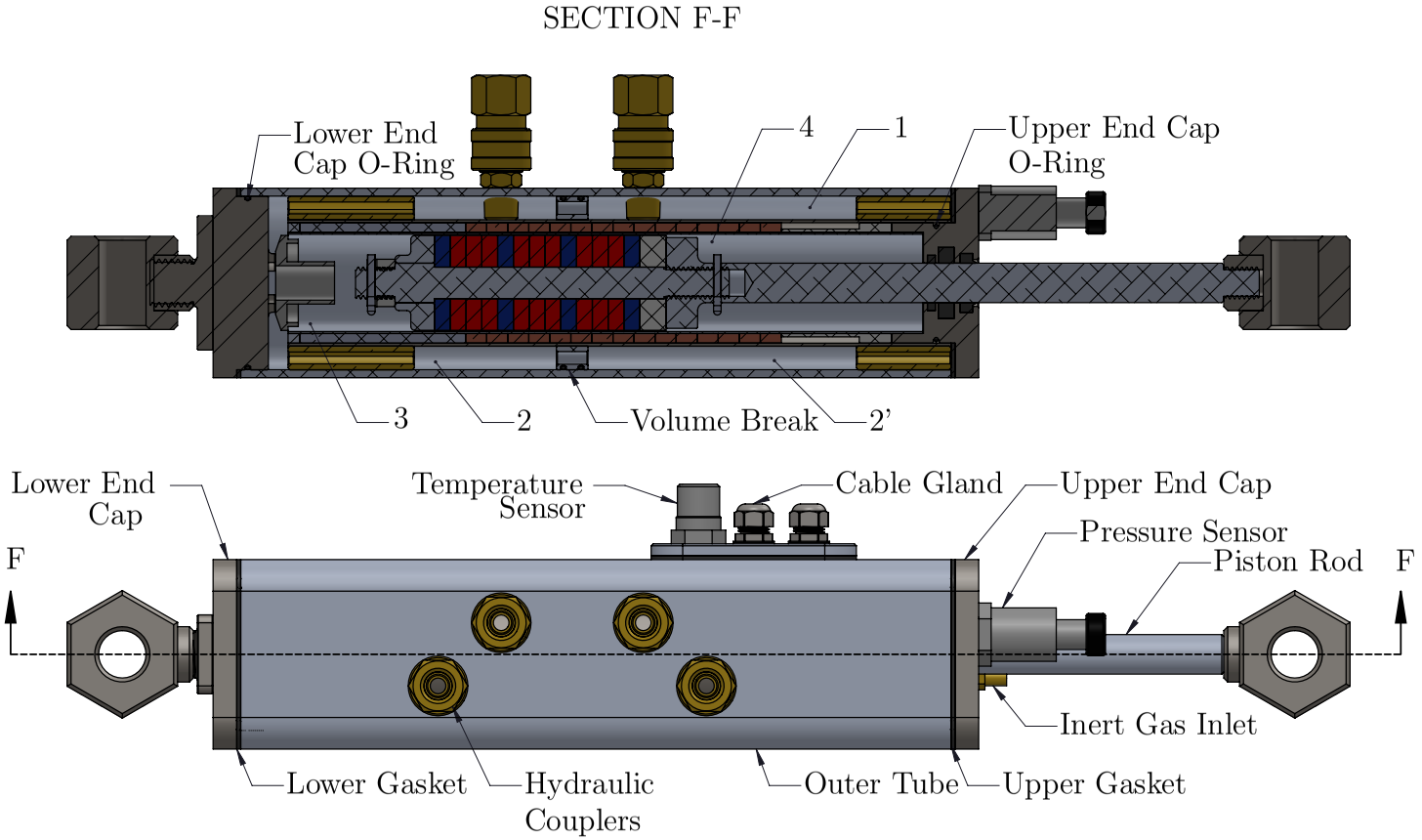

Figure 4.5: Hybrid Damper Twin Tube Prototype Design.

piston shaft could be completely removed from the assembly with no obstruction. To address this a split shaft design was developed in which the two halves of the shaft were connected with a thread and a clevis pin (refer to Figure 4.6).

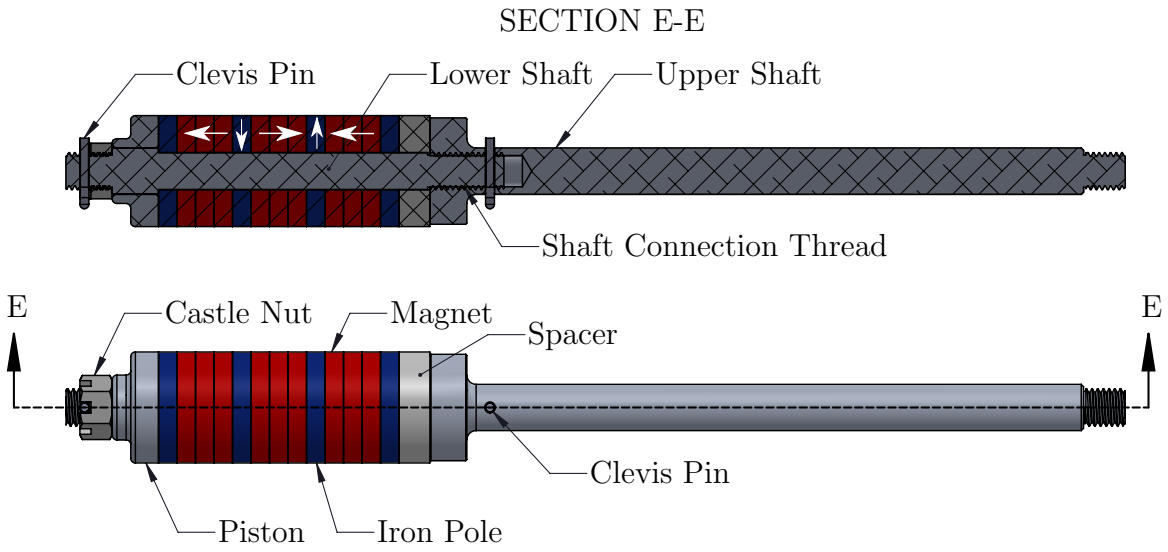

Figure 4.6: Schematic of Split Shaft Design (White arrows show poling directions of magnets and iron poles).

From a functional perspective, the conceptual piston design and up and down stroke adjustment valves would not work as intended. The issue with the conceptual piston design was that oil would not be able to flow in or out of reservoir 4 which would cause a change in the damping force characteristics. To address this, the piston external diameter was made equal to the external diameter of the magnets and iron poles to allow for oil flow around the piston shaft. Another functional issue in the design concerned the adjustment valves. From the conceptual design it can be seen that there is no physical separation between the inlet and outlet ports which leads to this design flaw. In order for these valves to function as intended reservoir 2 must be subdivided (2 and 2') such that the pairs of inlet and outlets ports are segregated. To allow for this segregation the volume break was designed (Figure 4.7 reflects a schematic of the volume break).

In order to physically implement the adjustment valves; hoses, hydraulic couples, and unidirectional flow valves were purchased and added to the damper. To finalize the prototype design, a temperature and pressure sensor were added directly to the damper to measure the internal temperature and pressure within the damper respectively.

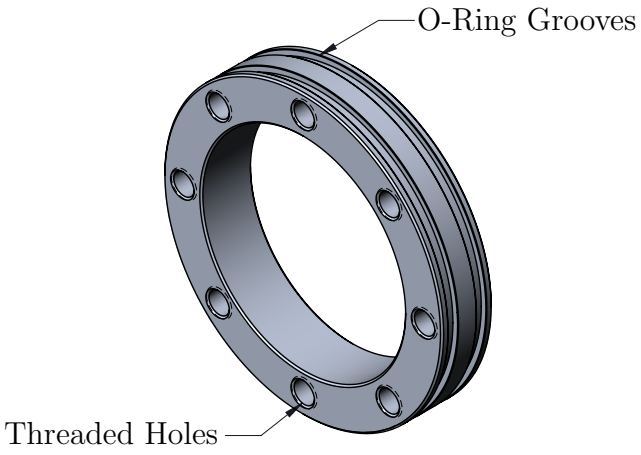

Figure 4.7: Schematic of Volume Break.

From this figure it can be seen that there are two o-ring grooves cut into the diameter of this component and a circular bolt pattern drilled through the volume break. The purpose of the o-ring groves is to seal the volume break to the internal bore of the outer tube. The purpose of the thru hole bolt pattern is to allow for different levels of separation between subdivided reservoirs 2 and 2'. This is achieved by blocking these holes with screws to change the flow characteristics between the sub-reservoirs.

Now with the prototype design defined, the size and mechanical operating parameters can be defined for the prototype. The dimensions for this prototype were derived based on an existing twin tube damper used in a mid-size passenger vehicle. The specific damper used as a point of reference was the Monroe Reflex part number 911258. The following figure is an image of this damper.

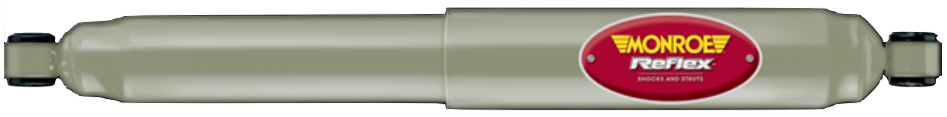

Figure 4.8: Mid-Size Passenger Vehicle Twin Tube Damper.Image reproduced from [18].

Based on the dimensions of this damper; the hybrid damper was designed to have an equivalent internal diameter of 50.8 mm (2.00 in) for the pressure tube, an equivalent

piston rod shaft size of 15.875 mm (0.625 in), and finally an upper and lower mount size diameter of 19.05 mm (0.750 in). Another dimension of interest typically associated with dampers is the travel length or stroke. Table 4.1 reflects a comparison of the travel lengths and associated dimensions for the hybrid design and the reference damper (Monroe 911258).

Parameter	Units	Monroe Damper	Hybrid Damper
Travel Length	mm[in]	206.375 [8.125]	83.820 [3.300]
Retracted Length	mm[in]	346.075 [13.625]	468.630 [18.450]
Extended Length	mm[in]	552.450 [21.750]	552.450 [21.750]

Table 4.1: Moroe Damper vs. Hybrid Damper Dimensional Comparison.

As can be seen from Table 4.1 there is a significant difference in stroke between the two dampers. The hybrid damper travel length is significantly restricted due to the stack of iron poles and magnets. Although the travel length of the hybrid damper is significantly less; based on the previously defined road modeling the travel length falls well within the excitation amplitudes experienced on typical roads. In addition the travel length for the hybrid damper falls within the limits of the reference damper, making it a viable replacement candidate . The remaining dimensions for the damper were developed based on the clearances, fits, and other design practices. The following figure reflects the envelope dimensions of the final hybrid damper as well as a photo of the prototype.

Now with the hybrid damper defined mechanically, the electromagnetic system can be fully defined. The following section will detail the electromagnetic optimization and final dimensional results for the system.

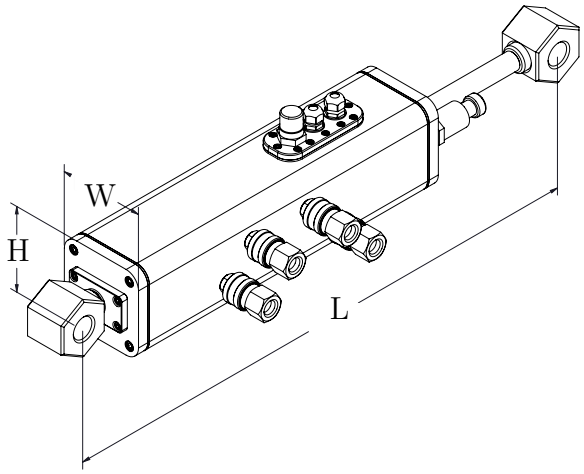

(a) Envelope dimensions of Hybrid Damper Fully Retracted. Where H=W=76.2 mm (3.0 in), and L=468.630 mm (18.450 in).

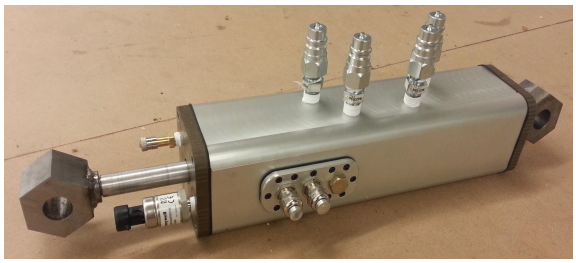

(b) Photograph of Actual of Hybrid Damper Assembly.

Figure 4.9: Prototype Hybrid Damper Assembly.

4.2 Electromagnetic Design and Optimization

Based on the previously described hybrid damper prototype design, the electromagnetic system needs to be designed, and optimized to maximize its performance. As mentioned in Section 1.2 the optimization of the system was completed by another team member working on this research.

The performance of a linear permanent magnet array, when used as an actuator with respect to regenerative capacity and damping force is highly dependent on the geometry of the system. In a limited number of applications, the geometric results yielded through optimization cannot be directly applied to a design due to the availability of components such as permanent magnets. In addition, due to physical constraints with respect to integration with existing products and designs, direct optimization results cannot be used. Therefore it is ideal to limit the scope of the optimization to the geometric constraints. As found in other literature, the goal of a new damper design should be to develop drop in replacement for an original component with the added benefit of increased performance and a return on investment.

Based on the work done by Wang et al. [37] one of the parameters of interest for optimization of an actuator is the ratio of the magnet thickness to the thickness of the iron pole. Figure 4.10 reflects the results obtained through optimization for this ratio.

In Figure 4.10 the horizontal axis reflects the ratio of the magnet thickness to the thickness of the iron pole (τ_m/τ_i), the vertical axis is the normalized damping force and each of the curves reflects a different length for each stack of magnets and iron poles ($\tau = \tau_m + \tau_i$). It can be seen from Figure 4.10 that at approximately a ratio of 2.3 all curves become linear, which illustrates that the minimum required ratio to maximize the normalized damping force is 2.3. This resulting ratio is consistent with the results published by Wang et al. [37] after converting the ratio shown above into an equivalent ratio for comparison. Wang et al. [37] also showed that although the normalized damping force is maximized at this ratio, an equivalent ratio between 2.3 and 3.1 will reduce the effects of force ripple on the actuator. Based on this result a ratio of 3 for τ_m/τ_i and a stack length of $25.4\,mm$ was chosen for the design and modeling.

From this optimization, the constraints of using off-the-shelf components, and the geometric constraints from the mechanical design, the remaining dimensions were chosen. Starting the magnets, a nickle plated neodymium permanent magnet grade N42 was chosen for this design. Although N42 is not the strongest grade of commercially available permanent magnets (N52 is highest), it was selected due to its availability. Once again, based on the availability of magnets; a thickness of $6.35mm(0.25in)$ was chosen. The thick-

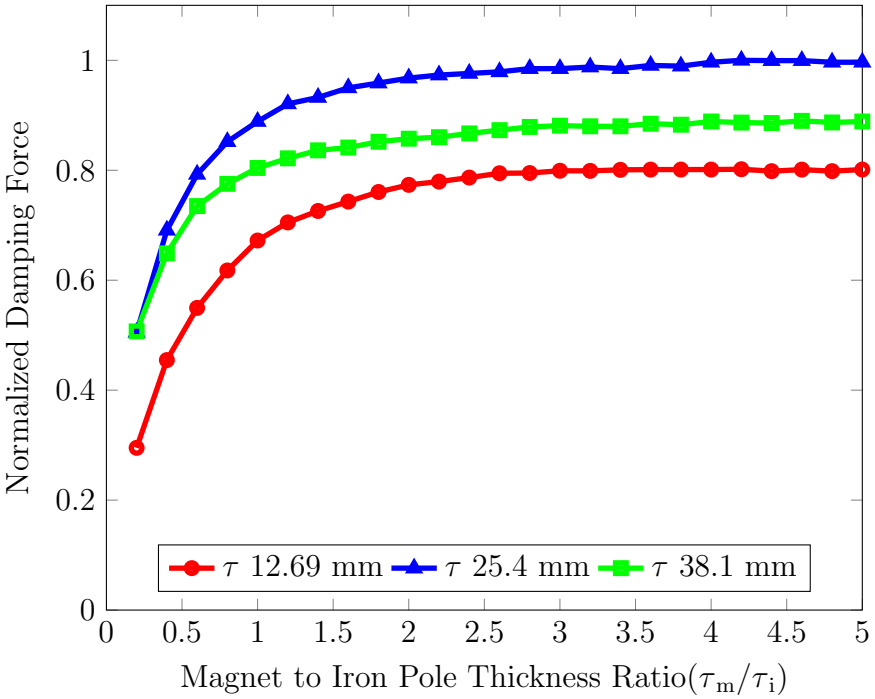

Figure 4.10: Magnet to Iron Pole Thickness Ratio vs. Normalized Damping Force.

ness of the iron pole was selected to be equal to the thickness of the permanent magnets at $6.35\,mm\,(0.25\,in)$. In order to achieve the optimal ratio for τ_m/τ_i, three magnets were used for each iron pole making the total stack length ($\tau = \tau_m + \tau_i$) equal to $25.4\,mm\,(1.00\,in)$. The final component of the electromagnetic system to be defined is the coil. The inner and outer diameters of the coil were restricted to the dimensions from the mechanical design and the purchased parts. Therefore the thickness of the coils (τ_c) became the only variable parameter. The coil thickness was chosen to be $8.47\,mm\,(0.33\,in)$, such that the damper would have three phases. This configuration was chosen based on simulation to mitigate the effects of canceling voltages in the system. Consequently the number of turns for the coils and wire gauge (250 and AWG 28 respectively) were chosen such that the conductor could carry the required current, and to maximize the winding factor.

Finally the total number of coils ($n_c = 15$) was chosen such that the stacks of iron poles and magnets would be within the stack of coils during typical operation. Figure 4.11 is a photograph of the custom coils and coil assembly used for the design.

The final dimensions and parameters for the electromagnetic system are defined in Table 4.2. Now with both the mechanical and electromagnetic systems defined, the final

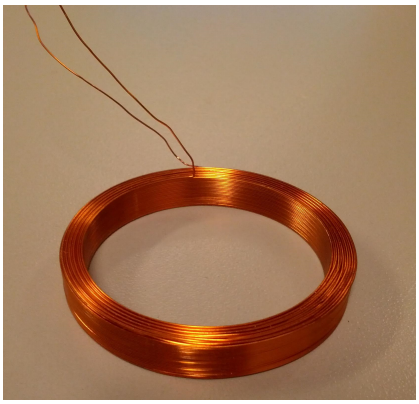

(a) Photograph of Custom Coil.

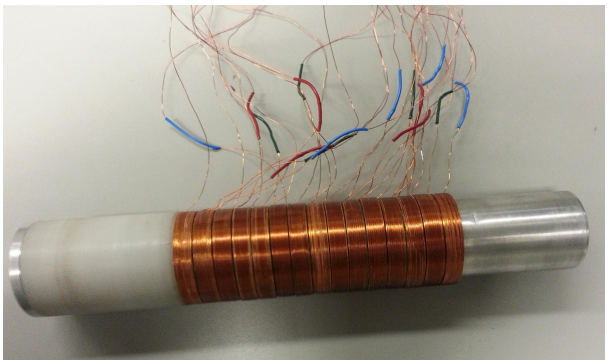

(b) Photograph of Coil Assembly.

Figure 4.11: Hybrid Damper Custom Coils and Assembly.

component of the design is the electronics. The following section will detail the custom electronics in the system.

Variable	Units	Value	Description
r_s	mm[in]	6.350 [0.250]	Radius of Piston Shaft
r_w	mm[in]	19.050 [0.750]	Outside Radius of Magnets/Iron Poles
r_a	mm[in]	20.343 [0.801]	Outside Radius of Air Gap
r_c	mm[in]	24.232 [0.9540]	Outside Radius of Coil
r_p	mm[in]	25.400 [1.000]	Outside Radius of Conductor Tube (Pressure Tube)
τ_m	mm[in]	19.050 [0.750]	Magnet Thickness
τ_i	mm[in]	6.350 [0.250]	Iron Pole Thickness
τ_c	mm[in]	8.467 [0.333]	Coil Thickness
N	N/A	250	Number of Turns in Multi-Turn Coil
a	N/A	25	Number of wire layers in axial direction
b	N/A	10	Number of wire layers in radial direction
W_g	AWG	28	Wire gauge
n_c	N/A	15	Number of coils in design
B_r	T	1.2	Remanent Flux Density of Magnet
M_g	N/A	N42	Magnet Grade (NEODYMIUM, NdFeB)
n	N/A	3	Number of iron pole/magnet stacks

Table 4.2: Electromagnetic Dimensions and Parameters of Interest from Optimization.

4.3 Electronics Design

The objective of the electronics design for this prototype was to develop a system to collect data from the prototype and harvest the power being produced by the damper. In order to achieve this two boards were developed: the *Rectifier Board* and *Buck Booster Board*.

Starting with the *Rectifier Board*; it was designed to act as the main interface between the data acquisition system, external sensors, damper, and *Buck Booster Board*. The data acquisition system used was the National Instruments NI USB-6210 with 16 input channels capable of sampling at 250 kS/s (kilo samples per second). This data acquisition system was directly connected to the left hand side of this board through a set of terminal blocks as seen in Figure 4.12a. The purpose of this data acquisition card was to collect analogue data from the various sensors and coils. The external sensors connected to this board were as follows: string potentiometer, accelerometer, pressure sensor, and load cell. Each of these sensors output analogue data and required a DC power supply. By adding a DC power supply, a power jack barrel, and voltage regulators, each sensor received the correct voltage for operation from a signal source. The sensors physically interfaced to the board

with multi-pin male and female connectors to supply power and output their respective signals. Once the signals were on the board they were routed to the appropriate pins on the data acquisition system for measurement. The sensor input connectors can be seen in Figure 4.12a (side with DB9 connector).

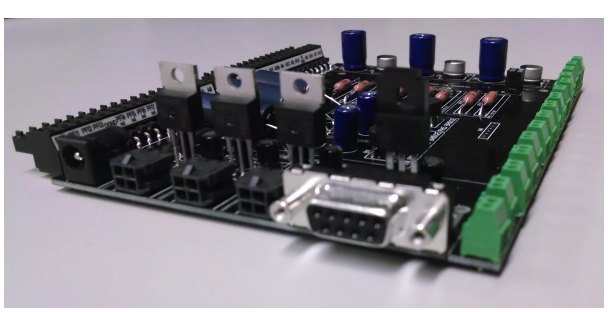

(a) Photograph of Custom Rectifier Board Isometric View.

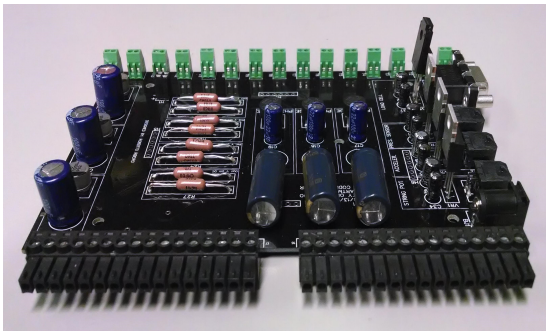

(b) Photograph of Custom Rectifier Board Front View.

Figure 4.12: Hybrid Damper Custom Rectifier Board.

From the damper coils this board received 15 independent AC signals into the green terminal blocks shown in Figure 4.12. These 15 inputs were separated into three predetermined phases consisting of five coils in each phase and summed in series. Following the input of these voltages each phase was redirected into two parallel paths. One path lead to a AC voltage divider and then to the data acquisition system for measurement. The AC voltage divider was added prior to the measurement at the data acquisition system in the event that the sum of the voltages in a phase exceeded the input range for measurement ($\pm 10\,V$). The AC voltage dividers for each phase can be seen in Figure 4.12b on the right hand side. The alternate path after input was to the AC/DC full bridge rectifier with filtering capacitors on the output. Once all three phases were DC voltages they once again took two parallel paths. As done with AC raw inputs, the DC rectified voltages passed through a DC voltage divider and then to the data acquisition card for measurement. The alternative path after rectification was to a common set of header pins where the three DC voltages (one from each phase) were tied together in series. These header pins acted as the output of the *Rectifier Board* and as the DC input into the *Buck Booster Board*.

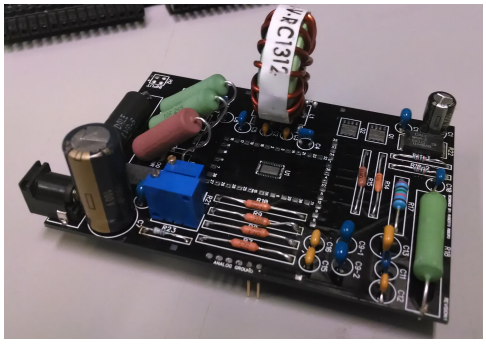

(a) Photograph of Custom Buck Booster Board Isometric View.

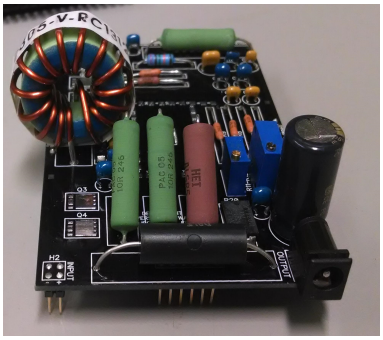

(b) Photograph of Custom Buck Booster Board Front View.

Figure 4.13: Hybrid Damper Custom Buck Booster Board.

The *Buck Booster Board* addressed the second functional objective of the electronics design; energy harvesting. As mentioned in Section 1.2, the circuit design for this board was completed by another team member working on this research. This board was designed to be able to take a wide range of DC input voltages and output a constant DC voltage. This objective was achieved with a 4 switch buck-boost DC/DC controller developed by Linear Technology. The specific controller used for this board was the LT8705 and the developed circuit was derived based on the *12 V Output Converter Circuit* provided in the product literature. Figure 4.13 is a photograph of the final *Buck Booster Board* assembly.

By bringing together the *Rectifier Board* and *Buck Booster Board*, the electronics component of this design is complete and all requirements have been met. Figure 4.14 is a photograph of the final electronics assembly. Based on the described hybrid damper design in this chapter, the following chapter will outline the experimental characterization of this prototype.

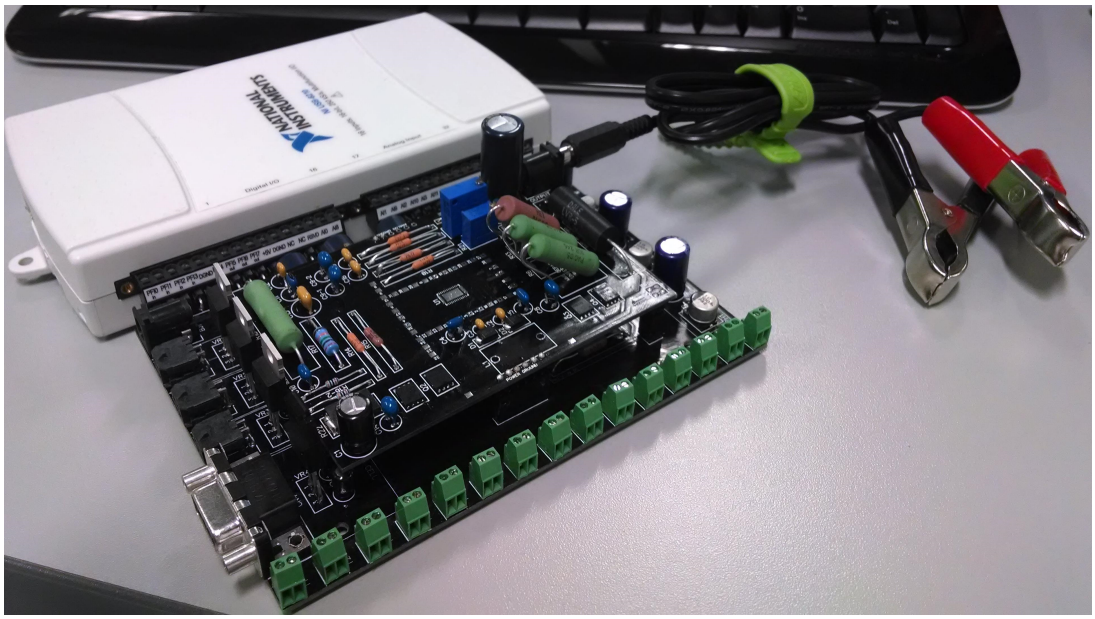

Figure 4.14: Hybrid Damper Custom Electronics Assembly.

Chapter 5

Experimental Validation

Based on the previously defined modeling techniques and the detailed hybrid damper design, the experimental characterization can be completed. The objective of the experimental characterization is to validate the analytical electromagnetic modeling, the finite element model, and to determine the damper's performance characteristics. The following subsections will detail the various experimental protocols, and results obtained.

5.1 Experimental Flux Characterization

One of the fundamental aspects of the electromagnetic system is the radial flux produced by the magnet and iron pole stacks. The radial magnetic flux produced by the stacks is of interest due to the output voltage and force produced by the electromagnetic system; being a function of this flux and the velocity of the piston rod. With the radial magnetic flux accurately characterized, analytically evaluating for the induced voltages and produced forces becomes relatively trivial based on the previously provided expressions.

In order to characterize the radial flux experimentally, a hand-held Gaussmeter was used in conjunction with an Epson Selective Compliance Assembly Robot Arm (SCARA) robot.The experiment was configured such that the probe of the hand-held Gaussmeter was attached to the end effector of the SCARA robot and the piston rod assembly was mounted vertically in a stationary position. Figure 5.1 shows photographs of the Epson SCARA Robot and the Gaussmeter probe measuring the radial magnetic flux density of the stack.

(a) Photograph of Epson SCARA Robot used for Radial Flux Measurement.

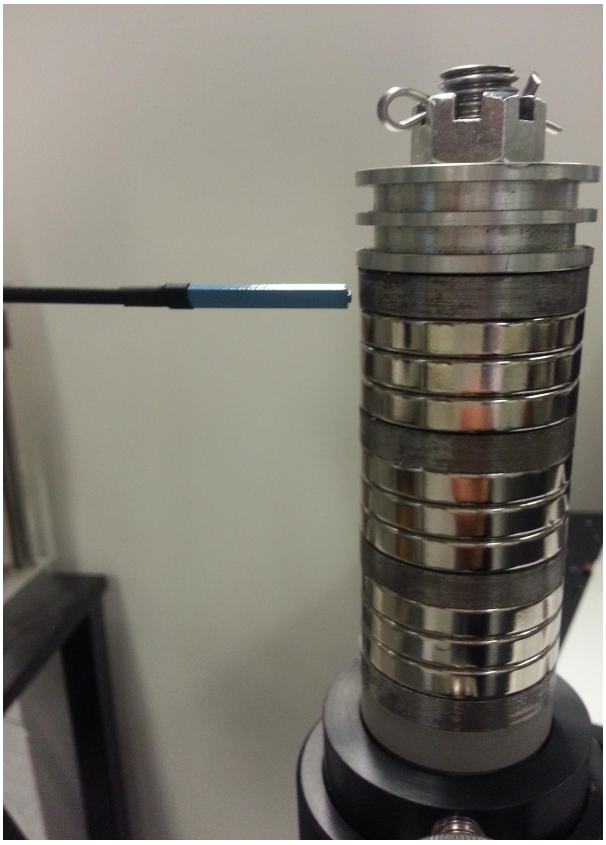

(b) Photograph of Magnetic Flux Measurement Probe and Damper Piston Rod.

Figure 5.1: Radial Magnetic Flux Measurement Setup.

As mentioned in the electromagnetic modeling section, the radial magnetic flux of the stack diverges as function of distance. In order to see this trend experimentally, a variety of offset distances from the surface of the stack were taken as measurement points (refer to Figure 5.2). The offset distances of interest were chosen to be 0.5, 1.5, 3.0, 5.0 mm, which corresponds to approximately the center of the air gap, the interior surface of the coil (r_a), the middle of the coil, and the exterior surface of the coil (r_c).

Based on the defined radial magnetic flux measurement protocol, Figure 5.3 reflects the results obtained from this experiment.

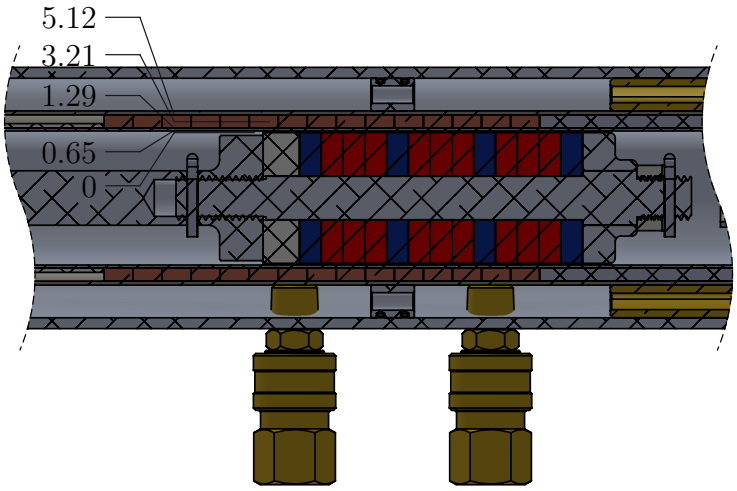

Figure 5.2: Various Offset Distances for Flux Measurement.

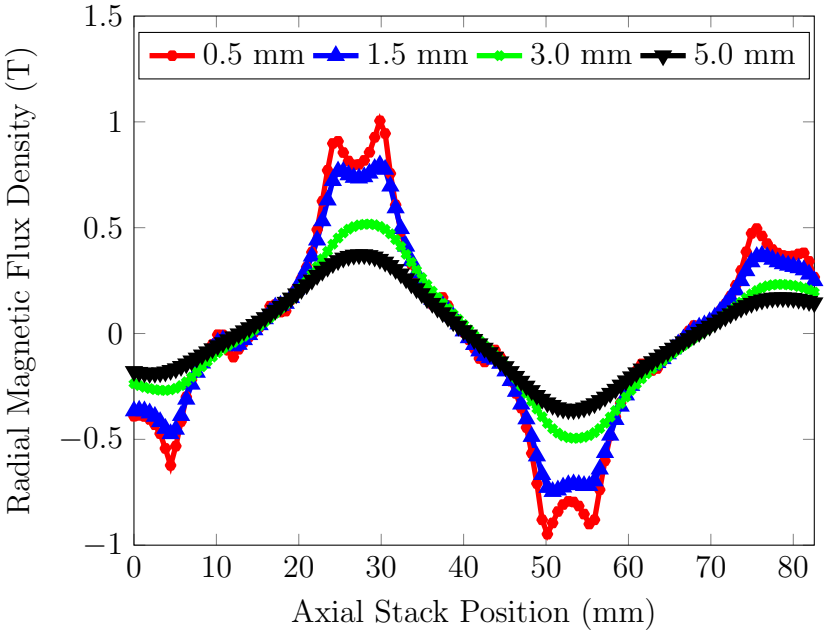

Figure 5.3: Radial Magnetic Flux Density Experimental Measurement at Various Offset Distances.

From Figure 5.3 it can be seen that previously mentioned tend of radial magnetic flux diverging as a function of distance is present in the experimental data. In this figure the *Axial Stack Position* of zero corresponds to the top of the first iron pole shown in Figure 5.2 (first pole after spacer). From the experimental data, it can be seen that the maximum radial flux occurs at the tips of iron poles 2 and 3 (where iron pole 1 corresponds to the pole next to the spacer) for the line representing the $0.5\,mm$ offset. These peaks are attributed to the high concentration of magnetic flux at the tips due to the reduced area (similar to stress concentration factors in stress analysis). To reduce these peaks, a larger fillet could be added on the edge of the iron pole. By referring to Figure 5.4, the flux concentration points at the tips of the poles can be seen.

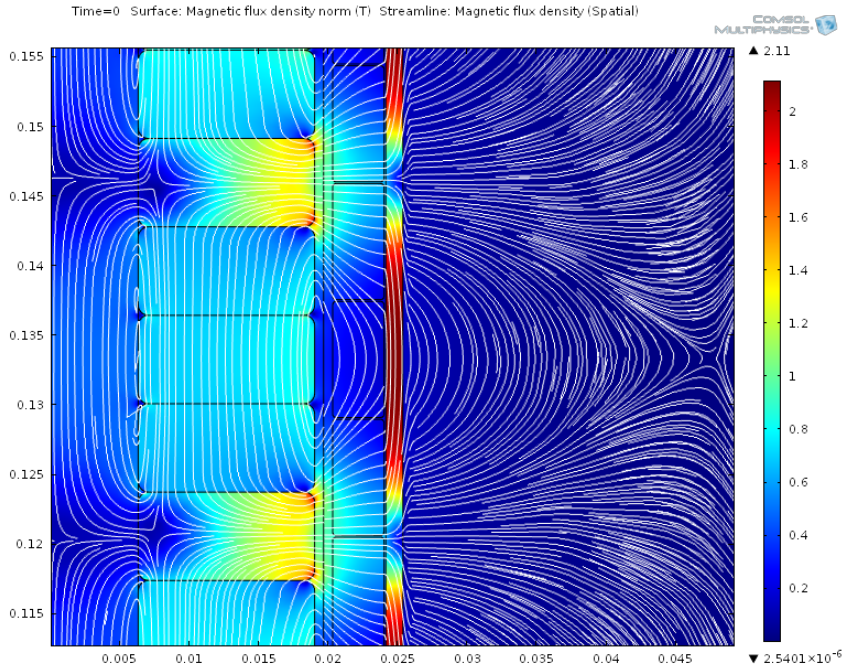

Figure 5.4: Magnetic Flux Density Distribution from Finite Element Analysis.

In addition, from Figure 5.3 it can be seen that the effects of this flux concentration become less dominant as the offset distance increases.

To further evaluate the validity of the finite element model, the measured magnetic flux can be compared with the simulation results. Within the finite element model it is possible to evaluate the magnetic flux at any point in space, which is not the case in reality. Therefore for comparison purposes, a cut line was added to the finite element

model corresponding to a 0.5 mm offset distance with the length of the stack to evaluate the radial flux. Figure 5.5 reflects the results of radial magnetic flux at a 0.5 mm offset distance for both experimental and simulation.

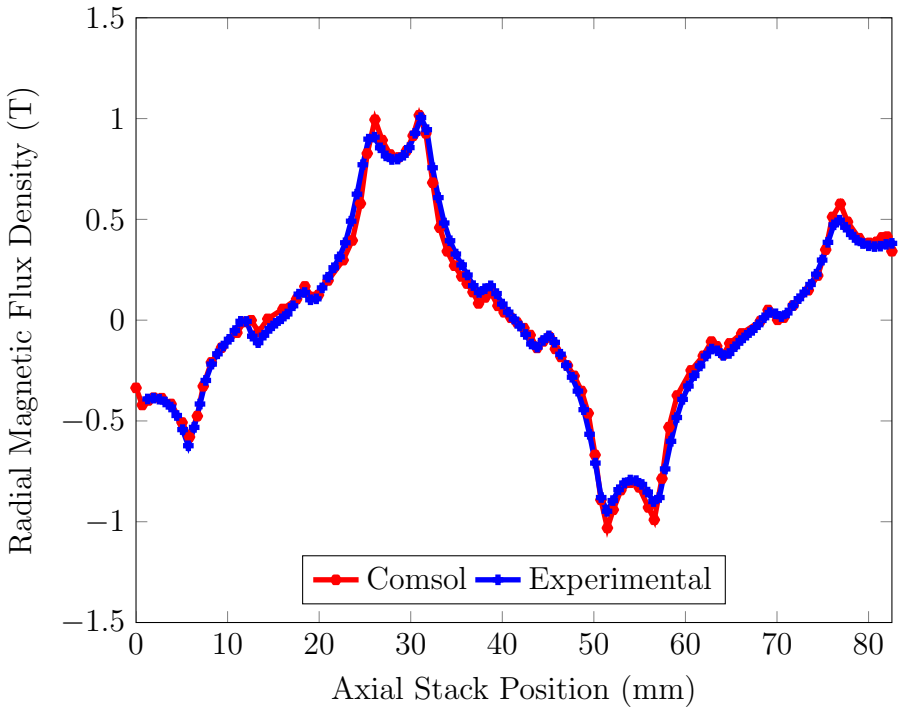

Figure 5.5: Experimental vs. Finite Element Radial Magnetic Flux Density (0.5 mm Surface Offset).

From Figure 5.5 it can be seen that both the experimental and finite element results corresponded well with one another. Although the level of agreement is high, some of the peaks at the previously described flux concentration points disagree slightly between experimental and finite element. This variation can be attributed to an inconsistency in fillet size from manufacturing. In addition, both the experimental and finite element results show ripples that can be seen before and after the peaks. These ripples are attributed to the use of multiple magnets as oppose to a single magnet. Overall it can be concluded that, in terms of radial magnetic flux the finite element model is valid.

In addition to the comparison between experimental and finite element, a comparison between the previously defined analytical model and finite element can be made.

By adding cut lines through the previously mentioned coil, air gap, stator, and magnet/iron pole regions, the radial and axial magnetic flux can be evaluated. Figure 5.6 illustrates the comparison between the analytical and finite element results for the radial magnetic flux through the coil and air gap respectively.

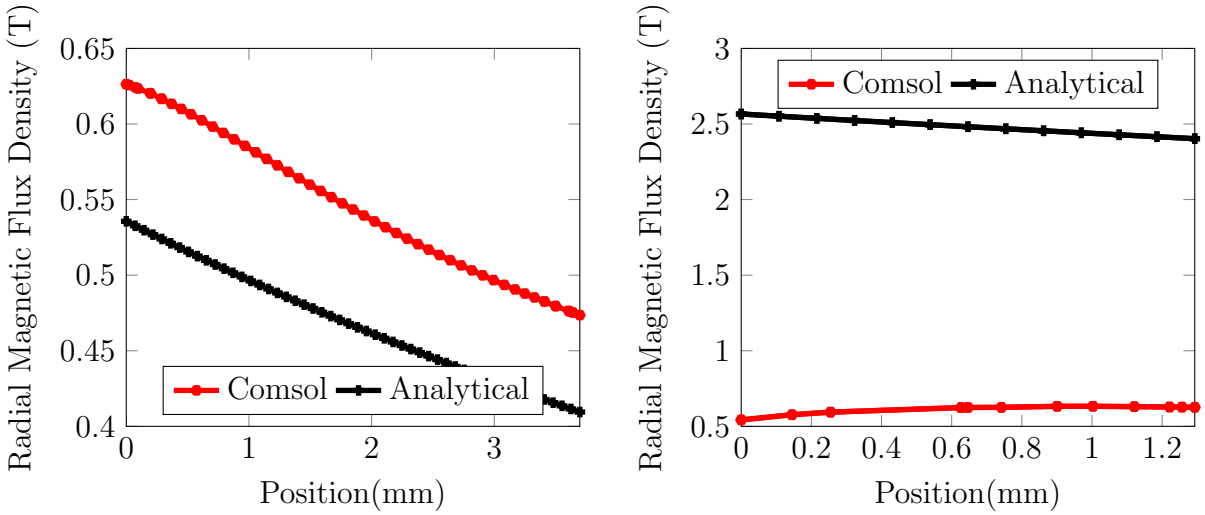

(a) Radial Magnetic Flux Density of Coil (B_C) (Analytical vs. Comsol Simulation).

(b) Radial Magnetic Flux Density of Air Gap (B_{AG}) (Analytical vs. Comsol Simulation).

Figure 5.6: Analytical vs. Simulation Radial Flux Comparison from Magnetic Circuit.

From Figure 5.6a it can be seen that the analytical model and finite element models have agreement with respect to the overall trends, but the discrete values disagree. Although the values disagree, the shown trend validates the modeling approach of assuming the radial magnetic flux divergence can be modeled linearly within the limits of the coil. Figure 5.6b once again shows that the trend between the two lines is similar (more or less constant), although the absolute difference is significantly greater.

Figure 5.7 reflects the comparison between the analytical and finite element axial flux components. From Figure 5.7a it can be seen that the analytical model significantly overestimates the magnitude of the axial magnetic flux. It also shows that assuming the flux is constant through the stator for the magnetic circuit is an inadequate modeling approach. In Figure 5.7b it can be seen once again that assuming constant axial flux through the magnet/ iron pole stack (as shown in the magnetic circuit) is inaccurate; although the difference between analytical and finite element is significantly less when compared to the stator results.

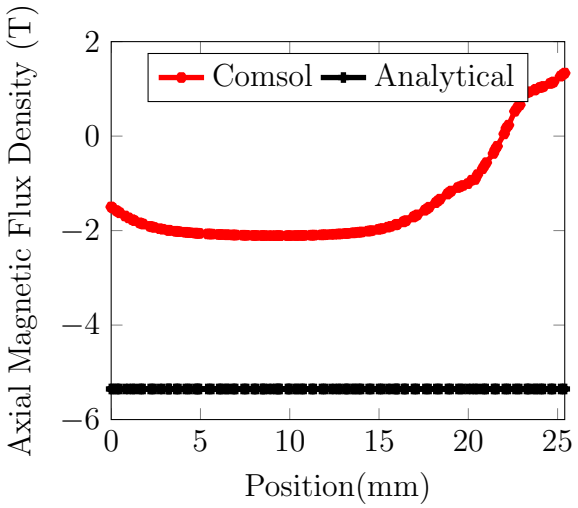

(a) Axial Magnetic Flux Density of Stator (B_S) (Analytical vs. Comsol Simulation).

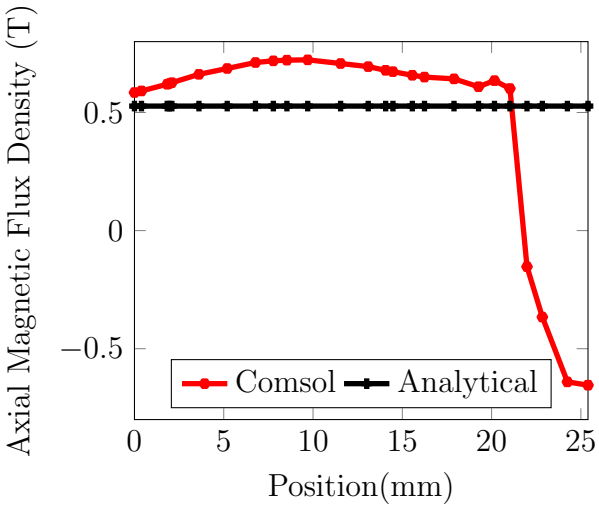

(b) Axial Magnetic Flux Density of Magnet and Iron Pole (B_M) (Analytical vs. Comsol Simulation).

Figure 5.7: Analytical vs. Simulation Axial Flux Comparison from Magnetic Circuit.

Based on the shown results, the analytical model lacks the required level of complexity to accurately model the axial and radial magnetic flux through the various components in the magnetic circuit. As a general model for approximating the flux distributions it maybe sufficient; but if a high level of accuracy is required a different approach should be taken. Now with the magnetic flux characterized, the damper's performance characteristics can be evaluated.

5.2 Experimental Protocol and Equipment

As a means of evaluating the performance characteristics of the hybrid damper, an electromagnetic shaker was used as the input mechanism (LMS 722 shaker). This shaker was driven by an amplifier which received a controlled signal from a function generator (Agilent 33220A). All of the outputs from the damper were then routed to the previously described *Rectifier Board*, and subsequently to two separate data acquisition cards. The first data acquisition card was the previously mentioned National Instruments NI-USB 6210, which was predominately responsible for receiving the outputs from the various sensors. The sensors used in this setup were as follows:

Sensor Type	Model	Range	Measurement
String Potentiometer	Celesco SP2-25	$0 - 635\,mm$	Displacement
Accelerometer	Kistler 8305B10M2	$\pm\,10\,g$	Shaker Acceleration
Pressure Sensor	Honeywell 19C300PG4K	$0 - 300\,psi$	Internal Damper Pressure
Load Cell	Futek LCF450	$0 - 2000\,lbs$	Force

Table 5.1: Sensors used as part of Experimental Protocol.

The second data acquisition card was a National Instruments NI-USB 6225, which was used to record the output from the various coils. All of the data was collected using LabVIEW 2013 and was post processed using MatLab 2012b. Figure 5.8 represents a schematic of the described experimental setup.

The experimental protocol consisted of testing the damper at a variety of frequencies and amplitudes with a sinusoidal profile. Table 5.2 reflects a select list of the tested frequencies and amplitudes which will be included in subsequent sections:

Test Case	Frequency (Hz)	Peak to Peak Amplitude(mm)
1	5	14.40
2	10	8.09
3	15	5.64

Table 5.2: Experimental Protocol Frequencies and Amplitudes.

From the table above, the minimum frequency was set by the lower limit of the LMS 772 shaker itself ($5\,Hz$). The displacement amplitudes were once again limited by the operating range of the shaker and values were selected such that the peak-to-peak amplitudes would be maximized.

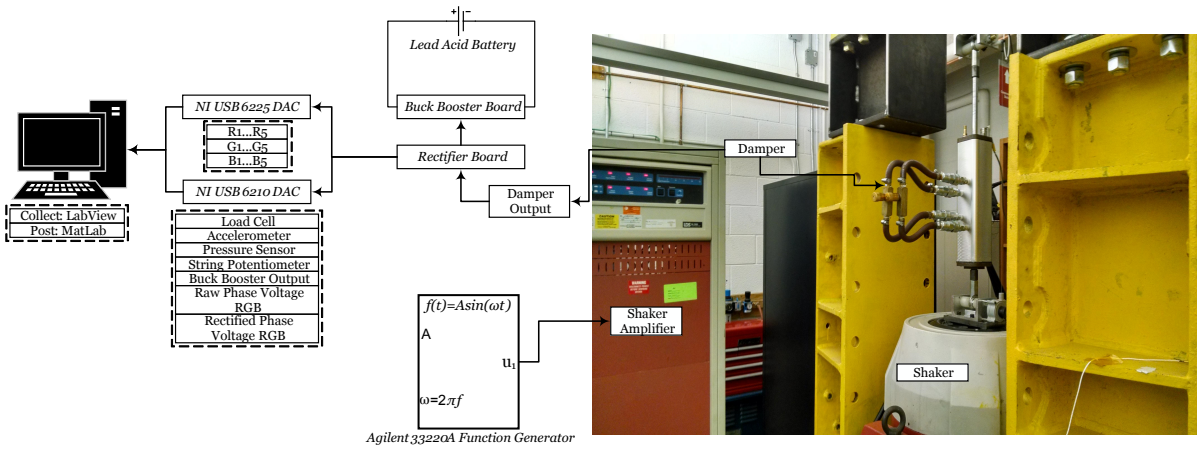

Figure 5.8: Performance Characterization Experimental Setup.

Based on the described experimental protocol and setup, a variety of experiments were carried out to determine the force and regenerative power capacity of the damper. The subsequent sections will further detail the results for the force and power respectively.

5.3 Friction Characterization

As previously mentioned, one major component of the characterization of the hybrid damper is the force it is capable of producing. The force in this system has three components: 1) **Friction** Force, 2) **Electromagnetic** Force, and 3) **Hydraulic** force. The friction force in the system is attributed to the seals which interface with the piston rod assembly. This force is always present and if not accounted for independently it will skew other force results. With the friction characterization done independently, it can simply be subtracted from the other measured forces to get individual components of force.

From the previously described experimental protocol friction was characterized based on the three defined test cases (1-3). In addition, since the travel of the damper ($83.820mm(3.30in)$ from Table 4.1) significantly exceeds the maximum experimental excitation amplitude ($14.4\,mm\,(0.567\,in)$), three additional test points were taken. These additional test points are illustrated in Figure 5.9.

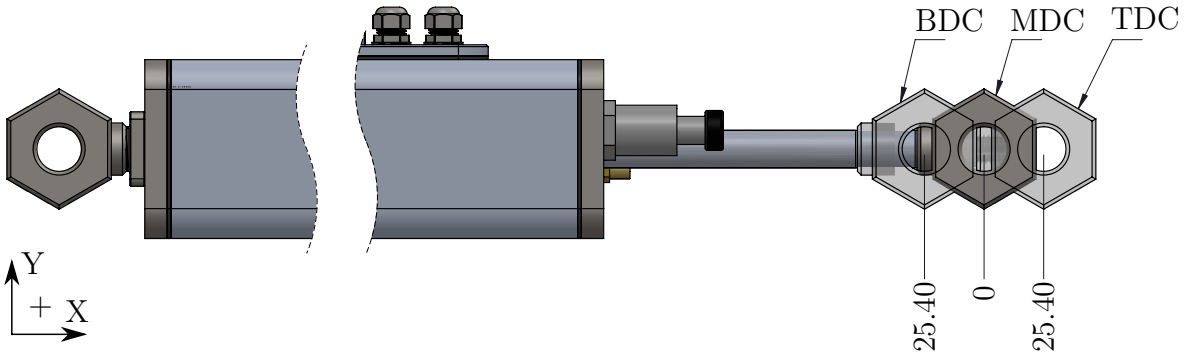

Figure 5.9: Supplemental Test Points for Friction Characterization.

From Figure 5.9, the *MDC* position corresponds to when the stack of permanent magnets and iron poles is centered in the stack of coils. The *BDC* and *TDC* positions correspond to a shift from the *MDC* position in the negative and positive X directions respectively of $25.4\,mm\,(1.00\,in)$.

Starting with the *BDC* test point; Figure 5.10 illustrates the *Force vs. Displacement* and *Force vs. Velocity* results obtained at the various frequencies and amplitudes.

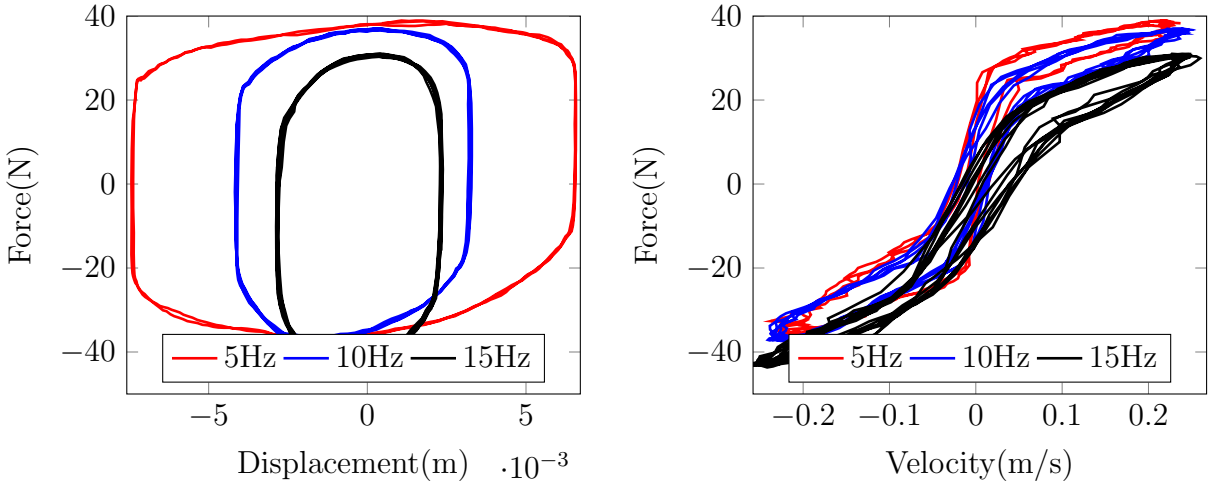

(a) Force vs. Displacement (BDC).

(b) Force vs. Velocity (BDC).

Figure 5.10: Experimental Friction Characterization at BCD Test Point.

From Figure 5.10a, it can be seen that the maximum force occurs at a frequency of 5 Hz and that all three frequencies have produced a similar trend. The theoretical shape of this figure should be a prefect square or rectangle by assuming the friction force is solely attributed to Coulomb friction. The major variation seen in this figure is the skew of the profile. This skew is caused by trapped air within the damper acting as an air spring, adding a stiffness term to the Coulomb friction. If a linear regression was done to this data set and the effects of stiffness were subtracted, the skew would no longer be present. In Figure 5.10b it can be seen that the three frequencies maintain a tight distribution for the force versus velocity relationship. Removing the effects of the air stiffness in this figure would result in the shown profile collapsing into three lines. The slopes of the lines above and below the zero point in this figure typically have a slope of zero, in the case of solely Coulomb friction. Since these lines have a non-zero slope, this is indicative of viscous damping (this is also illustrated in the force vs. displacement figure by the curved segment between the two vertical portions of the profile).

By assessing the two remaining test points (*MDC* and *TDC*, Figures 5.11 and 5.12). it can be seen that similar trends and magnitudes are present (at all of the test points). Since *MDC* corresponds to the initial position designed for; in subsequent sections only data at the *MDC* position will be present. Now with the contribution of friction for the system identified, the electromagnetic contribution can be defined.

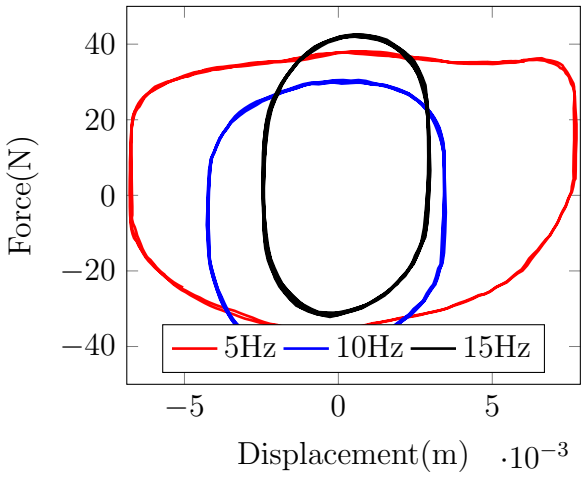

(a) Force vs. Displacement (MDC).

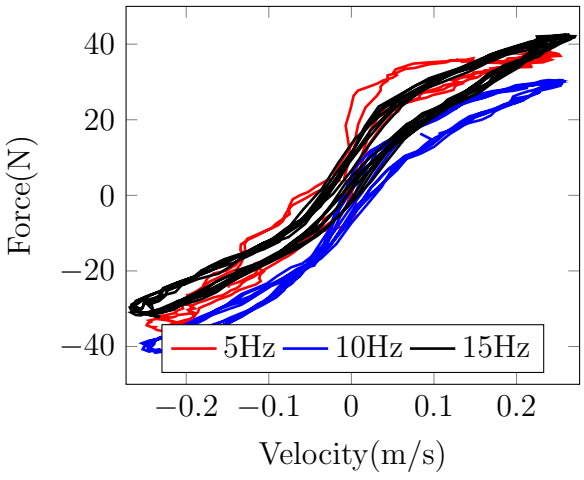

(b) Force vs. Velocity (MDC).

Figure 5.11: Experimental Friction Characterization at MCD Test Point.

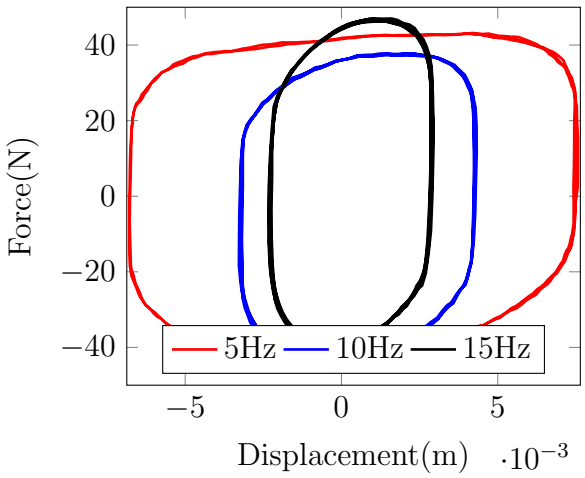

(a) Force vs. Displacement (TDC).

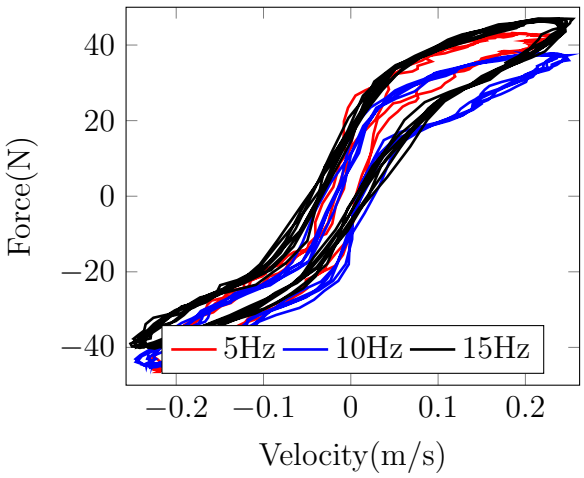

(b) Force vs. Velocity (TDC).

Figure 5.12: Experimental Friction Characterization at TCD Test Point.

5.4 Electromagnetic Characterization

The electromagnetic system is a fundamental part of this damper due to it being the mechanism for variable damping, as well as for regenerative power. The electromagnetic system can be further characterized by assessing the three distinct components of the output; these being the induced voltage, force, and regenerative power capacity. The following subsections of this chapter will assess each of these components.

5.4.1 Electromagnetic Induced Voltage Characterization

As mentioned previously, the electromagnetic system has been configured to have 15 independent coils which are sub-divided into three discrete phases. The adopted naming convention for these phases was derived based on the RGB color model; where the first phase consists of coils $R1 - R5$, the second phase consists of coils of $G1 - G5$, and the final phase consists of coils $B1 - B5$. Figure 5.13 illustrates the positions of the various coils within the electromagnetic system.

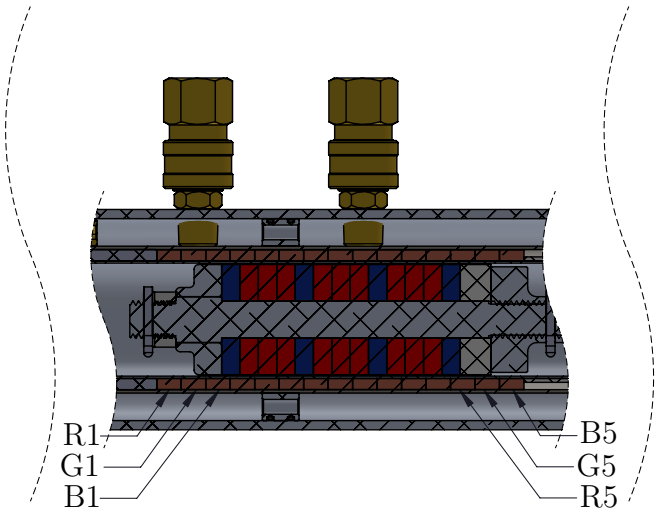

Figure 5.13: Coil Naming Convention.

To better understand the output of the various coils, Figures 5.14, 5.15a, and 5.15b represent a sample output of the open-loop voltage for all of the coils at a frequency of $5\,Hz$.

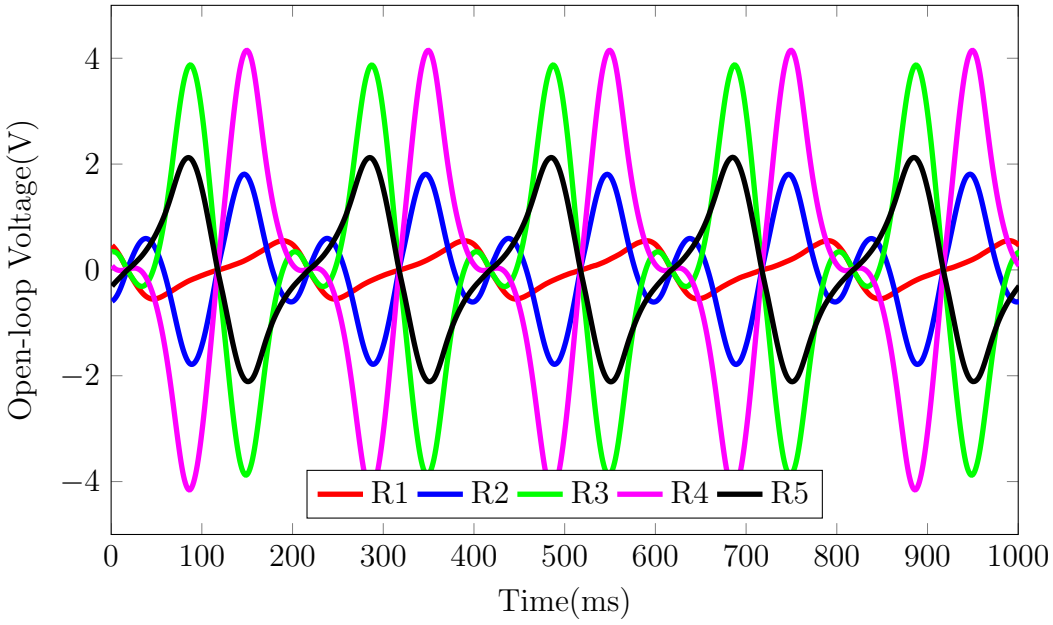

Figure 5.14: Experimental Red Phase Open-loop Voltage vs. Time at MDC 5Hz.

Starting with Figure 5.14, it can be seen that all of the coils follow a periodic trend and that there are two sets of coils that are in phase with the same sign ($R2$ & $R4$ are pairs and $R3$ & $R5$ are pairs). By referring to Figure 5.15a, it can be seen that once again a periodic trend is present but the number of coil pairs in this phase has dropped to one ($G1$ & $G3$ are pairs). Coils $G2$ & $G4$ are similar with respect to sign but it is clear that a phase shift is present. Finally by referring to Figure 5.15b, this phase has identical coil pairs to the red phase ($B2$ & $B4$ are pairs and $B3$ & $B5$ are pairs respectively) and overall this is the best performing phase (highest voltage output). In addition, it can be seen across all three of these figures that each phase has a coil which is out of phase and marginally contributing to the overall induced voltage ($R1$, $G5$, & $B5$, respectively). This is due to these coils not being directly excited by the movement of the magnet/iron stack.

In general, the trends seen and described in the previously shown plots are highly dependent on the amplitude of excitation and the geometry of the electromagnetic system. If the initial starting position for the stack was shifted up or down by the thickness of a coil (τ_c), the previously shown trends would all still be present, but in different phases (i.e Red phase would become best performer and blue would become worst). Now with an understanding of the open-loop experimental voltages, the electromagnetic force and power can be further characterized.

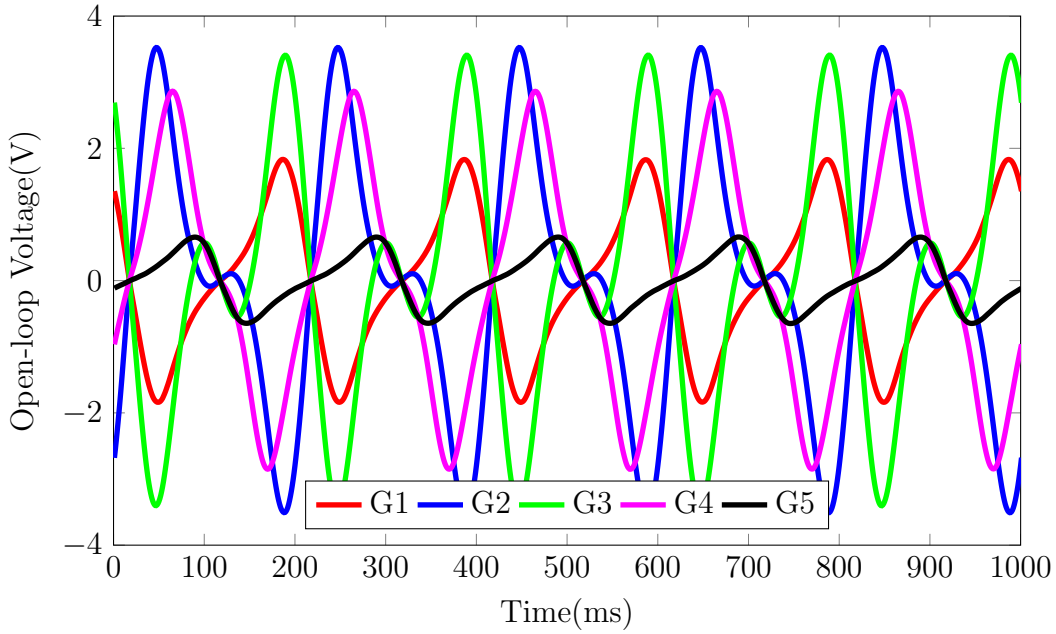

(a) Experimental Green Phase Open-loop Voltage vs. Time.

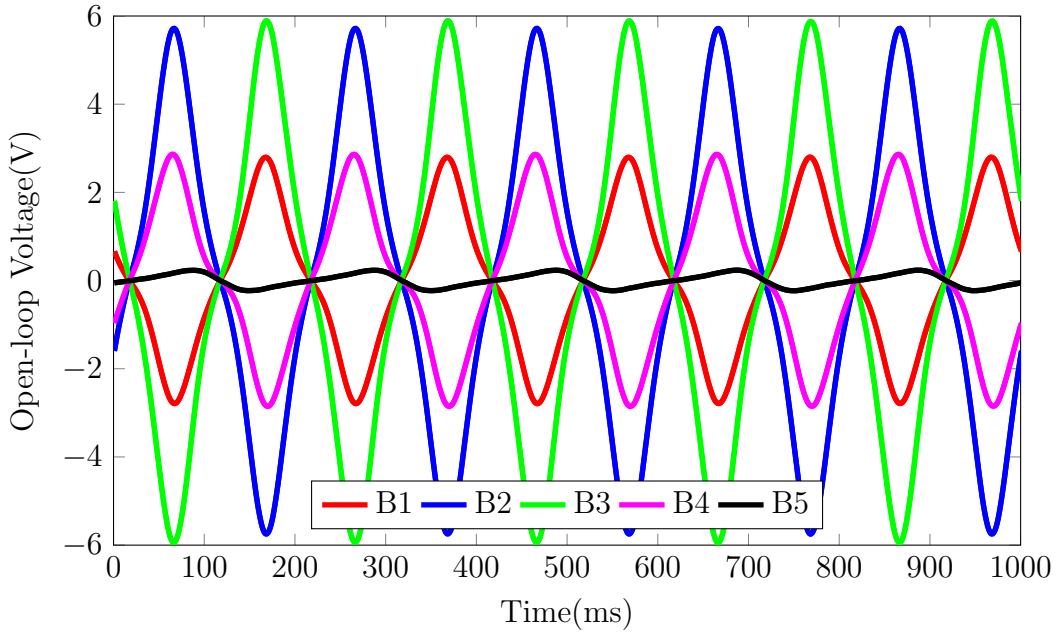

(b) Experimental Blue Phase Open-loop Voltage vs. Time.

Figure 5.15: Green and Red Phase Open-Loop Voltages at MDC 5Hz.

5.4.2 Electromagnetic Force

As seen in the modeling section of this thesis; the electromagnetic force is dependent on current and current is dependent on the internal and external resistances of the system (refer to equations (3.29) and (3.51)). By knowing the internal resistance of the system is a fixed parameter (resistance of multi-turn coils), by default current can only be maximized when the external resistance is minimized. Therefore, the condition that will result in the maximum amount of electromagnetic force is when the external resistance of the system is equal to zero. Based on this relationship, the electromagnetic force is characterized when the coils are independently short circuited.

Figure 5.16 reflects the maximum measured experimental electromagnetic force produced by the system at a frequency of 5 Hz.

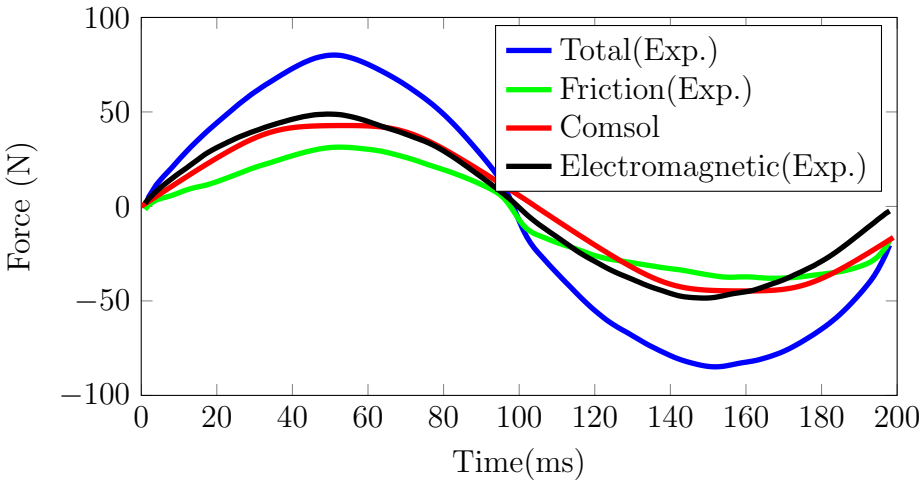

Figure 5.16: Experimental and Simulation Force Comparison (MDC 5Hz).

Directly from the experimental protocol, the total force produced by the system while short circuited can be measured(blue line on figure). As previously mentioned, the friction force is always present and therefore the measured total is equal to the summation of the electromagnetic and friction forces. Since the friction force was characterized independently(green line in figure), through post-processing the electromagnetic force contribution can be determined (black line in figure). To further validate the obtained results, finite element force results were also added for comparison. Based on the shown results, a good agreement between finite element and experimental is present which further validates the completed modeling. By using the same approach described for the $5\,Hz$ experimental data, the $10\,Hz$

and 15 Hz data sets displayed similar results and are presented in Figures 5.17 and 5.18 respectively.

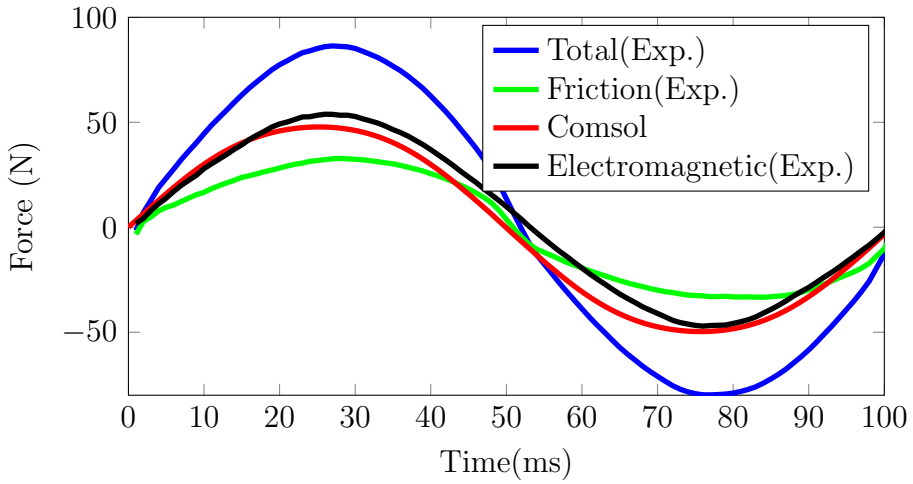

Figure 5.17: Experimental and Simulation Force Comparison (MDC 10Hz).

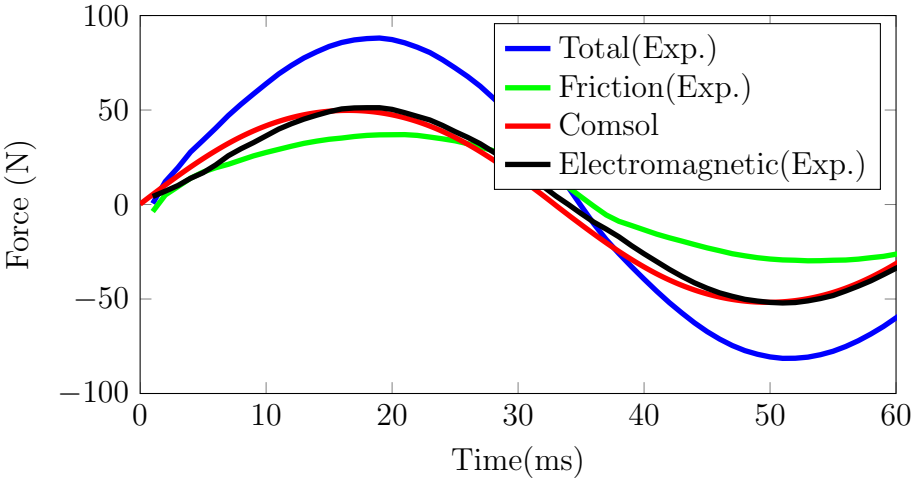

Figure 5.18: Experimental and Simulation Force Comparison (MDC 15Hz).

Since the finite element model had a high level agreement with the three previously shown test cases, additional simulations were run at a variety of frequencies and amplitudes to illustrate the overall trend for force. Figure 5.19 illustrates the yielded results from the

additional simulations (black pentagon markers in this figure are the previously shown experimental results).

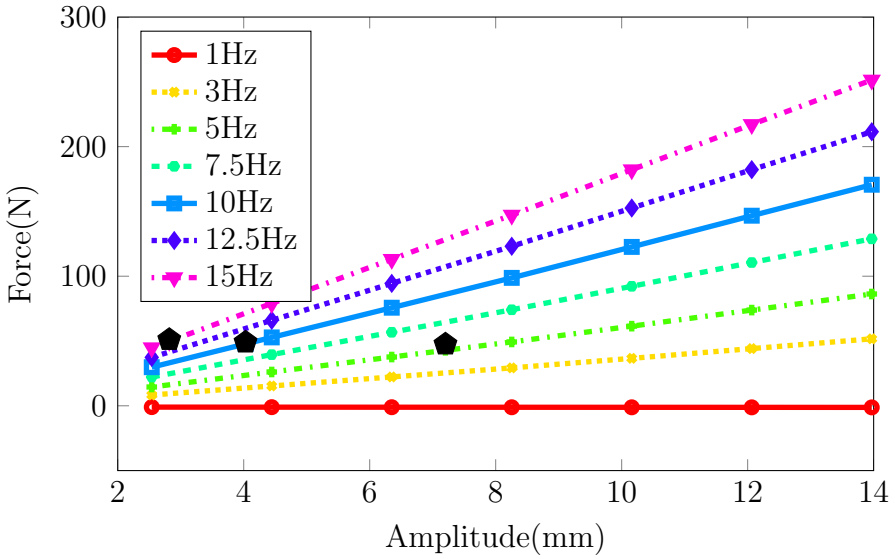

Figure 5.19: Force vs. Displacement Amplitude at Various Frequencies.

From this figure it can be seen that the maximum amount of force is produced at a frequency of 15 Hz and an amplitude of 14 mm (or 28 mm peak-to-peak). It can also be seen that the force for all frequencies increases linearly with amplitude. The shown trend is self-consistent with the previously defined equation for voltage (V_{emf}), which showed that voltage is a function of velocity. With the electromagnetic force defined experimentally and through simulation, the next aspect of the electromagnetic system to be defined is the regenerative capacity.

5.4.3 Regenerative Power

As mentioned in the background section of this thesis, maximum energy recovery occurs when internal resistance is equal to external resistance based on the maximum power transfer theorem (assuming no complex impedance in the system). If complex impedance is present, capacitance or inductance needs to be added to the energy harvesting circuit to remove the phase lead or lag between current and voltage. Knowing that the coils in the system are capable of producing inductance, the magnitude of the inductance needs to be assessed.

To the measure the effects of inductance for the coils a LCR meter (Agilent E4980A) was used. Figure 5.20 illustrates the obtained experimental results from the inductance measurement experiment.

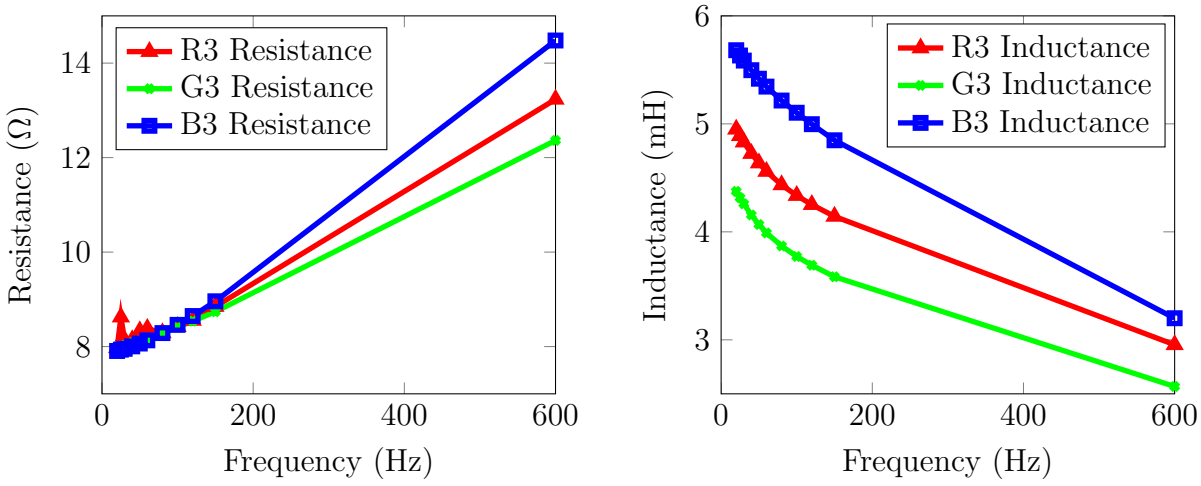

(a) Resistance vs. Frequency Relationship.

(b) Inductance vs. Frequency Relationship.

Figure 5.20: Experimental Complex Impedance of Coils.

Starting with Figure 5.20a, it can be seen that the resistance of the coils increases as the frequency increases. In Figure 5.20b the opposite trend is true; the inductance decreases as the frequency increases. Although it is apparent that inductance is present in the system, since the magnitude is low the induced phase shift between voltage and current would be negligible. Therefore for maximum power transfer the internal and external resistances will be equal.

To experimentally validate the amount of power the electromagnetic system is able to

provide, two configurations were evaluated: *Standard* and *Star*. The *Standard* configuration consists of each coil being connected to an individual resistor equal to the resistance of the coil. The *Star* configuration consists of all phases being connected in star with each branch being a phase. The coils in each phase are configured such that the polarities are changed in one set of the pairs (previously described pairs) to mitigate the canceling effects. Figure 5.21 illustrates a sample of the experimental results for power and force for the *Standard* and *Star* configurations, respectively (for the 10 Hz test case).

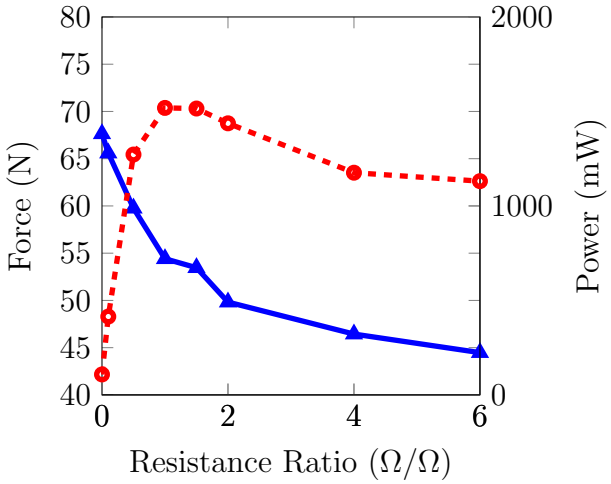

(a) Maximum Power Transfer Standard Configuration (MDC 10Hz).

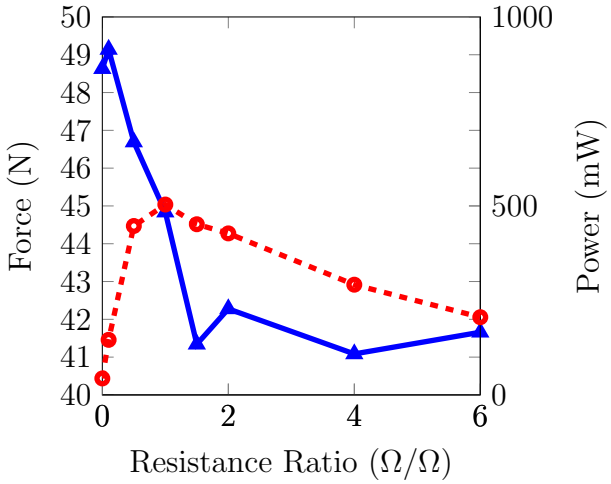

(b) Maximum Power Transfer Star Configuration (MDC 10Hz).

Figure 5.21: Maximum Power for Two Test Configurations (MDC 10Hz).

From Figure 5.21 it can be seen that the maximum power transfer in both configurations occurs when the internal and external resistances are equal (resistance ratio of 1). It can also be seen that the *Standard* configuration produces more power and force. This is attributed to there being no canceling of voltages in this configuration, resulting in a higher output. Once again, to obtain more generalized trends for power a variety of simulations where completed. Figure 5.22 illustrates the relationship between excitation amplitude and power at a variety of frequencies (where the black pentagon is an experimental data point).

From Figure 5.22 it can seen that maximum power occurs at the maximum frequency and amplitude (which is similar to the results shown in Figure 5.19 for force). Another trend that can be seen in this figure is that power increases with parabolic trend as the amplitude increases. Based on the presented results, the electromagnetic system has been

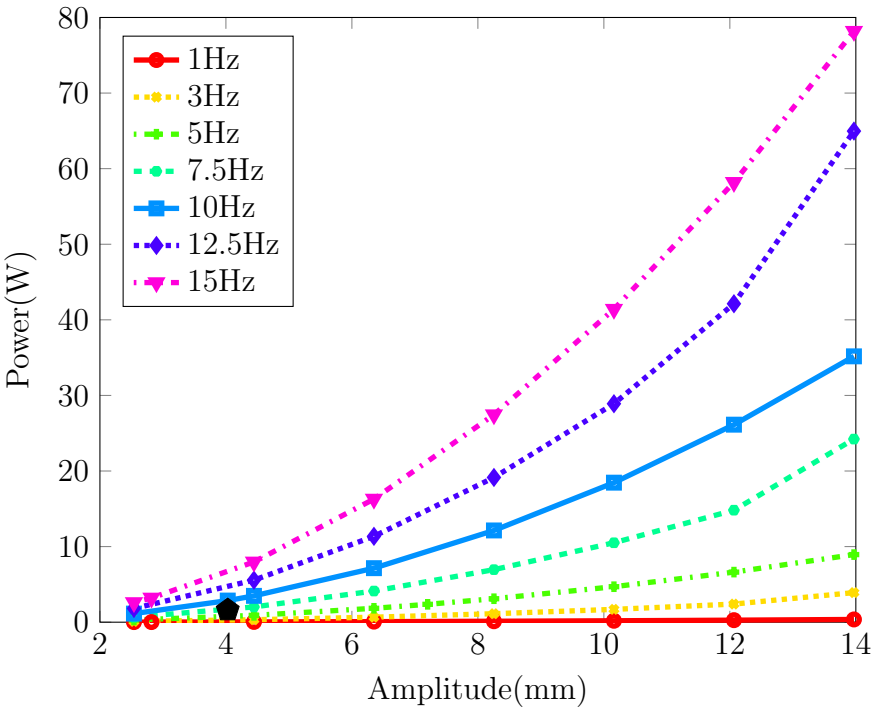

Figure 5.22: Power vs. Displacement Amplitude at Various Frequencies.

fully characterized and high level of agreement between experimental and finite element results has been shown. The following section will detail the last force producing element in the system; the hydraulic system.

5.5 Hydraulic Characterization

The final force producing component of the detailed hybrid design is the hydraulic force. In the hydraulic system, one of the parameters of interest is the value of the pressure of the inert gas in the damper. In most twin tube designs dampers are typically pressurized between $5.5 - 8.3\,bar$ $(80 - 120\,psi)$. To determine the effects of inert gas pressure on the performance of the damper, the experimental protocol was carried out at $10\,Hz$ (average frequency). Figure 5.23 illustrates the results obtained from this experiment.

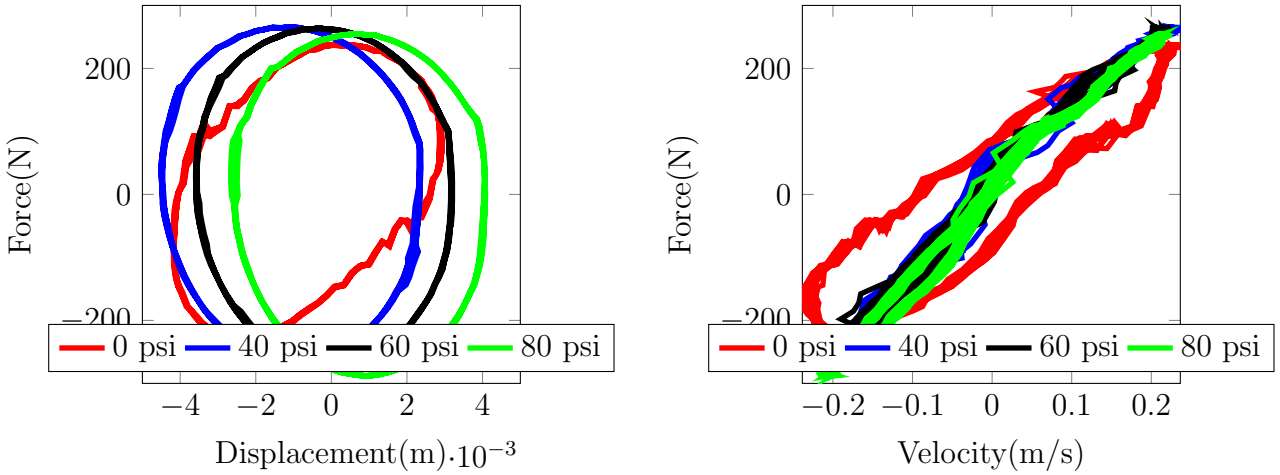

(a) Force vs. Displacement (MDC).

(b) Force vs. Velocity (MDC).

Figure 5.23: Experimental Hydraulic Force Characterization Effects of Inert Gas Pressure.

From 5.23 it can be seen that when there is no inert gas is in the system, stiffness is present; this is indicated by the skew of the force versus displacement plot and also by the force versus velocity profile not being a line. By increasing the pressure between $0 - 80\,psi$, it can be seen that the stiffness is removed from the system and the force displacement profile shifts to the center point of the graph. Based on these results the inert gas pressure was set to $80\,psi$ for the remaining experiments. The subsequent figure reflects the results for force versus displacement and velocity for the hydraulic system at all three test points.

From Figure 5.24a it can be seen that at $5\,Hz$ and $10\,Hz$ frequencies the force displacement profile fits the theoretical model. The vertical segments of the profile are attributed to the friction component of the system and the curved sections are attributed to viscous damping. The $15\,Hz$ profile exhibits a similar trend; although a skew is still present which could be addressed by increasing the pressure of the inert gas beyond $80\,psi$. From 5.24b,

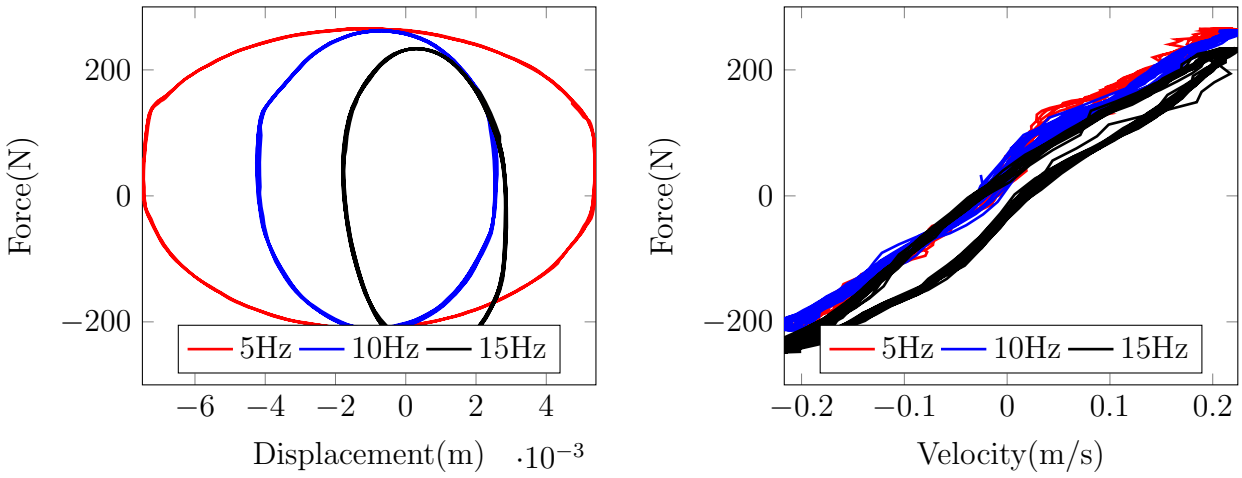

(a) Force vs. Displacement (MDC).

(b) Force vs. Velocity (MDC).

Figure 5.24: Experimental Hydraulic Force Characterization at MCD Test Point.

it can be seen that once again the 5 Hz and 10 Hz profiles fit the theoretical model and 15 Hz is slightly off due to the stiffness in the system. Another observation that can be made is that the effect of viscous damping is significantly more dominant in comparison to the friction force. This dominance leads to the reasonable approximation of modeling the summation of the friction and viscous forces solely as viscous(straight line for force versus velocity profile). Based on this characterization and the previous electromagnetic force, the final section of this chapter will illustrates the complete hybrid force characterization.

5.6 Complete Characterization

The final step in the characterization of the hybrid damper is to bring together the force contributions from the hydraulic and electromagnetic systems. Figure 5.25 illustrates the maximum achievable variation in damping force at the three test points.

From 5.25 it can be seen that all of the results from the experimental test points match that of a theoretical damper within reason. The variation in the experimental results once again can be attributed to the stiffness in the damper. A damper is ultimately characterized by its damping coefficient, which can be obtained from the force versus velocity figures. Since the units of damping in the metric system are Ns/m; by doing a linear regression of the data sets illustrated in Figures 5.25b, 5.25d,and 5.25f the following results were obtained.

Frequency (Hz)	Hydraulic Damping Coefficient (Ns/m)	Electromagnetic Damping Coefficient (Ns/m)	Summation (Ns/m)
5	1285.6	198.5	1484.1
10	1264	204.2	1468.2
15	1258	182.8	1440.8

Table 5.3: Summary of Damping Coefficient Results of Hybrid Damper.

Based on the results of the regression it can be concluded that, the average damping coefficient for the hydraulic system is equal to $1269.2 Ns/m$, and the average damping coefficient for the electromagnetic system is $195.17\, N/s/m$. This results in variable damping between $1269.2 - 1464.37\, Ns/m$. Based on the detailed experimental validation and previous chapters the complete scope of this research has been detailed. The following chapter will outline the major conclusions drawn from this work as well as avenues for future research.

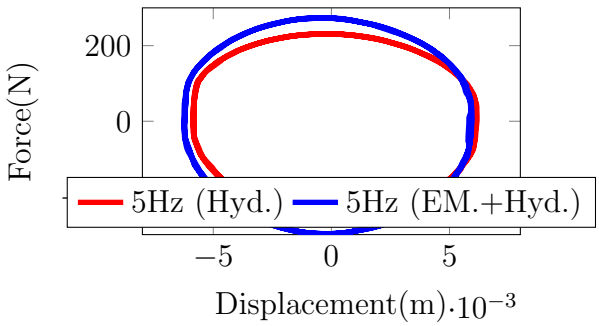

(a) Force vs. Displacement (5Hz MDC).

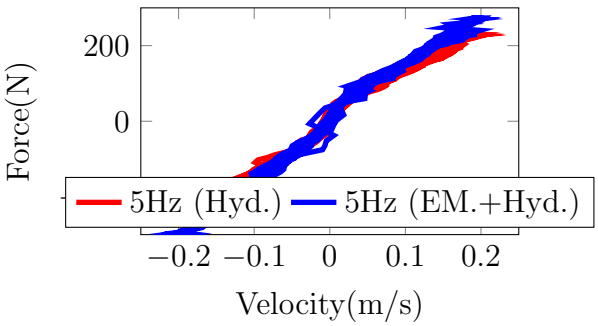

(b) Force vs. Velocity (5Hz MDC).

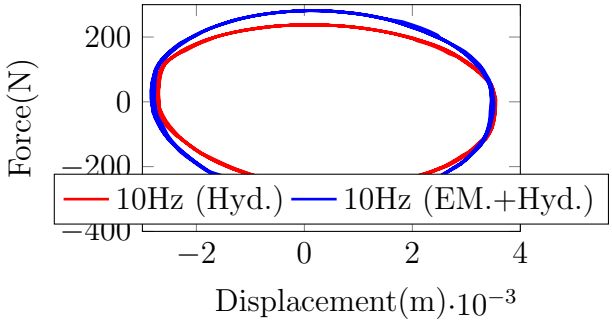

(c) Force vs. Displacement (10Hz MDC).

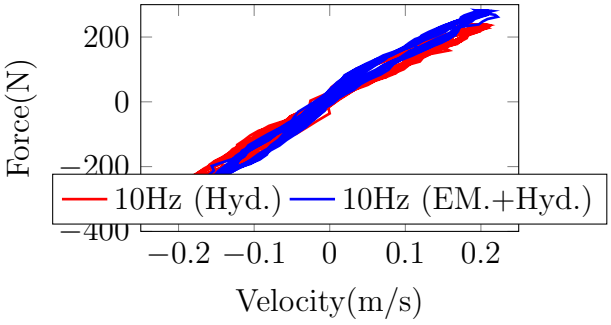

(d) Force vs. Velocity (10Hz MDC).

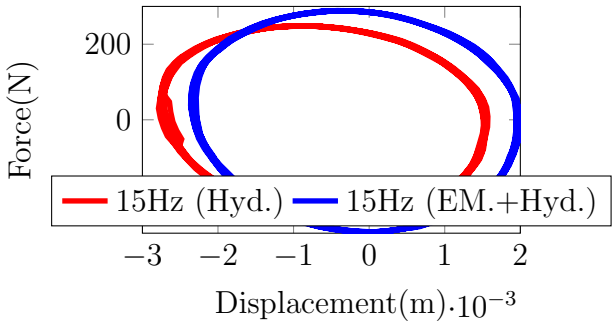

(e) Force vs. Displacement (15Hz MDC).

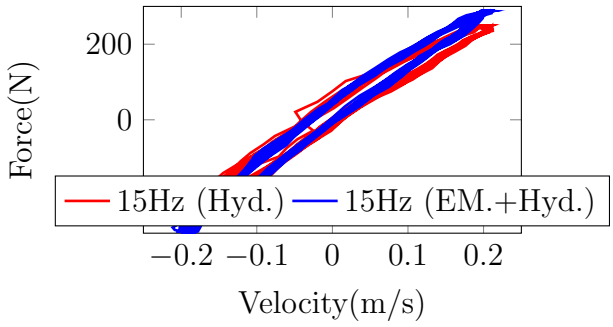

(f) Force vs. Velocity (15Hz MDC).

Figure 5.25: Experimental Hydraulic+Electromagnetic Characterization at MCD Test Points.

Chapter 6

Conclusions and Future Work

Damping in a variety of applications has a varying threshold requirement as a function of excitation in order to achieve a particular system response. This varying requirement is of significance in an automotive suspension system due to the conflicting objectives of comfort versus road holding. To address these conflicting objectives a variety of commercial and non-commercial variable damping solutions have been developed. Although the developed solutions are functional and capable of producing the requisite functionality, their major deficiencies stem from power consumption and critical failure modes (not fail-safe). To address these concerns, a hybrid damper consisting of a viscous bias and electromagnetic system was developed. The developed design was configured such that the viscous medium provided the bias damping force, and the electromagnetic system provided the variability in damping for the steady state condition (bias) to upper threshold.

In order to model this system, a variety of techniques were used to define the dynamics of the suspension system and also the electromagnetic system. The dynamics of the suspension system were modeled based on the quarter car model; and the input excitation into this model was a road profile modeled using the ISO power spectral density method. The electromagnetic system was characterized based on the lumped magnetic circuit model and through finite element modeling.

To characterize this system experimentally, two key attributes needed to be defined: force and regenerative power. In order to characterize the force, a multitude of experiments were carried out to evaluate the individual force components attributing to the total force produced by the system (friction, hydraulic, and electromagnetic). The regenerative capacity of the damper was evaluated based on the two connection permutations: *Standard* and *Star*. Ultimately it was shown that the standard configuration yield better results.

The electromagnetic system, through experimental and simulation results showed a high level of sensitivity to frequency and amplitude based on the chosen geometry. This leads to the conclusion that the electromagnetic system should be designed for the minimum excitation amplitude and frequency. The amount of force produced by the electromagnetic system is linearly proportional to the excitation amplitude, while the power increases with a parabolic trend as a function of amplitude.

Based on the detailed design, supporting modeling, and experimental results, it can be concluded that a variable damping solution has been developed and characterized that addresses the deficiencies associated other designs. As avenues for future research it is recommended that the following is further investigated:

1. Develop an analytical model that better characterizes the non-linearity of the electromagnetic system. Such a model is of interest due to the computational costs associated with the existing finite element model.

2. Develop an analytical model for the force produced by the hydraulic system.

3. Investigate alternative coil configurations to address cable management concerns for existing design.

4. Investigate the required changes to the existing damper design to transition from prototyping to commercialization.

5. Investigate suitable control strategies for the damper and evaluate the performance characteristics.

6. Experimentally characterize damper on a vehicle to better understand its performance characteristics during typical operation.

References

[1] ISO 8608:1995. Mechanical vibration-road surface profiles: Reporting of measured data. *International Organization for Standardization, Geneva, Switzerland, Tech. Rep.*, 1995.

[2] Audi AG. Adaptive air suspension. `http://m.audi-technology-portal.com/en/atp/Chassis/Suspension-control-systems/adaptive-air-suspension/adaptive-air-suspension`.

[3] Audi AG. Audi magnetic ride. `http://m.audi-technology-portal.com/en/atp/Chassis/Suspension-control-systems/Audi-magnetic-ride/Audi-magnetic-ride`.

[4] Audi AG. Dynamic ride control. `http://m.audi-technology-portal.com/en/atp/Chassis/Suspension-control-systems/Dynamic-Ride-Control/Dynamic-Ride-Control`.

[5] A. Bandivadekar, K. Bodek, L. Cheah, C. Evans, T. Groode, J. Heywood, E. Kasseris, M. Kromer, and M. Weiss. On the road in 2035: Reducing transportations petroleum consumption and ghg emissions. *MA: MIT Laboratory for Energy and the Environment*, 2008.

[6] L. E. Bell. Cooling, heating, generating power, and recovering waste heat with thermoelectric systems. *Science*, 321(1457):1457–1461, 2008.

[7] BMW. Dynamic drive. `http://www.bmw.com/com/en/insights/technology/technology_guide/articles/dynamic_drive.html`.

[8] Ian L. Cassidy, Jeffrey T. Scruggs, Sam Behrens, and Henri P. Gavin. Design and experimental characterization of an electromagnetic transducer for large-scale vibratory energy harvesting applications. *Journal of Intelligent Material Systems and Structures*, 22(17):2009–2024, 2011.

[9] N.C. Cheung, K.-W. Lim, and M.F. Rahman. Modelling a linear and limited travel solenoid. In *Industrial Electronics, Control, and Instrumentation, 1993. Proceedings of the IECON '93., International Conference on*, pages 1567–1572 vol.3, Nov 1993.

[10] Bose Corporation. Bose suspension system. "http://www.bose.com/controller?url=/automotive/bose_suspension/the_system.jsp".

[11] John C. Dixon. *The shock absorber handbook*. Society of Automotive Engineers, Warrendale, PA, 1999.

[12] Babak Ebrahimi, Mir Behrad Khamesee, and Farid Golnaraghi. A novel eddy current damper: theory and experiment. *Journal of Physics D: Applied Physics*, 42(7):1–6, 2009.

[13] Y. Fujimoto, T. Kominami, and H. Hamada. Development and analysis of a high thrust force direct-drive linear actuator. *Industrial Electronics, IEEE Transactions on*, 56(5):1383–1392, May 2009.

[14] Piersol Alan G. and Thomas L. Paez. *Harris' Shock and Vibration Handbook. 6th ed.* McGraw-Hill, New York, 2009.

[15] A. Gupta, J. A. Jendrzejczyk, T. M. Mulcahy, and J. R. Hull. Design of electromagnetic shock absorbers. *International Journal of Mechanics and Materials in Design*, 3(3):285–291, 2006.

[16] Bart L. J. Gysen, Tom P. J. van der Sande, Johannes J. H. Paulides, and Elena A. Lomonova. Efciency of a regenerative direct-drive electromagnetic active suspension. *IEEE TRANSACTIONS ON VEHICULAR TECHNOLOGY*, 60(4):1384–1393, 2011.

[17] D. Hrovat, D. L. Margolis, and M. Hubbard. An approach toward the optimal semi-active suspension. *Journal of Dynamic Systems, Measurement, and Control*, 110:288–296, 1988.

[18] TENNECO Inc. Monroe shocks and struts e-catalog. http://www.monroe.com/en-US/catalog/e-Catalog/911258.

[19] W.D. Jones. Easy ride: Bose corp. uses speaker technology to give cars adaptive suspension. *Spectrum, IEEE*, 42(5):12–14, 2005.

[20] D. Karnopp, M. J. Crosby, and R. A. Harwood. Vibration control using semi-active force generators. *Journal of Engineering for Industry*, 96(2):619–626, 1974.

[21] Y. Kawamoto, Y. Suda, H. Inoue, and T. Kondo. Electro-mechanical suspension system considering energy consumption and vehicle manoeuvre. *Vehicle System Dynamics*, 46:1053–1063, 2008.

[22] Z. Li, Z. Brindak, and L. Zuo. Modeling of an electromagnetic vibration energy harvester with motion magnification. In *ASME 2011 International Mechanical Engineering Congress & Exposition IMECE2011*, Denver, 2011.

[23] Z. Li, L. Zuo, J. Kuang, and G. Luhrs. Energy-harvesting shock absorber with a mechanical motion rectier. *Smart Materials and Structures*, 22:1–10, 2013.

[24] Haiwei Lu, Jianguo Zhu, and Youguang Guo. Development of a slotless tubular linear interior permanent magnet micromotor for robotic applications. *Magnetics, IEEE Transactions on*, 41(10):3988–3990, 2005.

[25] Mercedes-Benz. Active body control abc. `http://m.mercedes-benz.de/de_DE/abc/detail.html`.

[26] Multimatic. Drayson racing sets new fia world electric land speed record using multimatic dserd technology. `http://www.multimatic.com/news/release.php?release=60`.

[27] K. Nakano and Y. Suda. Combined type self-powered active vibration control of truck cabins. *Vehicle System Dynamics*, 46(6):449–473, 2004.

[28] Rogelio Palomera-Arias, Jerome J. Connor, and John A. Ochsendorf. Feasibility study of passive electromagnetic damping systems. *Journal of Structural Engineering*, 134:164–170, 2008.

[29] Sanjay M. Patel and A. D. Patel. Investigation and analysis of quarter car automotive suspension using mathematical model. *PARIPEX- Indian Journal of Research*, 2(7):86–88, 2013.

[30] Levant power. Our technology. `http://www.levantpower.com/technology/`.

[31] Rajesh Rajamani. Design and analysis of passive automotive suspensions. In *Vehicle Dynamics and Control*, Mechanical Engineering Series, pages 287–323. Springer US, 2006.

[32] L. C. Rome, L. Flynn, E. M. Goldman, and T. D. Yoo. Generating electricity while walking with loads. *Science*, 309:1725–1728, 2005.

[33] Sergio M. Savaresi, Charles Poussot-Vassal, Cristiano Spelta, Oliver Sename, and Luc Dugard. *Semi-active suspension control design for vehicles*. Butterworth-Heinemann/Elsevier, Oxford, UK, 2010.

[34] S.Kameyama, M. Kato, A. Kawamura, K. Himeno, and A.Kasahara. Effects of frost heave on the longitudinal profile of asphalt pavements in cold regions. In *ISAP 9th Conference Titles & Abstracts (09044)*, Copenhagen, 2002.

[35] M. VALEK, M. NOVK, Z. IKA, and O. VACULN. Extended ground-hook - new concept of semi-active control of truck's suspension. *Vehicle System Dynamics*, 27(5-6):289–303, 1997.

[36] G. Verros, S. Natsiavas, and C. Papadimitrious. Design optimization of quarter-car models with passive and semi-active suspensions under random road excitation. *Journal of Vibration and Control*, 11(5):581–606, 2005.

[37] J. Wang, D. Howe, and W. G. Jewell. Analysis and design optimization of an improved axially magnetized tubular permanent-magnet machine. *IEEE Transactions on Energy Conversion*, 19(2):289–295, 2004.

[38] J. Y. Wong. *Theory of ground vehicles*. Wiley, New York, 2008.

[39] G. Zhang, J. Cao, and F. Yu. Design of active and energy-regenerative controllers for dc-motor-based suspension. *Mechatronics*, 22:1124–1134, 2012.

[40] Y. Zhang, K. Huang, F. Yu, Y. Gu, and D. Li. Experimental verification of energy-regenerative feasibility for an automotive electrical suspension system. In *IEEE International Conference on Vehicular Electronics and Safety*, pages 1–5, 2007.

[41] L. Zuo, B. Scully, J. Shestani, and Y. Zhou. Design and characterization of an electromagnetic energy harvester for vehicle suspensions. *Smart Materials and Structures*, 19(4):1–10, 2011.

[42] L. Zuo and P. Zhang. Energy, ride comfort, and road handling of regenerative vehicle suspensions. In *ASME dynamic systems and control conference*, Arlington, 2011.

[43] Kristina Zuza. Rethinking faraday's law for teaching motional electromotive force. *European Journal of Physics*, 33(2):397–406, 2012.